

University of Windsor

## Scholarship at UWindor

---

Electronic Theses and Dissertations

Theses, Dissertations, and Major Papers

---

2001

**I. Attempted synthesis and characterisation of an electron-deficient transition metal complex potentially useful in carbon-hydrogen bond activation. II. Investigations of mesoporous niobium oxide - cobaltocene composites: The first example of superparamagnetism in molecule-based clusters.**

Samantha Murray  
*University of Windsor*

Follow this and additional works at: <https://scholar.uwindsor.ca/etd>

---

### Recommended Citation

Murray, Samantha, "I. Attempted synthesis and characterisation of an electron-deficient transition metal complex potentially useful in carbon-hydrogen bond activation. II. Investigations of mesoporous niobium oxide - cobaltocene composites: The first example of superparamagnetism in molecule-based clusters." (2001). *Electronic Theses and Dissertations*. 2352.  
<https://scholar.uwindsor.ca/etd/2352>

This online database contains the full-text of PhD dissertations and Masters' theses of University of Windsor students from 1954 forward. These documents are made available for personal study and research purposes only, in accordance with the Canadian Copyright Act and the Creative Commons license—CC BY-NC-ND (Attribution, Non-Commercial, No Derivative Works). Under this license, works must always be attributed to the copyright holder (original author), cannot be used for any commercial purposes, and may not be altered. Any other use would require the permission of the copyright holder. Students may inquire about withdrawing their dissertation and/or thesis from this database. For additional inquiries, please contact the repository administrator via email ([scholarship@uwindsor.ca](mailto:scholarship@uwindsor.ca)) or by telephone at 519-253-3000ext. 3208.

## **INFORMATION TO USERS**

This manuscript has been reproduced from the microfilm master. UMI films the text directly from the original or copy submitted. Thus, some thesis and dissertation copies are in typewriter face, while others may be from any type of computer printer.

**The quality of this reproduction is dependent upon the quality of the copy submitted.** Broken or indistinct print, colored or poor quality illustrations and photographs, print bleedthrough, substandard margins, and improper alignment can adversely affect reproduction.

In the unlikely event that the author did not send UMI a complete manuscript and there are missing pages, these will be noted. Also, if unauthorized copyright material had to be removed, a note will indicate the deletion.

Oversize materials (e.g., maps, drawings, charts) are reproduced by sectioning the original, beginning at the upper left-hand corner and continuing from left to right in equal sections with small overlaps.

Photographs included in the original manuscript have been reproduced xerographically in this copy. Higher quality 6" x 9" black and white photographic prints are available for any photographs or illustrations appearing in this copy for an additional charge. Contact UMI directly to order.

**ProQuest Information and Learning  
300 North Zeeb Road, Ann Arbor, MI 48106-1346 USA  
800-521-0600**

**UMI<sup>®</sup>**



## **NOTE TO USERS**

**This reproduction is the best copy available.**

UMI<sup>®</sup>



**I: ATTEMPTED SYNTHESIS AND CHARACTERISATION OF AN  
ELECTRON DEFICIENT TRANSITION METAL COMPLEX  
POTENTIALLY USEFUL IN C-H BOND ACTIVATION.**

**II: INVESTIGATIONS OF MESOPOROUS NIOBIUM OXIDE –  
COBALTOCENE COMPOSITES: THE FIRST EXAMPLE OF  
SUPERPARAMAGNETISM IN MOLECULE-BASED CLUSTERS.**

**By Samantha Murray**

**A Thesis  
Submitted to the Faculty of Graduate Studies and Research  
through the School of Physical Sciences  
Chemistry and Biochemistry  
in Partial Fulfilment of the Requirements for  
the Degree of Master of Science at the  
University of Windsor**

**Windsor, Ontario, Canada**

**2000**



National Library  
of Canada

Acquisitions and  
Bibliographic Services

395 Wellington Street  
Ottawa ON K1A 0N4  
Canada

Bibliothèque nationale  
du Canada

Acquisitions et  
services bibliographiques

395, rue Wellington  
Ottawa ON K1A 0N4  
Canada

*Your file Votre référence*

*Our file Notre référence*

The author has granted a non-exclusive licence allowing the National Library of Canada to reproduce, loan, distribute or sell copies of this thesis in microform, paper or electronic formats.

The author retains ownership of the copyright in this thesis. Neither the thesis nor substantial extracts from it may be printed or otherwise reproduced without the author's permission.

L'auteur a accordé une licence non exclusive permettant à la Bibliothèque nationale du Canada de reproduire, prêter, distribuer ou vendre des copies de cette thèse sous la forme de microfiche/film, de reproduction sur papier ou sur format électronique.

L'auteur conserve la propriété du droit d'auteur qui protège cette thèse. Ni la thèse ni des extraits substantiels de celle-ci ne doivent être imprimés ou autrement reproduits sans son autorisation.

0-612-62257-6

**Canada**

928842

© Samantha Murray

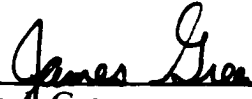


**APPROVED BY:**



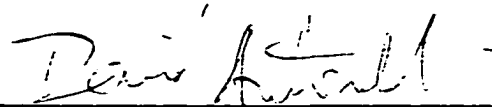
---

**Dr. D. Watt**  
Department of Mechanical - Automotive & Materials  
Engineering.



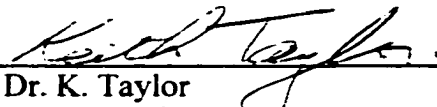
---

**Dr. J. Green**  
School of Physical Sciences, Department of Chemistry  
and Biochemistry.



---

**Dr. D. Antonelli**  
School of Physical Sciences, Department of Chemistry  
and Biochemistry.



---

**Dr. K. Taylor**  
Director, School of Physical Sciences, Department of  
Chemistry and Biochemistry.

# ABSTRACT

## Chapter One

The attempted syntheses of electron deficient transition metal complexes proposed to be useful in C-H bond activation processes are reported. Because tris(trimethylsilyl)methane (HTsi) is sterically demanding but only donates one electron, we were interested in synthesising transition metal complexes with this ligand, under the assumption that these traits would be important in designing an extremely electron deficient transition metal complex for use in C-H bond activation processes. By means of three synthetic approaches, nucleophilic attack, oxidative addition and free radical reactions, the syntheses of several ligand complexes, Ir(Tsi)I(CO)(PPh<sub>3</sub>)<sub>2</sub>, Rh(Tsi)I(CO)(PPh<sub>3</sub>)<sub>2</sub>, RhSiTsi(PPh<sub>3</sub>)<sub>3</sub>, Ir(SiTsi)CO(PPh<sub>3</sub>)<sub>2</sub>, MnSiTsiCl, NbCl<sub>4</sub>Tsi, TaCl<sub>4</sub>Tsi, ZrCl<sub>3</sub>Tsi and TaMe<sub>3</sub>ClTsi) were attempted but most products were intractable. The isolation and characterisation via <sup>1</sup>H NMR spectroscopy of a Ru-H species, (RuClH(C<sub>6</sub>H<sub>5</sub>Tsi)PPh<sub>3</sub>), formed from the direct reaction of RuCl(Tsi)(C<sub>6</sub>H<sub>6</sub>)PPh<sub>3</sub> with LiTsi, is discussed. The characterisation of, and hypothesised mechanistic pathway towards a novel organic material, benzyl-Tsi, formed during the course of our investigations, is also reported.

## Chapter Two

Herein we report the synthesis of a superparamagnetic cobaltocene mesoporous Nb-oxide based composite. This is the first example of a molecular ensemble displaying superparamagnetic behaviour. Investigations were conducted on how variations in pore size, wall thickness, wall composition and cobaltocene loading level affected the superparamagnetic behaviour. All samples prepared were characterised by Nitrogen Adsorption, XRD, XPS, UV, Elemental Analysis, SQUID Magnetometry and SEM. The results obtained demonstrated that a change in pore volume and wall thickness had little effect on the magnetic properties of these mesoporous composites. A change in wall composition to Ti and Ta-oxide based mesoporous materials led to the isolation of composites, which were paramagnetic with no superparamagnetic properties. These studies also demonstrated that a critical M:Co (M = Nb, Ti or Ta) mol ratio and a critical Co(II):Co(III) ratio was required for the onset of superparamagnetism. (An investigation into the thermal stability of the intercalated Nb-TMS1 materials was also conducted.)

## ACKNOWLEDGEMENTS

Principally, I would like to thank my supervisor Dr. David Antonelli. His help, guidance, advice and support during my graduate term here at the University of Windsor will be remembered and always appreciated.

I am also extremely grateful to Mr. Fuerth, Dr. Stephan, Mr. Robinson and Dr. Lazarescu for all their helpful advice and expertise with regards to the analytical data acquired within the department. Special thanks is also given to Dr. M. Trudeau<sup>†</sup> whose collaborative work with SQUID magnetometry and XPS analysis has been invaluable towards the success of the project.

There are many Departmental Representatives (Faculty, Staff and Graduate students) who have made the past years extremely enjoyable and memorable. They are all thanked for their support and kindness.

Finally I would like to thank my husband and family for the encouragement they have given me during this final journey.

---

<sup>†</sup> Dr. M. Trudeau, Technologies Emergentes, IREQ, Hydro-Quebec, 1800 Boul. Lionel-Boulet, Varennes, Quebec, Canada J3X 1S1

# TABLE OF CONTENTS

	Page
Abstract.....	iv
Acknowledgements.....	vi
List of Figures.....	xi
List of Tables.....	xiv
List of Schemes.....	xv
List of Abbreviations.....	xvi

## Chapter One

### Synthesis and Characterisation of an Electron Deficient Transition Metal Complex Potentially Useful in C-H Bond Activation

1.	<b>Introduction</b> .....	1
1.1.	Methane Activators.....	2
1.1.1.	Bioinorganic Methane Activators.....	2
1.1.2.	Transition Metal Mediated Alkane Activation.....	3
1.1.3.	Alternative Systems.....	10
1.1.4.	Synthesis of an Electron Deficient Transition Metal Species.....	14
1.2.	<b>Results and Discussion</b> .....	16
1.2.1	LiTsi.....	16
1.2.2.	$\eta$ -Benzenedichloro(triphenylphosphine)ruthenium (II).....	18
1.2.3.	LiSiTsi.....	23

1.2.4.	Oxidative Addition Reactions with ITsi.....	27
1.2.5.	Free Radical Reactions with HSiTsi.....	28
1.3.	Early Transition Metals.....	29
1.3.1.	The Pentachlorides of Niobium and Tantalum.....	29
1.3.2.	Trimethyl Tantalum Dichloride.....	36
1.3.3.	Zirconium Tetrachloride.....	37
1.3.4.	Me <sub>3</sub> SnTsi and <sup>n</sup> Bu <sub>3</sub> SnTsi.....	39
1.4.	<b>Conclusion</b> .....	41
	Future Work.....	43
1.5.	<b>Experimental</b> .....	44
1.5.1.	General Methods.....	44
1.5.2.	Reaction of RuCl <sub>2</sub> C <sub>6</sub> H <sub>6</sub> (PPh <sub>3</sub> ) + LiTsi.....	46
1.5.3.	Reaction of LiSiTsi and RhCl(PPh <sub>3</sub> ) <sub>3</sub> .....	46
1.5.4.	Synthesis of Benzyl-Tsi (A).....	47
1.5.5.	Synthesis of Benzyl-Tsi (B).....	48
1.5.6.	Reaction of Me <sub>3</sub> TaCl <sub>2</sub> + LiTsi.....	48
1.5.7.	Reaction of ZrCl <sub>4</sub> + LiTsi.....	49

## Chapter Two

### Investigations into Mesoporous Niobium Oxide – Cobaltocene Composites: the First Example of Superparamagnetism in Molecule-Based Clusters.

2.1.	<b>Introduction</b> .....	50
2.1.1.	MCM-41 and M41S Physical Properties and Synthesis.....	51
2.1.2.	Non (Alumino) Silicate Based Mesoporous Materials.....	53
2.1.3.	Catalytic Properties.....	56

2.1.4.	<b>Intercalation of Organometallic Species into the Mesoporous Framework.....</b>	<b>56</b>
2.1.5.	<b>Cobaltocene.....</b>	<b>59</b>
2.1.6.	<b>Characterisation of the Isolated Products.....</b>	<b>60</b>
	X-ray Photoelectron Spectroscopy (XPS).....	60
	Electron Paramagnetic Resonance (EPR).....	61
	Ultraviolet Reflectance Spectroscopy (UV).....	63
	X-ray Powder Diffraction (XRD).....	63
	Nitrogen Adsorption Studies.....	64
	Scanning Electron Microscopy (SEM).....	64
	Elemental Analysis (E.A.).....	65
	Superconducting Quantum Interference Device (SQUID).....	65
2.2.	<b>Results and Discussion.....</b>	<b>67</b>
2.2.1.	<b>Synthesis of a Cobaltocene - Mesoporous Niobium Composite Exhibiting Superparamagnetic Behaviour (1).....</b>	<b>67</b>
2.2.2.	<b>Probing the Effect of Wall Thickness on a Superparamagnetic Cobaltocene Mesoporous Niobium Composite (2).....</b>	<b>77</b>
2.2.3.	<b>Probing the Effect of Pore Size on a Superparamagnetic Cobaltocene Mesoporous Niobium Composite (3).....</b>	<b>85</b>
2.2.3.1.	<b>An Investigation into the Critical Loading Level and Critical Co(II):Co(III) Ratio Required for the Onset of the Superparamagnetic Transition (4 and 5).....</b>	<b>92</b>
2.2.3.2.	<b>Probing the Thermal Stability of Composite 3.....</b>	<b>97</b>
2.2.4.	<b>Effect of Wall Composition on the Superparamagnetic Cobaltocene Mesoporous Materials.....</b>	<b>99</b>
2.2.4.1.	<b>Ti-TMS1 CoCp<sub>2</sub> (6).....</b>	<b>99</b>
2.2.4.2.	<b>Ta-TMS1 CoCp<sub>2</sub> (7).....</b>	<b>107</b>

2.2.5.	Host-Guest Equilibrium Effects on the Mesoporous Composites (8)...	112
2.3.	<b>Conclusion</b> .....	116
2.4.	<b>Experimental</b> .....	118
2.4.1.	General Methods.....	118
2.4.2.	Synthesis of Nb-TMS1 CoCp <sub>2</sub> (1).....	120
2.4.3.	Synthesis of Material 2.....	121
2.4.4.	Synthesis of Material 3.....	122
2.4.4.1.	Synthesis of Materials 4 and 5.....	123
2.4.4.2.	Heat Treatment of Material 3.....	123
2.4.5.	Synthesis of Material 6.....	124
2.4.6.	Synthesis of Material 7.....	125
3.1.	<b>Appendix A</b>	
	ORTEP of Benzyl-Tsi.....	126
3.2.	<b>Appendix B</b>	
	Relevant X-ray Parameters Used in Calculating the Structure for Benzyl-Tsi.....	127
3.3.	<b>Appendix C</b>	
	Relevant Structural Data for Benzyl-Tsi.....	128
4.	<b>References</b> .....	130
5.	<b>Curriculum Vitae</b> .....	137



## LIST OF FIGURES

Figure	Description	Page
1	Proposed Mechanistic Cycle for the Production of Methanol from Methane, via the Iron Catalyst, MMO <sup>4,5</sup> .....	2
2	Synthesis of a Stable Ir (III) Hydrido Methyl Complex <sup>10</sup> .....	4
3	1,2-Addition Reaction with an Electron Deficient Zirconium-Imido Complex <sup>13</sup> .....	6
4	1,2-Addition Reaction .....	6
5	A Stable Tantalum Oxo Complex.....	7
6	The First Example of Sigma Bond Metathesis by an Ir (III) Complex	8
7	Reaction Mechanism for the Oxidation of Methane to Methanol on the Pt-Complex (A) <sup>18,19</sup> .....	9
8	Tris(trimethylsilyl)methane, HTsi.....	12
9(a)	<sup>1</sup> H NMR of LiTsi in C <sub>6</sub> D <sub>6</sub> .....	16
9(b)	<sup>13</sup> C { <sup>1</sup> H} NMR of LiTsi in C <sub>6</sub> D <sub>6</sub> .....	17
10	Mn-Tsi Cluster.....	17
11(a)	<sup>1</sup> H NMR Spectrum for the Product Obtained from the Reaction between RuCl <sub>2</sub> C <sub>6</sub> H <sub>6</sub> (PPh <sub>3</sub> ) and LiTsi in C <sub>6</sub> D <sub>6</sub> .....	19
11(b)	Enlargement of <sup>1</sup> H NMR from 10(a) Showing the Benzyl Region.....	20
11(c)	<sup>1</sup> H NMR Spectrum for Ru-H Region.....	21
12	Hydride Migration from the Bound Ligand to the Metal Centre <sup>43</sup> .....	23
13(a)	<sup>1</sup> H NMR of the Product Obtained from the Reaction between Wilkinson's Catalyst and LiSiTsi in C <sub>6</sub> D <sub>6</sub> .....	25
13(b)	<sup>31</sup> P { <sup>1</sup> H} NMR of the Crystals Obtained from the Reaction between Wilkinson's Catalyst and LiSiTsi in C <sub>6</sub> D <sub>6</sub> .....	26
14(a)	<sup>1</sup> H NMR of Benzyl-Tsi in C <sub>6</sub> D <sub>6</sub> .....	30
14(b)	<sup>13</sup> C NMR of Benzyl-Tsi in C <sub>6</sub> D <sub>6</sub> .....	30
14(c)	X-ray of Benzyl-Tsi.....	31

Figure	Description	Page
15(a)	<sup>1</sup> H NMR of the Zr-Tsi Cluster Complex in C <sub>6</sub> D <sub>6</sub> .....	38
15(b)	<sup>13</sup> C { <sup>1</sup> H} NMR of the Zr-Tsi Cluster Complex in C <sub>6</sub> D <sub>6</sub> .....	38
16(a)	Bis[tris(trimethylsilyl)phenylsilane].....	43
16(b)	Bis[tris(trimethylsilyl)phenylsilyl]lithium.....	43
17(a)	Nitrogen Adsorption Isotherm for the Trimethylsilated Nb-TMS1 Starting Material.....	68
17(b)	Nitrogen Adsorption Isotherm for Material 1.....	68
18(a)	XRD Diffraction Pattern for 1.....	69
18(b)	XRD Diffraction Pattern for Trimethylsilated Nb-TMS1.....	69
19(a)	XPS Spectrum for Co 2p 3/2 Region for 1.....	71
19(b)	XPS Spectrum for Nb 3d 5/2, 3/2 Region for 1.....	72
20	EPR Spectrum for 1.....	73
21(a)	M vs. T Plot (at 250 G) for 1 Illustrating the ZFC FC Cross Over.....	74
21(b)	B vs. H Plot for 1 obtained at 10 K and 300 K.....	75
22(a)	Nitrogen Adsorption Isotherm for Trimethylsilated Nb-TMS1.....	78
22(b)	Nitrogen Adsorption Isotherm for Material 2.....	78
23(a)	XRD Diffraction Pattern for Trimethylsilated Nb-TMS1.....	79
23(b)	XRD Diffraction Pattern for Material 2.....	79
24	XPS Spectrum for Co 2p 3/2 Region for 2.....	80
25	XPS Spectrum for Nb 3d 5/2, 3/2 Region for the Trimethylsilated Nb-TMS1 (a) Composite and that for 2 (b).....	81
26	EPR Spectrum for 2.....	82
27	M vs. T Plot for 2.....	83
28	B vs. H Plot for 2.....	84

Figure	Description	Page
29(a)	Nitrogen Adsorption Isotherm for Trimethylsilated Nb-TMS1 Mesoporous Material.....	85
29(b)	Nitrogen Adsorption Isotherm for Material 3.....	86
30(a)	XRD Diffraction Pattern for Trimethylsilated Mesoporous Material Nb-TMS1.....	87
30(b)	XRD Diffraction Pattern Obtained for Material 3.....	87
31(a)	XPS Spectrum of the Co 2p 3/2 Region for 3.....	88
31(b)	XPS Spectrum for Nb 3d 5/2, 3/2 Region for 3.....	89
32(a)	M vs. T Plot for 3.....	90
32(b)	B vs. H Plot for 3.....	90
33	SEM Images for (a) Trimethylsilated Mesoporous Nb-TMS1 and (b) 3.....	91
34(a)	XPS Spectrum of the Co 2p 3/2 Region for 5.....	93
34(b)	XPS Spectrum of the Co 2p 3/2 Region for 4.....	93
35	M vs. T Plot for 4.....	95
36	M vs. T Plot for 5.....	95
37	XPS Spectrum of the Co 2p 3/2 Region, Comparing Non-Heat Treated Material 3 (a), to that of the Heated Sample (b).....	97
38	XPS Spectrum of the Nb 3d 5/2, 3/2 Region, Comparing Non-Heat Treated Material 3 (a), to that of the Heated Sample (b).....	98
39(a)	XRD Diffraction Pattern of Trimethylsilated Ti-TMS1.....	100
39(b)	XRD Diffraction Pattern of 6.....	100
40(a)	Nitrogen Adsorption Isotherm for a Sample of Trimethylsilated Ti-TMS1.....	101
40(b)	Nitrogen Adsorption Isotherm of 6.....	101

Figure	Description	Page
41(a)	XPS Spectrum for Ti 2p 3/2, 1/2 Region for 6.....	103
41(b)	XPS Spectrum for Ti 2p 3/2, 1/2 Region for the Trimethylsilated Ti-TMS1 Composite.....	103
41(c)	XPS Spectrum of the Co 2p 3/2 Region for 6.....	104
42	EPR Spectrum for 6.....	105
43	M vs. T Plot for Material 6.....	106
44	B vs. H Plot for Material 6.....	106
45(a)	XRD Diffraction Pattern for the Trimethylsilated Ta-TMS1 Mesoporous Material.....	108
45(b)	XRD Diffraction Pattern for Material 7.....	108
46(a)	Nitrogen Adsorption Isotherm for the Trimethylsilated Ta-TMS1 Mesoporous Composite.....	109
46(b)	Nitrogen Adsorption Isotherm for Material 7.....	109
47(a)	XPS Spectrum for Ta 4f 7/2, 5/2 Region for 7.....	110
47(b)	XPS Spectrum for Ta 4f 7/2, 5/2 Region for Trimethylsilated Ti-TMS1 Mesoporous Composite.....	111
47(c)	XPS Spectrum of the Co 2p 3/2 Region for 7.....	111
48	EPR Spectrum for Material 7.....	112
49(a)	M vs. T Plot for 7.....	113
49(b)	B vs. H Plot at 10 K and 300 K for 7.....	114

## LIST OF TABLES

		Page
Table 1:	Organometallic Species Investigated.....	45
Table 2:	A Variation in the S:I Ratio Leads to the Isolation of Mesoporous Materials with Differing Mesostructures. <sup>51</sup> .....	54
Table 3:	XPS Reference Data for Co 2p 3/2 Region of Co(II) and Co(III) Species <sup>94</sup> .....	61

## LIST OF SCHEMES

		Page
Scheme 1:	Reactions Used for the Activation of C-H Bonds <sup>2,7</sup> .....	3
Scheme 2:	Proposed Mechanism for the Reaction of RuCl <sub>2</sub> C <sub>6</sub> H <sub>6</sub> (PPh <sub>3</sub> ) with LiTsi in C <sub>6</sub> D <sub>6</sub> .....	22
Scheme 3:	Second Proposed Hypothetical Reaction Sequence for the Formation of Benzyl-Tsi .....	34
Scheme 4:	Proposed Reductive Elimination Pathway for the Formation of Benzyl-Tsi.....	35
Scheme 5:	Synthesis of Nb-TMS1CoCp <sub>2</sub> (1). Giving the Non Saturated Mesoporous Species A (Black) and Upon Further Addition of CoCp <sub>2</sub> the Saturated Product - Material (1) Dark Green in Colour. Oxidation of Both Species Led to the Isolation of the Bright Green Coloured Material B.....	70
Scheme 6:	A Schematic Representation of the Theoretical Composition of the Mesoporous Material after Intercalation of the Organometallic Species into the Lattice of the Composite (a) with Less than or Equal to 0.1 Equivalents of CoCp <sub>2</sub> to Nb; (b) with Greater than 0.1 Equivalents of the Organometallic to Nb Ratio, within the Mesoporous Material.....	96

## LIST OF ABBREVIATIONS

$\alpha$ -Nicotinamide Adenine Dinucleotide Phosphate, Reduced Form.....	NAD(P)H
Approximately.....	ca.
Broad.....	b
Carbon Nuclear Magnetic Resonance, Proton Decoupled.....	$^{13}\text{C}\{^1\text{H}\}$ NMR
Chemical Shift in ppm.....	$\delta$
Chlorotrimethylsilane (or Trimethylsilylchloride).....	TMSCl
Cyclooctadiene.....	COD
Cyclooctene.....	COE
Cyclopentadienyl.....	Cp
Doublet.....	d
Doublet of doublets.....	dd
Doublet of doublets of doublets.....	ddd
Electron.....	e-
Family of Mesoporous Materials.....	M41S
Light Energy.....	h $\nu$
Mesoporous Manganese Oxides.....	MOMS
Mesoporous Niobium Oxides.....	Nb-TMS1
Mesoporous Tantalum Oxides.....	Ta-TMS1
Mesoporous Titanium Oxides.....	Ti-TMS1
Mesoporous Zirconium Oxides.....	Zr-TMS1
Methane Mono-Oxygenase.....	MMO
Methyl.....	Me
Mobil Composition of Matter – 41, Hexagonal Mesoporous Phase.....	MCM-41
Multiplet.....	m
n-Butyl.....	$^n\text{Bu}$
Nuclear Magnetic Resonance.....	NMR
Number of Electron Counts per Electron.....	N(E)/E
Oak Ridge Thermal Ellipsoid Program.....	ORTEP

Pentamethylcyclopentadienyl.....	Cp*
Phenyl.....	Ph
Phosphorous Nuclear Magnetic Resonance, Proton Decoupled .....	$^{31}\text{P} \{^1\text{H}\}$ NMR
Proton Nuclear Magnetic Resonance.....	$^1\text{H}$ NMR
Singlet.....	s
Tech. Molecular Sieve 1 .....	TMS1
Tetrahydrofuran.....	THF
Trimethylsilyl.....	TMS
Trimethylsilylchloride (or Chlorotrimethylsilane).....	TMSCl
Triphenylphosphine.....	$\text{PPh}_3$
Tris(trimethylsilyl)methyl.....	-Tsi

# Chapter One

## Synthesis and Characterisation of an Electron Deficient Transition Metal Complex Potentially Useful in C-H Bond Activation

### 1. Introduction

In recent years much research has been conducted in the area of selective activation of C-H bonds by transition metal complexes.<sup>1</sup> The ability to catalytically transform abundant amounts of organic compounds into "valuable products" is of great benefit to industry. To date, industrial use of alkanes has relied predominantly on free-radical activation of C-H bonds at very high temperatures. However, these reactions generally result in low selectivity. The selective oxidation of C-H bonds by a transition metal complex could ultimately transform alkanes into alcohols. Alkanes (such as methane) are the least expensive and most abundant hydrocarbon resource found within the world's natural ecosystem.<sup>2</sup> The transformation of methane gas into methanol would be an important achievement, especially for environmental and economic reasons including the production of a cheaper fuel for motor vehicles. This is greatly needed, even more so, since at the present consumption level petroleum reserves are rapidly diminishing. For this reason alone methanol is fast becoming a "high-demand, under-supplied, cost-price driven product".<sup>3</sup>



## 1.1. Methane Activators

### 1.1.1. Bioinorganic Methane Activators

Bioinorganic systems have long been known for their role in methane activation.<sup>4,5</sup> It has only been in recent years that catalytic processes of this type have been explored in more depth. Some important results include the successful elucidation of the role played by methane mono-oxygenase (MMO) in methane activation. The results have shown that MMO, a di-iron complex, activates dioxygen for its further insertion into the C-H bond of stable hydrocarbons. The complex MMO catalyses the methane to methanol activation reaction in the presence of two equivalents of  $\alpha$ -Nicotinamide Adenine Dinucleotide Phosphate, reduced form (NAD(P)H). The proposed catalytic cycle for this sequence is shown in **Figure 1**.

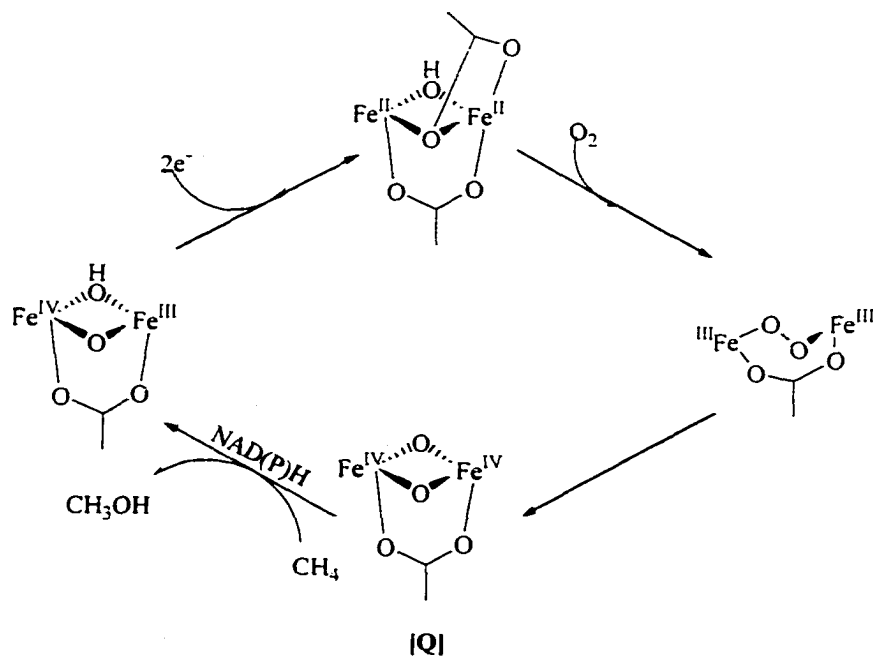


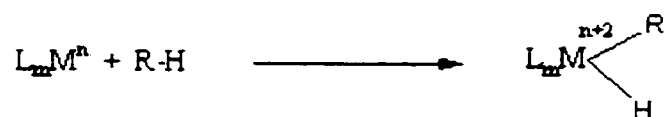
**Figure 1:** Proposed Mechanistic Cycle for the Production of Methanol from Methane, via the Iron Catalyst, MMO<sup>4,5</sup>

This reaction mechanism has been extensively investigated<sup>5</sup> and the conclusions indicate that the intermediate species [Q], upon introduction of methane, facilitates a free radical transformation that leads to the synthesis of methanol.

### 1.1.2. Transition Metal Mediated Alkane Activation

Since the early 1980's much research into the synthesis of transition metal complexes capable of methane activation has been conducted.<sup>6</sup> Reactions that have been successfully used for organometallic activation of hydrocarbons are illustrated in **Scheme 1**.<sup>2,7</sup>

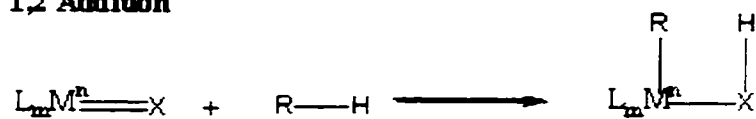
#### Oxidative Addition



#### $\alpha$ -Bond Metathesis



#### 1,2 Addition



X = O, NR, CR<sub>2</sub>

#### Electrophilic Activation



X = Halide, Hydroxide, Triflate... etc.

**Scheme 1: Reactions Used for the Activation of C-H Bonds**<sup>2,7</sup>

Reactions carried out independently by Graham<sup>8</sup>, Jones<sup>1</sup> and Bergman<sup>9</sup> in the early 1980's have shown that  $16e^- d^8$  rhodium and iridium complexes are capable of cleaving C-H bonds. Bergman and co-workers<sup>10</sup> showed that the transition metal product, from the reaction of the  $18e^- d^8$  iridium complex (2) with methane, was a very stable  $18e^-$  iridium (III) hydrido alkyl complex (3). Unfortunately the formation of this  $18e^-$  species renders the complex inactive to downstream reactivity of the alkyl functionality. **Figure 2.**

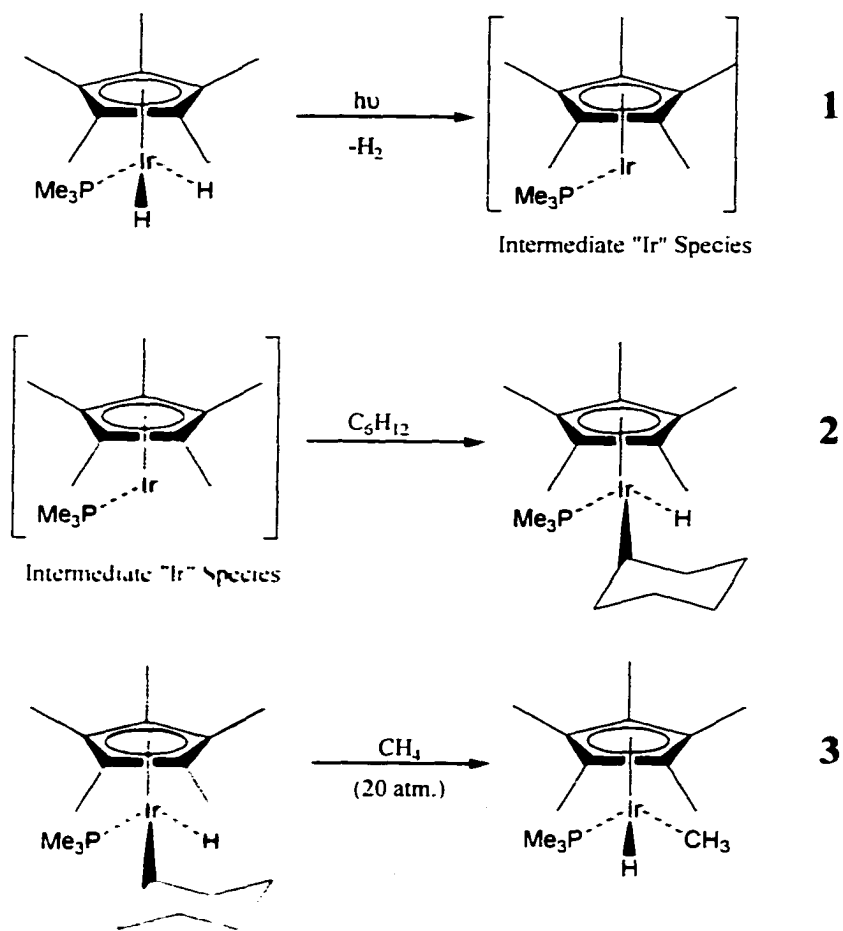


**Figure 2: Synthesis of a Stable Ir (III) Hydrido Methyl Complex.**<sup>10</sup>

By subjecting the Ir (Cp\*Ir(PMe<sub>3</sub>)H<sub>2</sub>) complex to photolysis, producing species (1), then creating an intermediate hydrido cyclohexyl iridium complex (2), the synthesis of the methyl complex (3) was achieved successfully.<sup>10</sup>

In 1982, Graham and co-workers successfully activated methane directly by using a photochemically generated iridium (I) complex.<sup>8</sup> This was the first documented example of stoichiometric C-H activation of methane by oxidative addition across a transition metal moiety.

During the same year Shilov<sup>11</sup> and co-workers showed that aqueous platinum (II) species were capable of mediating alkane oxidation reactions. The proposed mechanism for the catalytic cycle was later studied by other research groups<sup>12</sup> leading to a better understanding of the individual steps taking place during the reaction sequence. It is believed that electrophilic activation of the alkane by a Pt(II) species occurs first, followed by a 2-electron oxidative addition to give a Pt(IV) species, and finally reductive elimination results in the loss of the oxidized alkane and regeneration of the Pt(II) catalyst. A similar reaction mechanism to the one given above is illustrated in **Figure 7** and was developed by Periana *et al.* in 1998.<sup>20</sup>

In 1988 Wolczanski and Cummins<sup>13</sup> studied the 1,2-addition reaction of methane with an electron deficient zirconium-imido complex. The high reactivity of the complex was due to the low co-ordination number of the Zr centre imposed by the extremely bulky imido and amido groups. This bulk inhibited the dimerisation of the organometallic complex while allowing access to the highly reactive low co-ordinate Zr metal centre by small molecules. **Figure 3.**

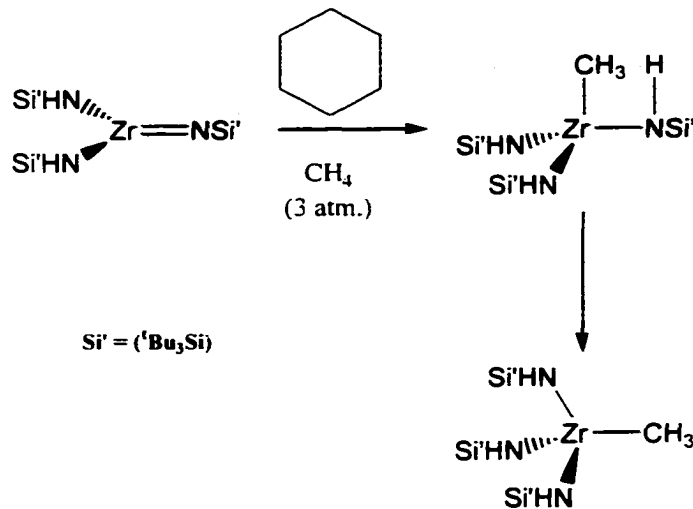


**Figure 3:** 1,2-Addition Reaction with an Electron Deficient Zirconium-Imido Complex<sup>13</sup>

Following this research Bergman and Glueck studied a similar 1,2-addition reaction with an  $18e^-$  iridium imido complex, **Figure 4**.<sup>14</sup> This  $[\text{Cp}^*\text{IrNBu}^t]$  species was synthesised via the treatment of  $[\text{Cp}^*\text{IrCl}_2]_2$  with four equivalents of  $\text{LiNHBu}^t$  in THF, giving repeatable 80-90 % yields.<sup>14</sup> This system was investigated because the respective  $\text{M}=\text{N}$  or  $\text{M}=\text{O}$  bonds (where  $\text{M}$  is a late transition metal) are generally weaker and more reactive than their earlier transition metal counterparts. It was believed that this feature would lead to downstream reactivity of the activated alkane functionality. This reaction, however, was unsuccessful as no addition of methane to the iridium complex was observed.

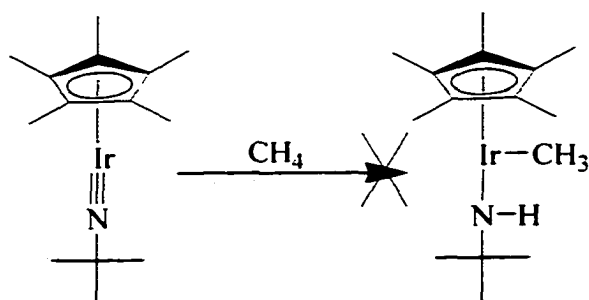


**Figure 4:** 1,2-Addition Reaction

This was possibly because the Ir complex in **Figure 4** is co-ordinatively saturated while the Zr complex of Wolczanski and Cummins is extremely electron deficient, leading to lower reactivity in the Ir complex. Hence, the question arises of how to make an electron deficient complex using a non-oxophilic metal in a co-ordination environment which allows not only catalytic but also stoichiometric C-H activation.

Further investigations conducted by Bergman and co-workers during the early 1990's led to the isolation of  $\text{Cp}^*_2\text{Zr}=\text{O}$ .<sup>15</sup> The reaction with methane did not proceed to the ultimate formation of methanol via the intermediate species  $\text{Cp}_2\text{Zr}(\text{CH}_3)\text{OH}$  because (a) the strength of the  $\text{Zr}=\text{O}$  bond did not favour bond scission and (b) reductive elimination to  $\text{Zr(II)}$  results in an unfavourable oxidation state for Zr.

In 1993, Antonelli and Bercaw,<sup>16</sup> carried out an analogous reaction using a stable (18-electron) tantalum oxide complex. No reaction was observed when the organometallic species was reacted with methane. This showed that the tantalum oxygen bond is too strong, as are most early transition metal oxide bonds and of course their respective nitride bonds. **Figure 5.**

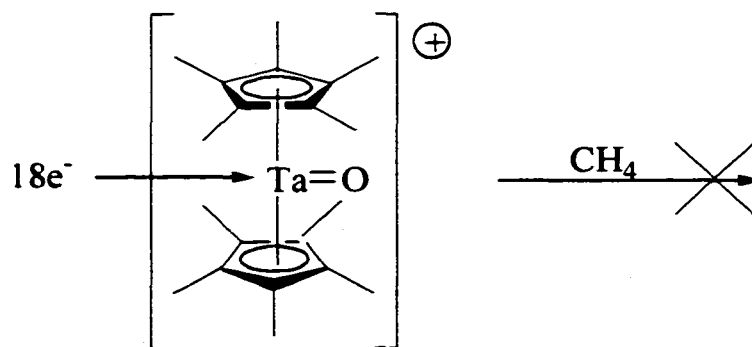


**Figure 5: A Stable Tantalum Oxide Complex**

In the same year Burger and Bergman<sup>17</sup> successfully activated C-H and Si-H bonds by using the electron deficient cationic Ir (III) species,  $[\text{Cp}^*(\text{PMe}_3)\text{Ir}(\text{CH}_3)]\text{OTf}$ ,  $\text{OTf} = \text{CF}_3\text{SO}_3$ . Their work illustrated that the greater the electrophilicity of the Ir (III) complex the more reactive the species is towards the activation of C-H bonds. A second observation made was that the ligand set imposes significant steric restrictions on the Ir (III) centre. Thus neither cyclohexane nor neopentane underwent C-H activation. Further investigations by Bergman and co-workers led to the synthesis of another electron deficient 16-electron Ir (III) species,<sup>18</sup> **Figure 6**, capable of C-H activation. The reaction of this organometallic moiety with benzene under mild conditions led to the formation of methane and the stable, electron deficient organometallic complex  $[\text{Cp}^*(\text{PMe}_3)\text{Ir}(\text{H})\text{C}_6\text{H}_5]$  via a  $\sigma$ -bond metathesis mechanism. This again highlighted the trends that the more electron deficient the species, the more reactive it is with respect to the activation of C-H bonds.

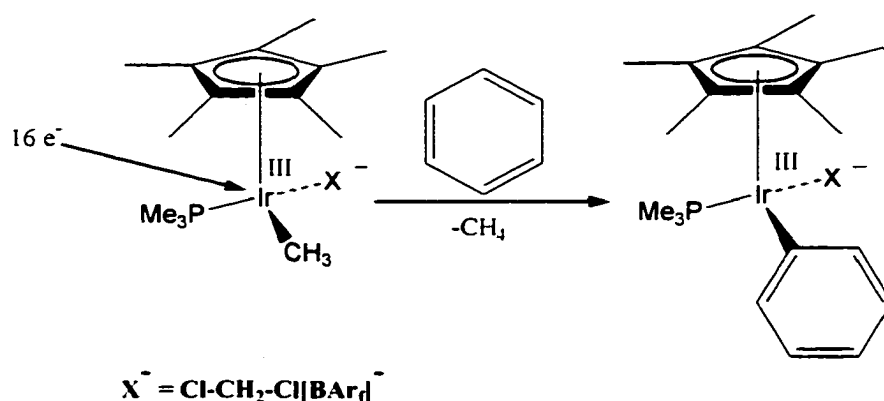


**Figure 6:** The First Example of  $\sigma$ -Bond Metathesis by an Iridium III Complex.<sup>18</sup>

These studies further demonstrated that Ir could undergo C-H activation by  $\sigma$ -bond metathesis and not only by oxidative addition.

More recently, Periana and co-workers demonstrated that sulphuric acid solutions of Hg and Pt salts could catalyse the conversion of methane to methanol.<sup>19</sup> This achievement led to the development of an organometallic complex, which under strongly acidic conditions (fuming sulphuric acid) underwent the process summarised in **Figure 7**.<sup>20</sup>

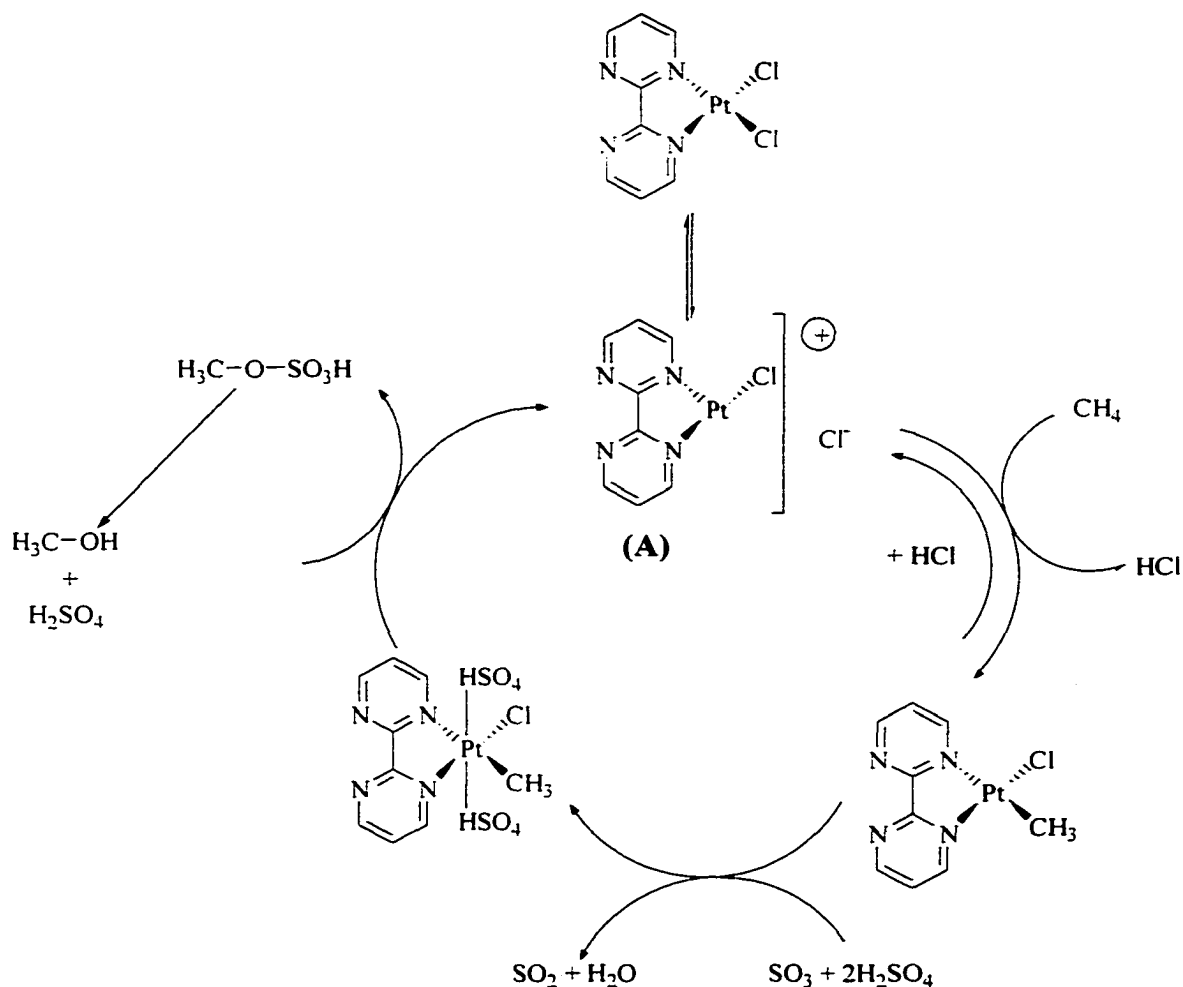


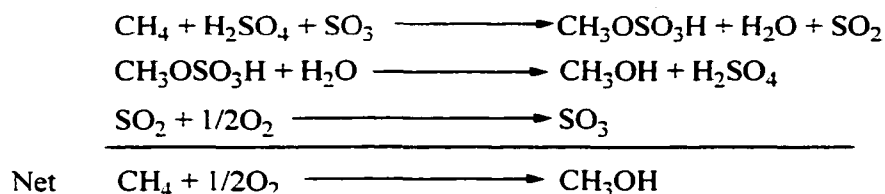
**Figure 7:** Reaction Mechanism for the Oxidation of Methane to Methanol on the Pt-Complex (A)<sup>19,20</sup>

This 14-electron platinum (II) complex remains catalytically active, converting methane to methylbisulfate, for 14 hours. During the catalytic cycle Pt (II) is oxidized to Pt (IV), a pathway similar to that reported by Shilov and co-workers in the early 1980's.<sup>11</sup>



Unfortunately subsequent work-up of the methylbisulfate requires long reaction times and hence may not be suitable for large-scale industrial applications.

This reaction sequence gives a reproducible 70% conversion of methane to methanol. The net reaction mechanism is summarised as:



Other processes have also been documented, however yields are often very low with large, unwanted side product formation taking place (such as the formation of formaldehyde).<sup>19</sup> In addition, many reactions routinely require the use of stoichiometric quantities of all reagents. Hence, these organometallic species cannot be considered as “true” catalysts.

### 1.1.3. Alternative Systems

In light of this past work, our primary goal was to successfully synthesise a stable low co-ordinate electron deficient transition metal species that would be capable of activating the C-H bonds of methane. In order to be successful, important considerations are to be made.<sup>21</sup>

- Scission of the C-H bond. This is generally accomplished at high reaction temperatures, however for optimum yields and hence low side product formation, reaction temperatures cannot be greater than the activation energy required for C-H bond scission. Thus for successful bond scission to take place lower reaction temperatures are preferred.

- Oxidation (addition of O<sub>2</sub>) to the reaction mixture generally occurs in the presence of a strong acid such as fuming sulphuric acid.<sup>21,22</sup> Thus the catalyst would need to survive and function under these harsh conditions.

Furthermore, we can conclude from the reactions mentioned in section 1.1.2, that in order to design a catalyst for the activation of methane, the complex must:

- be electron deficient at the metal centre
- be used as a “true” catalyst and not required in stoichiometric quantities
- not require photochemical activation
- behave as a redox active metal species

In addition careful considerations must be undertaken when choosing the appropriate ligand for the organometallic complex. For optimum results the chosen ligand should:

- be sufficiently bulky to inhibit dimerisation of the transition metal complex. When it is bonded to the transition metal, the bulky ligand group must prevent dimerisation while at the same time allow access to the metal centre by small molecules. (Wolczanski and Cummins<sup>13</sup>, **Figure 3**)
- donate a minimum number of electrons and have no  $\alpha$  lone pairs thus limiting  $\pi$ -donation to the metal atom and leading to a stronger interaction with the unsaturated metal intermediate. This would result in a higher degree of electron deficiency within the complex.
- not possess  $\alpha$  or  $\beta$  hydrogen's, which would result in non-selective addition occurring at the metal centre, such as  $\beta$  hydride elimination from the ligand to the metal atom.
- not possess acidic hydrogen's that can be easily removed by deprotonation reactions.

One ligand, which we believe fulfils the necessary criteria, has been previously reported.<sup>23,24</sup> **Figure 8.**

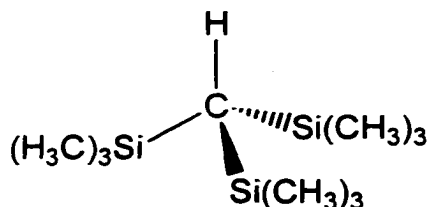


**Figure 8:** Tris(trimethylsilyl)methane, HTsi

Tris(trimethylsilyl)methane (HTsi) was first synthesised in the early 1960's by Merker and Scott.<sup>24</sup> The chemical properties of this ligand have been further explored in recent years by Eaborn and co-workers. There are two documented synthetic routes towards HTsi.<sup>25</sup> The first of these routes<sup>25a</sup> involves two synthetic steps: i) the reaction of TMSCl with 2 equivalents of lithium (wire) in THF leading to the production of TMSLi; ii) the reaction of TMSLi with chloroform leading to the formation of HTsi and LiCl. This approach takes up to one week for completion and the yields obtained are generally low.

The second approach<sup>25b</sup> is a one pot synthesis involving <sup>n</sup>BuLi, CHBr<sub>3</sub>, and an excess of TMSCl in THF. The reaction is slowly warmed over night from -78°C to room temperature. Subsequent work-up gives the desired product HTsi. This procedure gives repeatable 60-70 % yields and reaction times are generally no more than 24 hours.

HTsi readily undergoes metallation when treated with a strong base such as MeLi. The lithium salt is readily soluble in THF and the resulting product [Li(THF)<sub>4</sub>][{(Me<sub>3</sub>Si)<sub>3</sub>C}<sub>2</sub>Li], which is thought to lie in equilibrium with (Me<sub>3</sub>Si)<sub>3</sub>C<sup>•</sup>THF, is stable in solution for long periods of time.<sup>26</sup> The formation and

stability of the organolithium complex is possibly due to stabilisation of the carbanion  $(\text{Me}_3\text{Si})_3\text{C}^-$  by delocalisation of the negative charge into the  $\sigma^*$  non-bonding orbitals of the silicon atom. An area of possible concern is the stability of the radical  $[(\text{Me}_3\text{Si})_3\text{C}\bullet]$  formed in solution,<sup>26</sup> attributable to the delocalisation effect, and the ultimate formation of  $(\text{Me}_3\text{Si})_3\text{CC}(\text{SiMe}_3)_3$ .<sup>27</sup> Purification and subsequent characterisation via X-ray crystallographic methods of these alkali metal salts has shown these to be the first documented examples of polymeric alkali metal salt chains. Another important discovery in this area was the first characterised lithium 'ate' structure.<sup>28</sup> The  $\text{LiTsi}$  ligand is known to react readily (in good yields) with  $\text{Me}_3\text{MCl}$  ( $\text{M} = \text{Si}, \text{Ge}, \text{or Sn}$ ) to give the corresponding  $\text{TsiMMe}_3$  complexes.<sup>27,29</sup>

The ability of this ligand to enhance the overall stability and to impose remarkable steric hindrance at a metal centre has been emphasised via the formation of a thermally and chemically very stable  $\text{ZnTsi}_2$  species. This complex, unlike  $\text{ZnMe}_2$ , which spontaneously ignites in air, can be distilled in air<sup>30</sup> and melts without decomposition at  $300^\circ\text{C}$ .<sup>31</sup> The researchers determined that this inertness is due to the steric hindrance and hence large shielding effects that the ligand exerts on the metal atom face. A further reason for this stability is the lack of  $\alpha$  and  $\beta$  hydrogens on the ligand itself meaning that no  $\beta$  hydride elimination can occur. Other examples of very stable complexes formed include  $\text{MgClTsi}$ ,  $\text{MgTsi}_2$ ,  $\text{HgTsi}_2$ , and  $\text{CdTsi}_2$ . For the majority of these cases the materials were found to be thermally very stable and unusually unreactive.<sup>30</sup> With the exception of the manganese and cobalt cluster<sup>32</sup> species the area of development of M-Tsi formation has been limited to main group elements.

#### 1.1.4. Synthesis of an Electron Deficient Transition Metal Species

Before the present investigations were started, three synthetic approaches were planned for the synthesis of the electron deficient organometallic species. First we chose to investigate nucleophilic attack reactions of alkyl lithium salts (LiTsi and the bigger and less sterically demanding silicon species, Tris(trimethylsilyl)silyl lithium,  $\text{LiSiTsi}^{33}$ ) with a variety of transition metal complexes. These same organometallic species would then be taken and the reactions repeated using Sn-Tsi reagents in place of the lithium salt. The tin reagents would be used for two reasons: (a) if the reactions conducted with the lithium salt had resulted in the formation of unwanted by-products and (b) the zinc, magnesium and mercuric - Tsi reagents are extremely stable in their as-synthesised states; hence any reaction with an organometallic species would not have produced the desired product. Overall this approach should result in the formation of a M-Tsi complex where the formal oxidation state of the transition metal would have remained unchanged from that of the starting material

If this approach was unsuccessful, oxidative addition reactions, which are also a commonly used route in the synthesis of transition metal alkyl complexes, could then be studied as a means of synthesising the target complexes. Likely candidates as inorganic precursors would be  $d^8$  square planar low valent organometallic species such as  $\text{Ir(I)}^{34,35}$  or  $\text{Rh(I)}^{36}$  which are known to react with an XY (where X is Cl, Br, I or C and Y = C, X or H) molecule resulting in a product in which both the oxidation number and coordination number of the metal are increased by two. The ligand precursor of choice for these reactions is a halogenated analogue of the Tsi species, ITsi.<sup>37</sup> Generally C-I alkyls have been used for oxidative addition reactions due to the relatively weak C-I bond

strength. Furthermore, oxidative addition reactions with R-X species and Vaska's complex, or the Rh analogue,<sup>36</sup> have been known to proceed via an S<sub>N</sub>2 pathway with the relative rates of these reactions in the order of X = I > Br > Cl. However, to date there has been no documented evidence to suggest that oxidative addition of I-Tsi will proceed via an S<sub>N</sub>2 pathway.

Finally, we could also resort to free radical attack employing a radical form of the ligand species. This is a potential route for the formation of a transition metal alkyl complex via a one-electron oxidation process. Documented reports have indicated that the Tsi ligand can exist as relatively stable radical species in solution.<sup>26</sup> Therefore, free radical attack of this species or the silicon analogue, tris(trimethylsilyl)silane, HSiTsi,<sup>34</sup> may lead to the formation of a M-Si bond. As with all free radical transformations, three steps must be considered: initiation, one electron transfer and termination. For example, in the case of a free radical reaction involving HSiTsi, the following would potentially occur:

- i. initiation with the formation of H• and •Si(TMS)<sub>3</sub> radicals
- ii. an electron transfer to the organometallic species from the alkyl group (giving an M-R species) and finally
- iii. termination of the free radicals in solution by R• + •R to give R-R.

In summary, this thesis will investigate the synthesis of an electron deficient transition metal – Tsi complex via nucleophilic attack reactions of transition metal alkyl salts using i) LiTsi, ii) LiSiTsi or iii) R<sub>3</sub>Sn-Tsi reagents (R = Me or <sup>n</sup>Bu). If these attempts are not successful, oxidative addition reactions will be investigated and the reactions of I-Tsi across four co-ordinate Ir(I), Rh(I) and Ru(II) centres will also be studied. Finally, free radical reactions could also be explored using HSiTsi as the ligand species, as a means of synthesising the target complexes.

## 1.2. Results and Discussion

### 1.2.1. LiTsi

LiTsi was synthesised according to the literature.<sup>38</sup> Once purified, the salt was stored under an inert atmosphere and was stable for long periods of time. All reactions between the organometallic species and LiTsi were monitored using multinuclear NMR spectroscopy ( $\delta$  ppm).  $^1\text{H}$  NMR:  $\delta$  0.46 ppm ((Si(CH<sub>3</sub>)<sub>3</sub>)<sub>3</sub>), 27H, s),  $\delta$  1.99 ppm (THF, 4H, m),  $\delta$  3.27 ppm (THF, 4H, m) and  $^{13}\text{C}$  { $^1\text{H}$ } NMR  $\delta$  7.9 ppm (TMS, 9C, s),  $\delta$  25.3 ppm (THF, 2C, s),  $\delta$  68.2 ppm (THF, 2C, s), no resonance was observed for the quaternary carbon of the lithium salt.<sup>38</sup> **Figure 9(a) and (b)** respectively.

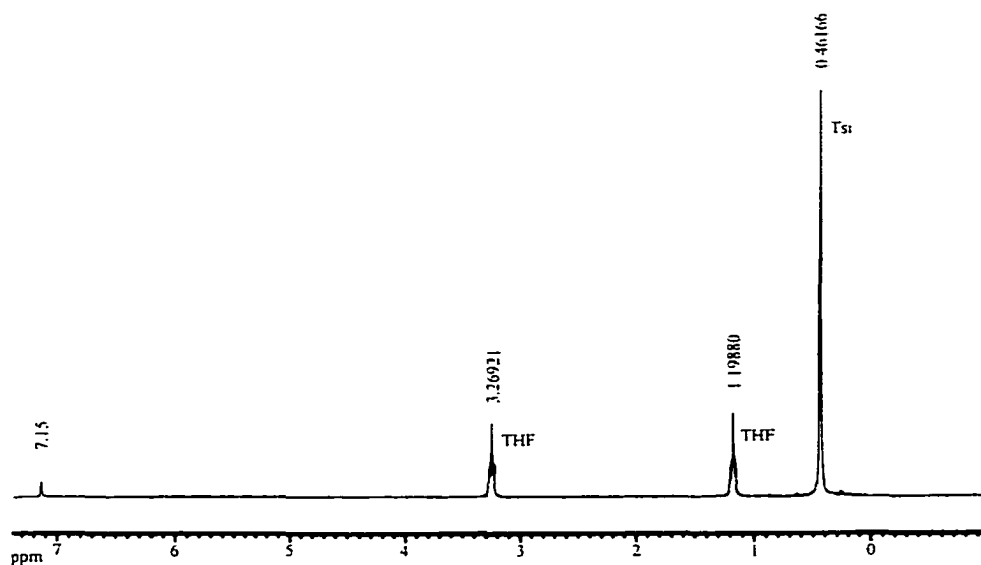


**Figure 9(a):**  $^1\text{H}$  NMR of LiTsi in C<sub>6</sub>D<sub>6</sub>

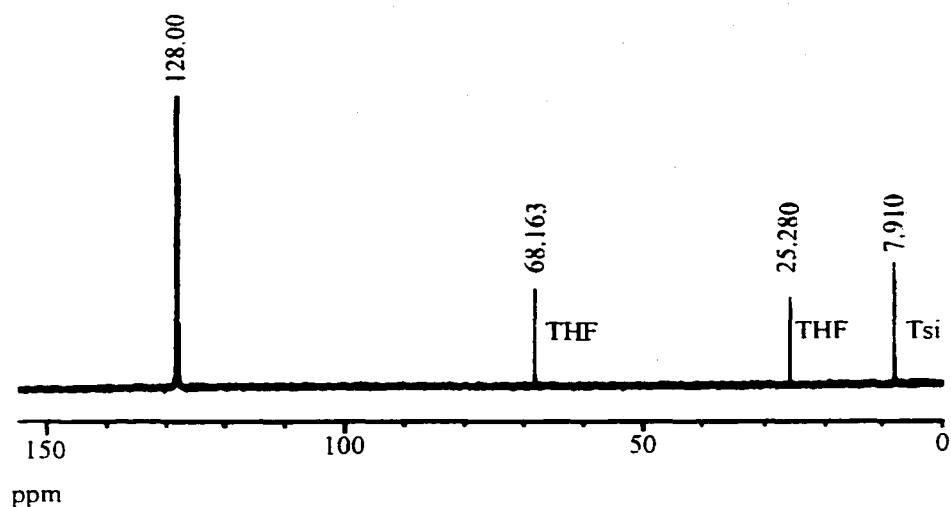


**Figure 9(b):**  $^{13}\text{C}$   $\{^1\text{H}\}$  NMR of LiTsi in  $\text{C}_6\text{D}_6$

To date numerous reactions have been conducted using LiTsi as a nucleophile.<sup>27-32</sup> Some inorganic precursors used include:  $\text{Me}_3\text{GeCl}$ ,  $\text{Me}_3\text{SnCl}$ ,  $\text{PbCl}_2$ ,  $\text{ZnCl}_2$ ,  $\text{CdCl}_2$ ,  $\text{KCl}$ ,  $\text{CsCl}$ ,  $\text{MgCl}_2$ . In 1985 Eaborn and co-workers documented the synthesis of a Manganese tri-cluster,  $[\text{Li}(\text{THF})_4][\text{Tsi}_3\text{Mn}_3\text{Cl}_4(\text{THF})]^{32}$  (**Figure 10**), as evidenced by X-ray crystallography. This organometallic Mn-tri-cluster was synthesised via a 1:1 stoichiometric reaction between LiTsi and  $\text{MnCl}_2$  at  $-78^\circ\text{C}$  in THF.

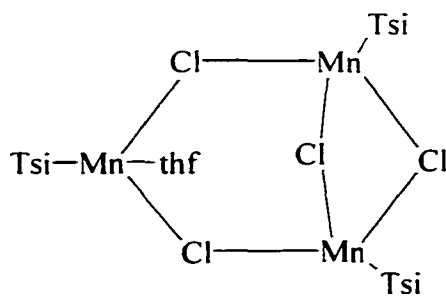


**Figure 10:** Mn-Tsi Cluster



A related cobalt complex was also synthesised via the reaction of  $\text{CoCl}_2$  and  $\text{LiTsi}$  in THF at  $-78^\circ\text{C}$  under an inert atmosphere of nitrogen, however the crystals could not be unambiguously characterised. Both the Mn and Co complexes isolated were paramagnetic and hence difficult to characterise via  $^1\text{H}$  NMR spectroscopic analysis.<sup>32</sup>

Further advances by Eaborn and co-workers demonstrated that when two equivalents of  $\text{LiTsi}$  were reacted with  $\text{MnCl}_2$  in THF a very stable air sensitive di-alkyl manganese complex,  $\text{Mn}(\text{Tsi})_2$  was isolated.<sup>39</sup>

### 1.2.2. $\eta$ -Benzenedichloro(triphenylphosphine)ruthenium (II)

In the early 1970's Zelonka and Baird<sup>40</sup> first reported the synthesis and chemical properties of a wide range of  $\text{RuCl}_2(\text{arene})\text{L}$  ( $\text{L} = \text{PPh}_3$ ) complexes and provided evidence that these species are monomeric in solution. These results were later corroborated by independent studies conducted on similar complexes by Bennett and Smith.<sup>41</sup> Due to the fact that these species are monomeric in solution, and that they contain labile  $\text{PPh}_3$  and  $\text{C}_6\text{H}_6$  moieties, we believed  $\text{RuCl}_2(\text{C}_6\text{H}_6)\text{PPh}_3$  would be an ideal organometallic precursor for our investigations.

When  $\text{LiTsi}$  (222 mg, 0.488 mmol) was added to a stirred solution of  $\text{RuCl}_2\text{C}_6\text{H}_6(\text{PPh}_3)$  (250 mg, 0.488 mmol) in  $\text{C}_6\text{D}_6$  an immediate colour change was observed from orange to deep red. A fraction of the reaction mixture was isolated and monitored via  $^1\text{H}$  NMR and  $^{13}\text{C}$   $\{^1\text{H}\}$  NMR spectroscopy. The  $^1\text{H}$  NMR spectrum is shown in **Figure 11(a)** and indicates the formation of  $\text{HTsi}$  and a new  $\text{Tsi}$  species at 0.36 ppm.

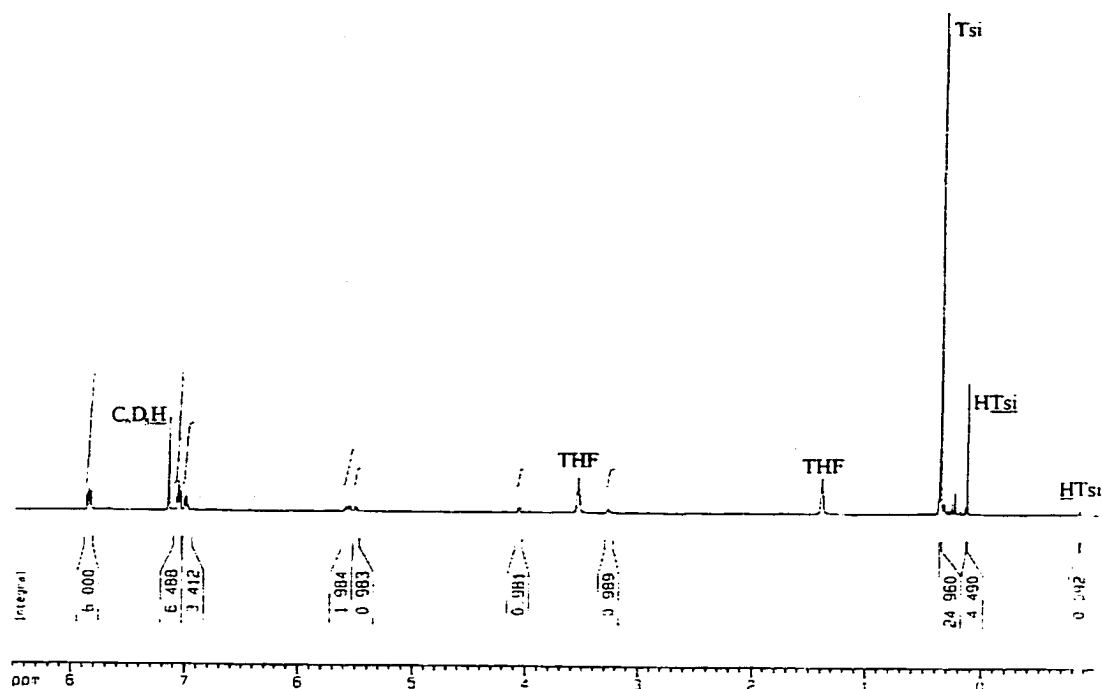


**Figure 11(a):**  $^1\text{H}$  NMR Spectrum for the Product Obtained from the Reaction between  $\text{RuCl}_2\text{C}_6\text{H}_6(\text{PPh}_3)$  and  $\text{LiTsi}$  in  $\text{C}_6\text{D}_6$

The  $^1\text{H}$  NMR spectrum of the starting material ( $\text{RuCl}_2(\text{C}_6\text{H}_6)\text{PPh}_3$ ) contains a broad multiplet resonance due to the phenyl groups of the  $\text{PPh}_3$  species and a sharp singlet, approximately 2.0 ppm upfield of free benzene, indicative of the co-ordinated  $\eta^6\text{-C}_6\text{H}_6$ . Due to the rapid rotation of the benzene ring on the NMR time scale, proton equivalence is observed for the starting material giving an integration ratio of 15:6 (phenyl:  $\eta^6\text{-benzene}$ ). Intriguingly, the expected proton integration ratio of 15:6:27 for the phenyl: $\eta^6\text{-benzene}$ :Tsi (**Figure 11(a)**) is not observed and is in fact 15:2:1:1:1:27. These resonances reflect that 5 and not 6 protons are present on the  $\eta^6\text{-benzene}$  ring and that these protons are not equivalent to one another.

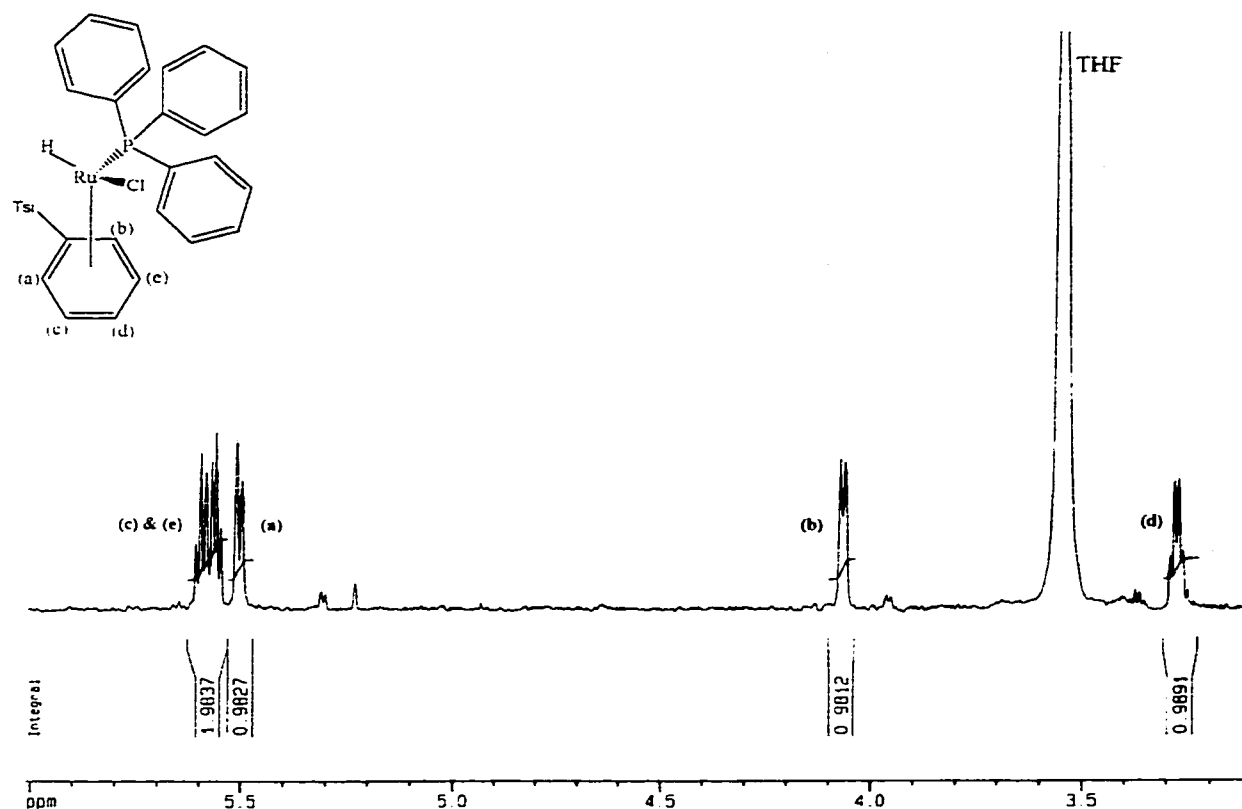


**Figure 11(b):** Enlargement of  $^1\text{H}$  NMR from 10 (a) Illustrating the Benzyl Region

For this reason we considered the possibility that while the reaction may have initially proceeded with the formation of the desired Ru-Tsi species, a rapid ring substitution of one proton for the Tsi moiety on to the Ru metal centre may have occurred (**Scheme 2**). This would have resulted in the formation of  $\eta^6\text{-C}_6\text{H}_5\text{Tsi}$  and a ruthenium hydride species.<sup>42</sup>

In fact, a resonance for a Ru-bound hydride atom is observed in the high-field region of the  $^1\text{H}$  NMR spectrum (**Figure 11( c)**) as a doublet at  $-6.17$  ppm.

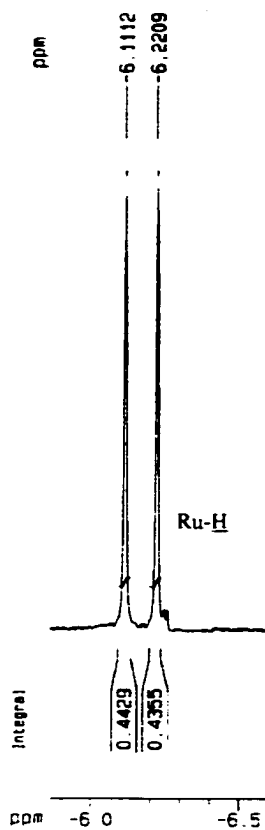
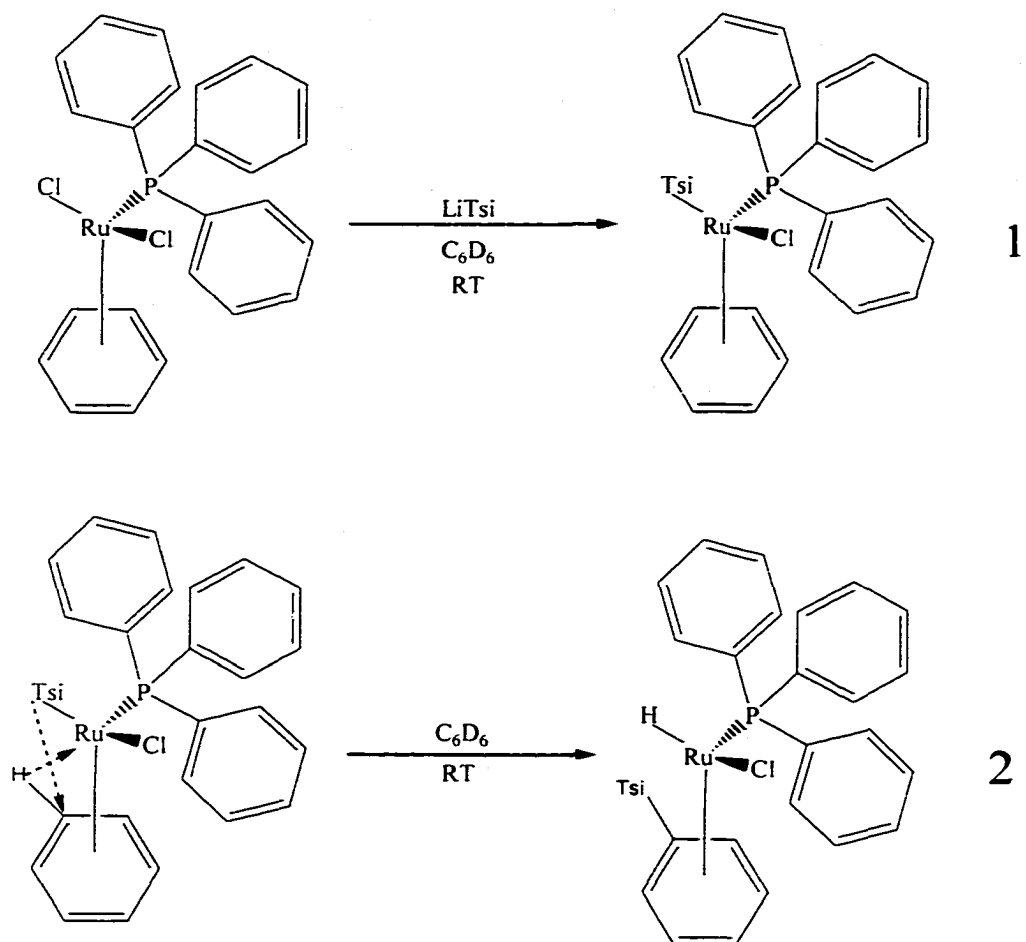


**Figure 11 (c):**  $^1\text{H}$  NMR Spectrum for Ru-H Region

The presence of this doublet species clearly indicates that there is a degree of interaction between the hydride ( $\text{M-H}$ ) and a neighbouring species, the phosphorous atom of  $\text{PPh}_3$ . The calculated coupling constant for the observed spin-spin splitting is equal to  $J_{\text{H-P}} = 32.91$  Hz. The presence of this hydride species gives us conclusive evidence that the reaction product is the stable 18-electron Ru (II) species **2** shown in **Scheme 2**.



**Scheme 2:** Proposed Mechanism for the Reaction of  $RuCl_2C_6H_6(PPh_3)$  with LiTsi in  $C_6D_6$ .

Brookhart, Lamanna and Humphrey documented similar results in 1981.<sup>43</sup> From these studies the researchers spectroscopically confirmed a three-centre interaction between the transition metal (Mn) centre and a C-H bond bound to the ligand co-ordinated to the organometallic. **Figure 12.**

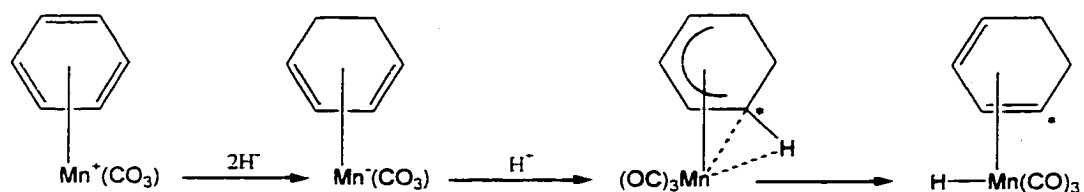


**Figure 12:** Hydride Migration from the Bound Ligand to the Metal Centre.<sup>43</sup>

Because of this three-centre interaction, the bridging proton becomes more acidic, thus deprotonation and migration to the metal centre is facilitated and the  $C^*$  becomes active for electrophilic substitution reactions.

These data indicate that while the desired Ru-Tsi species may have formed, the Ru-Tsi bond destabilised resulting in an internal ring substitution reaction and hence the formation of  $RuClH(C_6H_5Tsi)PPh_3$ .

### 1.2.3. LiSiTsi

Since reactions conducted between LiTsi and the organometallic precursors did not yield the desired transition metal complexes, we chose to investigate a related ligand species, LiSiTsi. It was possible that the observed side product formation was influenced by the steric demands enforced on the transition metal atom by the Tsi organic moiety and for this reason the use of LiSiTsi (which is bigger and less sterically demanding than LiTsi) as the ligand species would result in the formation of the desired transition metal species, M-SiTsi.

LiSiTsi was prepared according to the literature.<sup>44</sup> Independent studies have documented on reactions of LiSiTsi with Zr<sup>45</sup> and Ta<sup>46</sup> organometallic species; however, in these reports dimerisation of the organometallic complexes and elimination of methyl groups from the ligand was observed. This was primarily due to the formation of free radical SiTsi fragments.

During the present investigations, reactions conducted between LiSiTsi and organometallic species such as RhCl(PPh<sub>3</sub>)<sub>3</sub>, [IrCl(CO)(PPh<sub>3</sub>)<sub>2</sub>], [RhCl(CO)(PPh<sub>3</sub>)<sub>2</sub>], RuCl<sub>2</sub>(C<sub>6</sub>H<sub>6</sub>)PPh<sub>3</sub> and MnCl<sub>2</sub> led to the synthesis of several unidentifiable products.

Wilkinson's catalyst, RhCl(PPh<sub>3</sub>)<sub>3</sub> is known to dissociate in solution to give RhCl(PPh<sub>3</sub>)<sub>2</sub> + PPh<sub>3</sub>. Because of the extra co-ordination site available upon phosphine dissociation it was anticipated that the reaction between the organometallic species and LiSiTsi would result in the formation of a Rh(I)SiTsi product. When LiSiTsi (40 mg, 0.122 mmol) was added to RhCl(PPh<sub>3</sub>)<sub>3</sub> (113 mg, 0.122 mmol) in C<sub>6</sub>H<sub>6</sub> a change in colour from orange to very dark red was observed followed by the formation of a dark precipitate. Initial spectroscopic analysis indicated a new SiTsi species at  $\delta$  0.19 ppm (**Figure 13(a)**) for the <sup>1</sup>H NMR spectrum and a resonance at 0.5 ppm for the <sup>13</sup>C {<sup>1</sup>H} NMR spectrum.

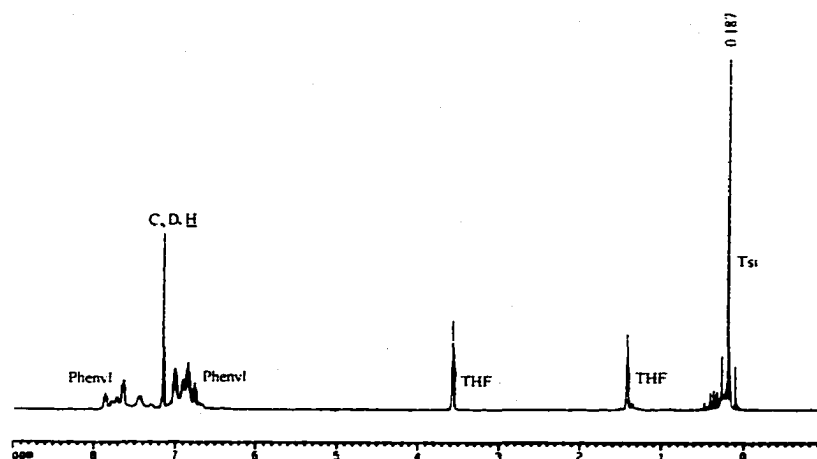


**Figure 13(a):**  $^1\text{H}$  NMR of the Product Obtained from the Reaction between Wilkinson's Catalyst and LiSiTsi in  $\text{C}_6\text{D}_6$

While the  $^{31}\text{P}$   $\{^1\text{H}\}$  NMR spectrum showed the presence of  $\text{RhCl}(\text{PPh}_3)_3$ ,  $\text{RhCl}(\text{PPh}_3)_2$  and a new product at  $\delta$  25.2 ppm, no resonance was observed for free  $\text{PPh}_3$  (-5 ppm). Purification of the reaction mixture led to the isolation of orange needle shaped crystals. The  $^{31}\text{P}$   $\{^1\text{H}\}$  NMR spectrum of the crystals showed a single resonance ( $\delta$  25.2 ppm) and not the expected doublet, which would have been consistent with phosphorous Rh coupling and hence the formation of  $\text{Rh}(\text{PPh}_3)_3\text{SiTsi}$ . **Figure 13(b)**



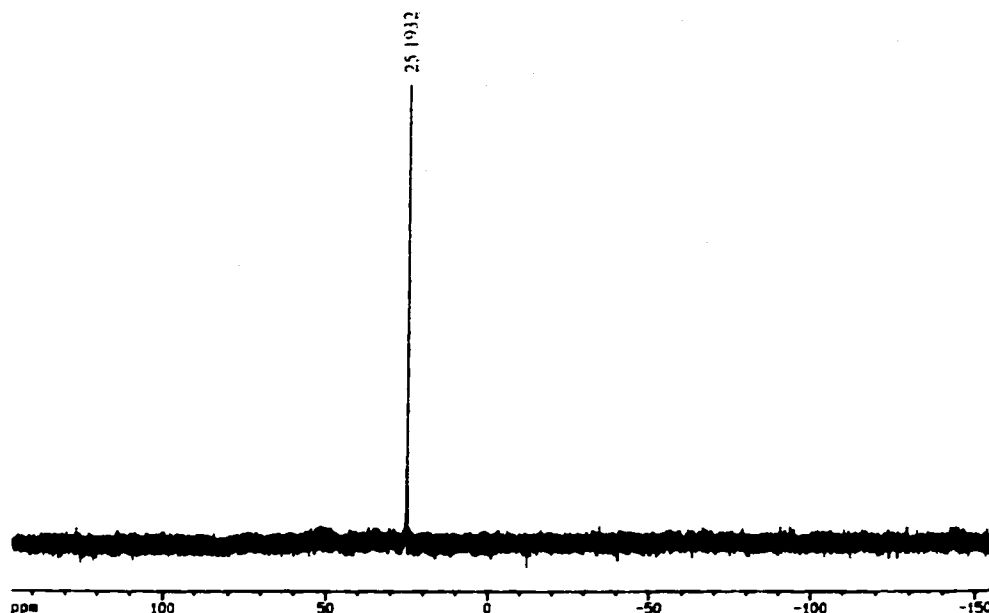


**Figure 13(b):**  $^{31}\text{P}$   $\{^1\text{H}\}$  NMR of the Crystals Obtained from the Reaction between Wilkinson's Catalyst and LiSiTsi in  $\text{C}_6\text{D}_6$

Therefore, while initial NMR analysis indicated the formation of a new M-SiTsi species, this organometallic compound was not stable and decomposition subsequently occurred.

Stoichiometric reactions conducted with Vaska's compound  $[\text{IrClCO}(\text{PPh}_3)_2]$  and its rhodium analogue  $[\text{RhClCO}(\text{PPh}_3)_2]$  at  $-78^\circ\text{C}$ . with LiSiTsi resulted in the formation of many products as evidenced by the multiple resonances within the TMS region in the  $^1\text{H}$  NMR spectrum. Cleavage of the TMS groups and subsequent migration from the ligand to the metal could account for the presence of these resonances.  $\text{Si}(\text{TMS})_4$  (achieved via TMS migration) was also formed during the course of these investigations as evidenced by the resonance at 0.26 ppm in the  $^1\text{H}$  NMR spectrum. Similar observations to those above were made for the reaction of  $\text{RuCl}_2(\text{C}_6\text{H}_6)\text{PPh}_3$  and LiSiTsi.

When LiSiTsi (130 mg, 0.397 mmol) was added to MnCl<sub>2</sub> (50 mg, 0.397 mmol) in THF at -78°C a change in colour from pale yellow to dark yellow was observed. Crystallisation of a saturated solution of the reaction product from hexane at -37°C led to the isolation of small yellow and orange paramagnetic crystals. These rapidly decomposed upon warming and because of this X-ray crystallography proved to be difficult. The <sup>1</sup>H NMR spectrum of these crystals in deuterated benzene showed very broad resonances, indicative of paramagnetic Mn (II) species present.

#### 1.2.4. Oxidative Addition Reactions with ITsi

An alternative approach to the synthesis of an electron deficient transition metal complex is via oxidative addition reactions across four co-ordinate Ir(I),<sup>34,35</sup> Rh(I)<sup>36</sup> and Ru(II)<sup>37</sup> complexes with iodo-tris(trimethylsilyl)methane, ITsi.<sup>38</sup> Oxidative addition reactions have been well documented, for example the reaction of MeI or MeOTf (OTf = SO<sub>3</sub>CF<sub>3</sub>) with Vaska's complex [IrCl(CO)(PPh<sub>3</sub>)<sub>2</sub>] gives the octahedral Ir (III) species [IrCl(CO)(X)Me(PPh<sub>3</sub>)<sub>2</sub>], (X = I or OTf). By analogy it appeared that ITsi would work in a similar manner. For this reason it was anticipated that oxidative addition of ITsi across the four co-ordinate transition metal species would be a favourable reaction. ITsi was prepared according to the literature,<sup>38</sup> is air stable and upon purification gives white crystalline needles.

When ITsi (15 mg, 0.0404 mmol) was added to [IrCl(CO)(PPh<sub>3</sub>)<sub>2</sub>] (28 mg, 0.0404 mmol) in C<sub>6</sub>D<sub>6</sub> no initial colour change of the reaction mixture was observed. The solution mixture was transferred to a sealed NMR tube and heated for 30 minutes at 50°C. Monitoring of the reaction mixture via <sup>1</sup>H NMR spectroscopy showed that no new

product(s) were formed. The sample was further heated at 100°C for 12 hours then 150°C for 8 hours. With each increase in temperature the reaction progress was monitored via NMR analysis, however even at temperatures greater than 150°C no new product(s) were observed. Identical results to those given above were noted when  $[\text{RhCl}(\text{CO})(\text{PPh}_3)_2]$  was reacted with ITsi under the same experimental conditions. We attribute these observations to the sheer steric bulk surrounding the iodine atom, although this halogen itself is known to be large in spherical diameter.

Since attempts at the oxidative addition reactions did not result in the formation of the desired I-M-Tsi species, attempts were made to synthesise the ionic triflate analogue  $\text{TsiSO}_3\text{CF}_3$ . If successful the new ligand would, due to the fact that the triflate species is a good leaving group, be an ideal candidate for electrophilic attack reactions to the organometallic species. Unfortunately, the direct reaction between ITsi and  $\text{AgSO}_3\text{CF}_3$  did not result in the formation of  $\text{TsiSO}_3\text{CF}_3$  as evidenced from the  $^1\text{H}$  and  $^{13}\text{C}$   $\{^1\text{H}\}$  NMR spectra. These findings were consistent with our previous observations regarding the high steric bulk surrounding the X species. (X = halogen,  $\text{SO}_3\text{CF}_3$ )

### 1.2.5 Free Radical Reactions with HSiTsi

Tris(trimethylsilyl)silane, HSiTsi, is known to readily undergo free radical reactions,<sup>26</sup> is sterically bigger<sup>37</sup> and possibly more reactive than HTsi.<sup>47</sup> For these reasons, attempts to react HSiTsi directly with organometallic precursors (such as  $[\text{IrCl}(\text{CO})(\text{PPh}_3)_2]$ ,  $[\text{IrClCOD}]_2$ ,  $[\text{RhCl}(\text{CO})(\text{PPh}_3)_2]$ ,  $[\text{RhCl}(\text{CO})_2]_2$  or  $\text{RhCl}(\text{PPh}_3)_3$ ) were undertaken. Unfortunately, the reactions conducted did not provide evidence for the formation of the desired M-SiTsi products. Spectroscopic analysis for the reactions

conducted between  $[\text{IrCl}(\text{CO})(\text{PPh}_3)_2]$  or  $[\text{RhCl}(\text{CO})(\text{PPh}_3)_2]$  and  $\text{HSiTsi}$  in  $\text{C}_6\text{D}_6$  did indicate TMS group migration within these systems as many new resonances in the TMS region of the spectra were observed. These observations were consistent with the results obtained from the reactions of  $\text{LiSiTsi}$  with  $[\text{IrCl}(\text{CO})(\text{PPh}_3)_2]$ ,  $[\text{RhCl}(\text{CO})(\text{PPh}_3)_2]$  and  $\text{RuCl}_2(\text{C}_6\text{H}_6)\text{PPh}_3$ .

### 1.3. Early Transition Metals:

#### 1.3.1. The Pentachlorides of Niobium and Tantalum

The information extracted from investigations with the late transition metal species and  $\text{LiTsi}$  suggested that no new organometallic materials had been isolated and that side product formation dominated the reactions. For this reason an investigation of early transition metal (V)  $d^0$  precursors was undertaken. These precursors have an electron count equal to 10 and hence are extremely electron deficient and highly coordinatively unsaturated.<sup>48</sup>

When a solution of  $\text{LiTsi}$  (168 mg, 0.37 mmol) in toluene was added dropwise to a stirred solution of  $\text{NbCl}_5$  (100 mg, 0.37 mmol) in toluene, a change in colour from orange to dark brown was observed. The solution was filtered and a dark brown precipitate was removed. The filtrate was reduced in volume resulting in the isolation of a pale yellow oily residue, which was recrystallised, from hexane at  $-37^\circ\text{C}$ . The crystals obtained were characterised via  $^1\text{H}$  NMR,  $^{13}\text{C}$   $\{^1\text{H}\}$  NMR spectroscopy and X-ray crystallography. **Figure 14(a), (b) and (c)** respectively. Intriguingly, the analytical data confirmed that no Nb had been incorporated into the product, but instead the reaction had resulted in the formation of a new organic species designated benzyl-Tsi.

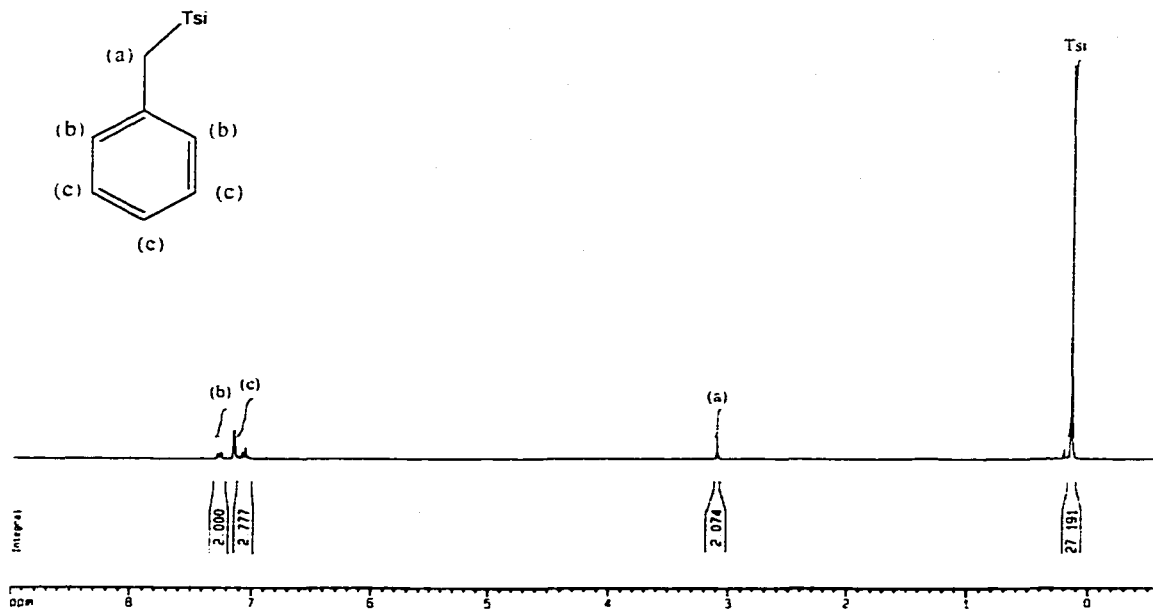


**Figure 14(a):**  $^1\text{H}$  NMR of Benzyl-Tsi in  $\text{C}_6\text{D}_6$

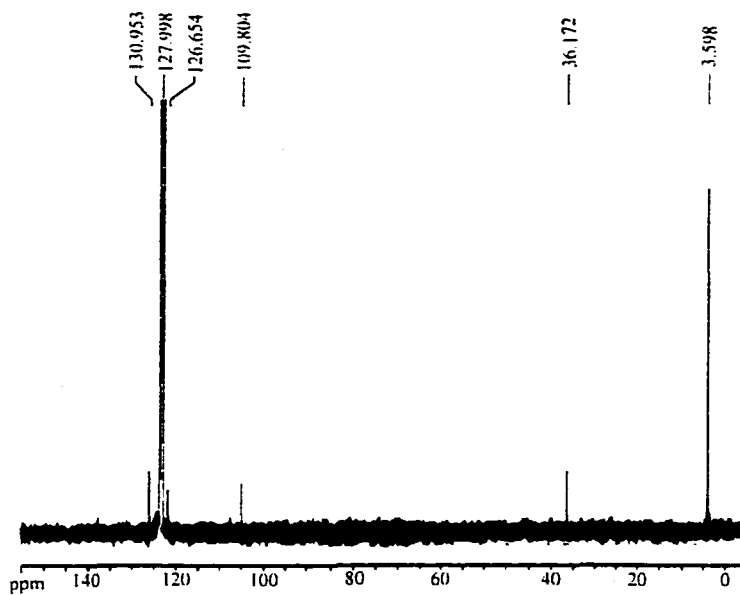


**Figure 14(b):**  $^{13}\text{C}$   $\{^1\text{H}\}$  NMR of Benzyl-Tsi  $\text{C}_6\text{D}_6$

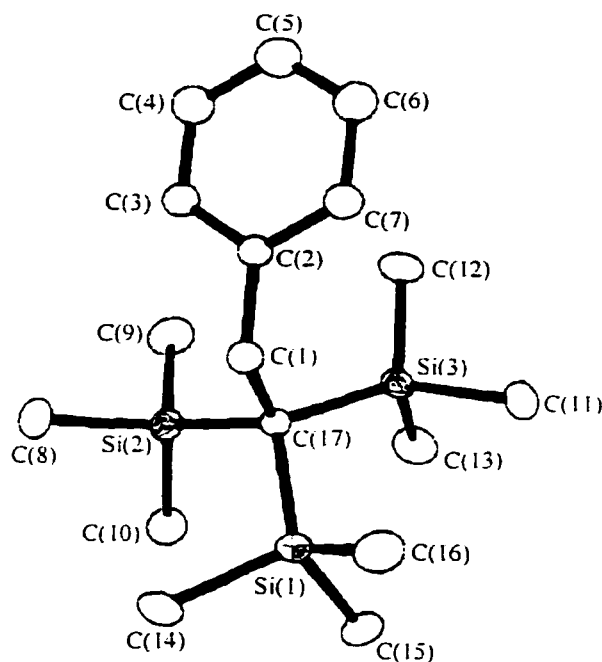


**Figure 14(c):** X-ray Structure of Benzyl-Tsi

Due to the formation of this organic species, low temperature NMR experiments were conducted at  $-90^{\circ}\text{C}$  in  $d^8$ -toluene to elucidate the reaction process. These were achieved by monitoring the formation of benzyl-Tsi and HTsi over time via  $^1\text{H}$ -NMR spectroscopy.

Dried and degassed  $d^8$ -toluene was vacuum transferred into a NMR tube cooled to 77K containing a 1:1 stoichiometric mixture of  $\text{TaCl}_5$  (or  $\text{NbCl}_5$ ) and LiTsi. The sample tube was stored in liquid nitrogen until ready for use. NMR analysis of the reaction mixture started at  $-90^{\circ}\text{C}$  and the spectra were recorded at  $10^{\circ}\text{C}$  increments up to room temperature. Initial  $^1\text{H}$  NMR spectroscopic results revealed that over a 20 degree span ( $-90$  to  $-70^{\circ}\text{C}$ ) resonances were only observed for LiTsi-(THF) and toluene. The spectrum at  $-60^{\circ}\text{C}$  showed the presence of toluene, HTsi and minor amounts of LiTsi.

Resonances attributed to benzyl-Tsi were first observed at  $-50^{\circ}\text{C}$ . Complete formation of both benzyl-Tsi and HTsi was reached at  $-30^{\circ}\text{C}$ . Furthermore, complete consumption of LiTsi was observed at this temperature as no  $^1\text{H}$  NMR resonance was detected for this species. Above  $-30^{\circ}\text{C}$  no further changes in the resonance intensities attributed to benzyl-Tsi and HTsi were observed. From the information obtained we were able to confirm that HTsi formation occurred prior to the synthesis of benzyl-Tsi. Unfortunately, the low temperature NMR spectrum did not provide any conclusive information about the reaction mechanism.

To probe solvent dependence in the formation of this organic material we chose to investigate different solvents: namely THF for  $\text{NbCl}_5$ <sup>\*</sup> and benzene for both  $\text{NbCl}_5$  and  $\text{TaCl}_5$ . In all cases the formation of the protonated species HTsi was apparent but no evidence for the formation of R-Tsi was observed, where R is the solvent used for the reaction, indicating that the formation of R-Tsi occurred only in the presence of toluene. Following these investigations, a reaction between  $\text{TaBr}_5$  and LiTsi in toluene was performed. Bromides are commonly used for electron transfer reactions due to the larger  $\text{Br}^-$  ion in comparison to  $\text{Cl}^-$ <sup>9</sup>. The addition of LiTsi to a toluene solution of  $\text{TaBr}_5$  led to an observed colour change from pale yellow/orange to green. Upon solvent removal from the reaction mixture, an olive green oil was isolated. The  $^1\text{H}$  NMR spectrum ( $\text{C}_6\text{D}_6$ ) of this oil showed the formation of benzyl-Tsi and HTsi, indicating that this organic species was obtained via an electron transfer between the Ph or Tsi alkyl groups and the metal atom (Ta).

---

<sup>\*</sup>Due to the possibility of polymerisation of the solvent, a reaction using  $\text{TaCl}_5$  in THF was omitted.

From this information three hypothetical reaction sequences for the formation of benzyl-Tsi were proposed. First, the synthesis of benzyl-Tsi might have occurred via a free radical pathway, as illustrated below.

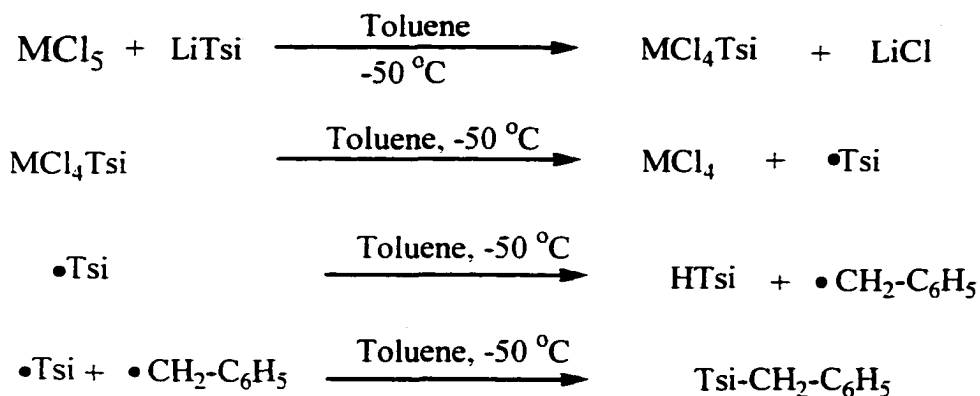
- a) The possible formation of  $M(\text{CH}_2\text{Ph})\text{Cl}_4$ , ( $M = \text{Nb}$  or  $\text{Ta}$ ). The independent syntheses for both the  $\text{Ta}(\text{CH}_2\text{Ph})_n\text{Cl}_{5-n}$  and  $\text{Nb}(\text{CH}_2\text{Ph})_n\text{Cl}_{5-n}$  ( $n = 1,2,3,4$ ) materials have been previously documented.<sup>50</sup> However, the spontaneous formation of these M-phenyl species has not been reported.
- b) If  $M(\text{CH}_2\text{Ph})\text{Cl}_4$  had been spontaneously formed, nucleophilic attack at the metal centre by LiTsi would have led to the production of the unstable  $\text{TsiM}(\text{CH}_2\text{Ph})\text{Cl}_3$ .
- c) Due to steric demands exerted on to the metal centre by the addition of the bulky Tsi group, a one-electron transfer from the phenyl group to the metal atom would have resulted in the loss of a  $\bullet\text{CH}_2\text{Ph}$  radical in solution.
- d) Similarly, a one-electron transfer from the Tsi group to the metal atom would have resulted in the loss of  $\bullet\text{Tsi}$  radicals in solution.
- e) If both radical species were produced, they could have potentially combined in solution giving  $\text{Tsi-CH}_2\text{Ph}$ . The reduced organometallic species, believed to be the insoluble brown precipitate obtained, was removed via filtration from the reaction mixture.

This hypothesis was rejected since the spontaneous formation of  $M(\text{CH}_2\text{Ph})\text{Cl}_4$  is not feasible from  $\text{NbCl}_5$  (or  $\text{TaCl}_5$ ) and toluene and furthermore, formation of the radicals  $\bullet\text{CH}_2\text{Ph}$  and  $\bullet\text{Tsi}$  would have resulted in the isolation of three products, benzyl-Tsi,  $\text{PhCH}_2\text{-CH}_2\text{Ph}$  and  $\text{Tsi}_2$ . The spectroscopic data obtained for the reaction mixture did not



indicate the formation of either PhCH<sub>2</sub>-CH<sub>2</sub>Ph or Tsi<sub>2</sub> but only showed the isolation of TsiCH<sub>2</sub>Ph.

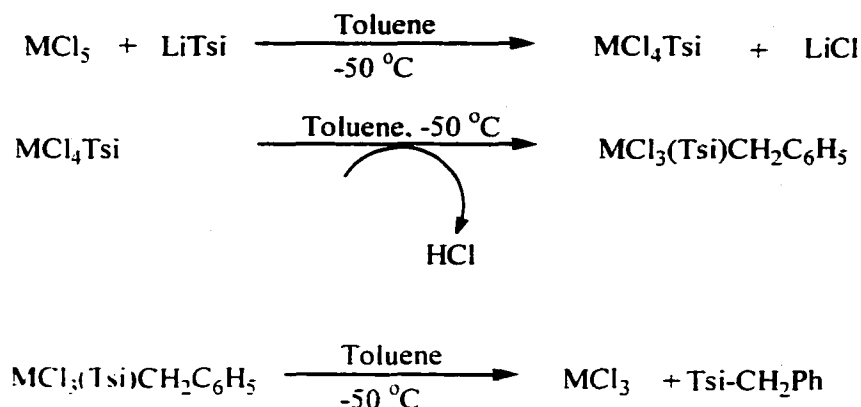
Our second hypothetical reaction sequence could have possibly involved the formation of the Tsi radical species as illustrated in **Scheme 3**.



**Scheme 3:** Second Proposed Hypothetical Reaction Sequence for the Formation of Benzyl-Tsi

Due to the large steric demands imposed on the metal centre by the Tsi organic moiety, destabilisation of the MCl<sub>4</sub>Tsi species could have led to a one-electron reduction of the transition metal complex and the formation of •Tsi. Since toluene is present in excess, free radical attack could have resulted with the formation of benzyl-Tsi, and •H and •CH<sub>2</sub>Ph radicals. **Scheme 3** illustrates the development of these radical species however, as with the first hypothesis, the expected side products formed from this mechanism would have also included Tsi<sub>2</sub>, PhCH<sub>2</sub>-CH<sub>2</sub>Ph and H<sub>2</sub>. These organic moieties were not detected during spectroscopic analysis of the reaction mixture and hence this pathway must also be rejected.

Finally we considered a two-electron reductive elimination pathway. **Scheme 4.**



**Scheme 4:** Proposed Reductive Elimination Pathway for the Formation of Benzyl-Tsi

One downfall of this proposed pathway is the formation of the extremely electron deficient  $\text{M(III)Cl}$  species. Stabilisation of this complex would be required and could have been achieved either by dimerisation of the organometallic complex or by solvent co-ordination. Furthermore, this electron deficient complex could have potentially reacted with the hydrochloric acid formed during the course of the reaction leading to the regeneration of the  $\text{M(V)}$  species.

As mentioned previously the formation of the protonated starting material, HTsi, was also observed by  $^1\text{H}$  and  $^{13}\text{C}$   $\{^1\text{H}\}$  NMR spectroscopy. Due to this observation vigorous redrying and degassing of all solvents and purification of all starting materials was undertaken.

Interestingly, in the absence of solvent, HTsi was also formed when a mixture of LiTsi and  $\text{TaCl}_5$  were heated to  $50^\circ\text{C}$  for 1 hour. The presence of this species, as shown by  $^1\text{H}$  NMR spectroscopy, was possibly due to the deprotonation of a THF solvent

molecule (co-ordinated to the LiTsi starting material). We have observed that HTsi is not formed when LiTsi is heated in C<sub>6</sub>D<sub>6</sub> for long periods of time and hence the formation of the protonated ligand is thus influenced by the presence of the organometallic species in solution or solid state.

### 1.3.2. Trimethyl Tantalum Dichloride

When LiTsi (153 mg, 0.336 mmol) was added to TaMe<sub>3</sub>Cl<sub>2</sub> (100 mg, 0.336 mmol) in d<sup>8</sup>-toluene at -20°C a change in colour from pale yellow to very dark brown, followed by evolution of gas was observed. A fraction of the reaction mixture was monitored at -20°C via <sup>1</sup>H NMR spectroscopy. The analysis showed the formation of the organic benzyl-Tsi product, the formation of HTsi and the ultimate loss of the methyl groups from the tantalum species as evidenced by the loss of the Ta-methyl resonance at δ 1.49 ppm. The elimination of the methyl groups from the tantalum complex indicated that an intermediate organometallic species was formed along with the proposed Ta-Tsi or Ta-Phenyl species. A similar phenomenon was observed in 1978 by Shrock and Sharp<sup>51</sup> where they conducted a reaction between TaCp<sub>2</sub>Me<sub>3</sub> and Ph<sub>3</sub>C<sup>+</sup>BF<sub>4</sub><sup>-</sup>. The expected product, [TaCp<sub>2</sub>Me<sub>2</sub>(CH<sub>2</sub>)]<sup>+</sup>BF<sub>4</sub><sup>-</sup> was not isolated, but instead [TaCp<sub>2</sub>Me<sub>2</sub>]<sup>+</sup>BF<sub>4</sub><sup>-</sup> and Ph<sub>3</sub>CMe. The elimination of methane here, indicates that the deprotonation of one organic species during the course of the reaction and the subsequent formation of a reduced metallic species as evidenced by the separation of a dark brown precipitate upon filtration.

### 1.3.3. Zirconium Tetrachloride

To a THF solution ( $-78^{\circ}\text{C}$ ) of  $\text{ZrCl}_4$  (500 mg, 2.14 mmol) was added LiTsi (973 mg, 2.14 mmol). The solution was left to warm slowly to room temperature over 14 hours. The solvent was removed under pressure leaving a pale cream residue.  $^1\text{H}$  NMR spectrum and  $^{13}\text{C}$   $\{^1\text{H}\}$  NMR analysis of this residue showed a new resonance at  $\delta$  0.23 ppm and  $\delta$  3.1 ppm respectively. In addition, the presence of the protonated ligand HTsi was also observed. We assumed this new peak at  $\delta$  0.23 ppm to be  $\text{ZrTsiCl}_3$  or a derivative thereof. **Figure 15(a) and (b)** show the  $^1\text{H}$  NMR and  $^{13}\text{C}$   $\{^1\text{H}\}$  NMR respectively of this new organometallic species. Purification of this complex proved difficult, however recrystallisation attempts led to the isolation of LiCl indicating that metathesis of a Zr-Cl bond had occurred. In stoichiometric reactions of the Zr-Tsi complex with the agents methyl magnesium bromide, allyl magnesium bromide, methyl lithium, phenyl lithium,  $(^i\text{Bu}_2\text{PhO})\text{Li}$  and  $(^i\text{Pr}_2\text{PhO})\text{Li}$ , no shift of the  $^1\text{H}$  NMR resonance assigned to the Zr-Tsi moiety was observed. Even under extremely harsh conditions (elevated reaction temperatures for long periods of time) no definite shift, or formation of new resonances on the NMR time-scale were observed, consistent with the stability of the Tsi group on the Zr species. The  $\text{ZrTsiCl}_3$  material was found to be stable for long periods of time when stored under an inert atmosphere of nitrogen. The species was readily soluble in polar solvents, soluble in aromatic organic solvents and insoluble in short chain hydrocarbon solvents such as hexane and pentane.

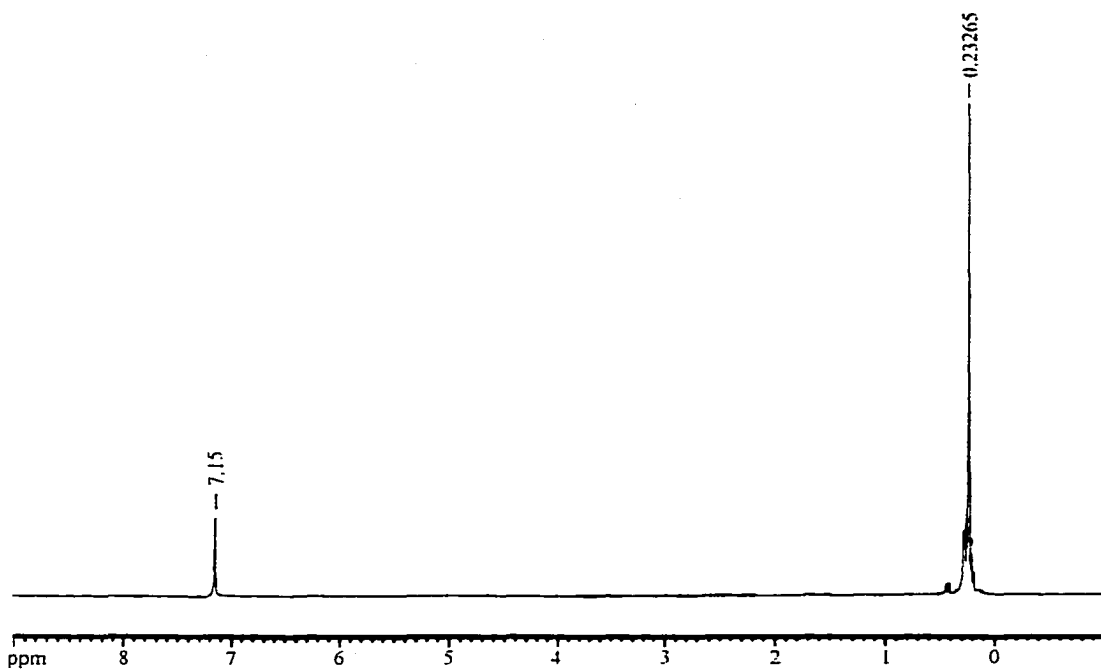


**Figure 15(a):**  $^1\text{H}$  NMR of the Zr-Tsi Cluster Complex in  $\text{C}_6\text{D}_6$

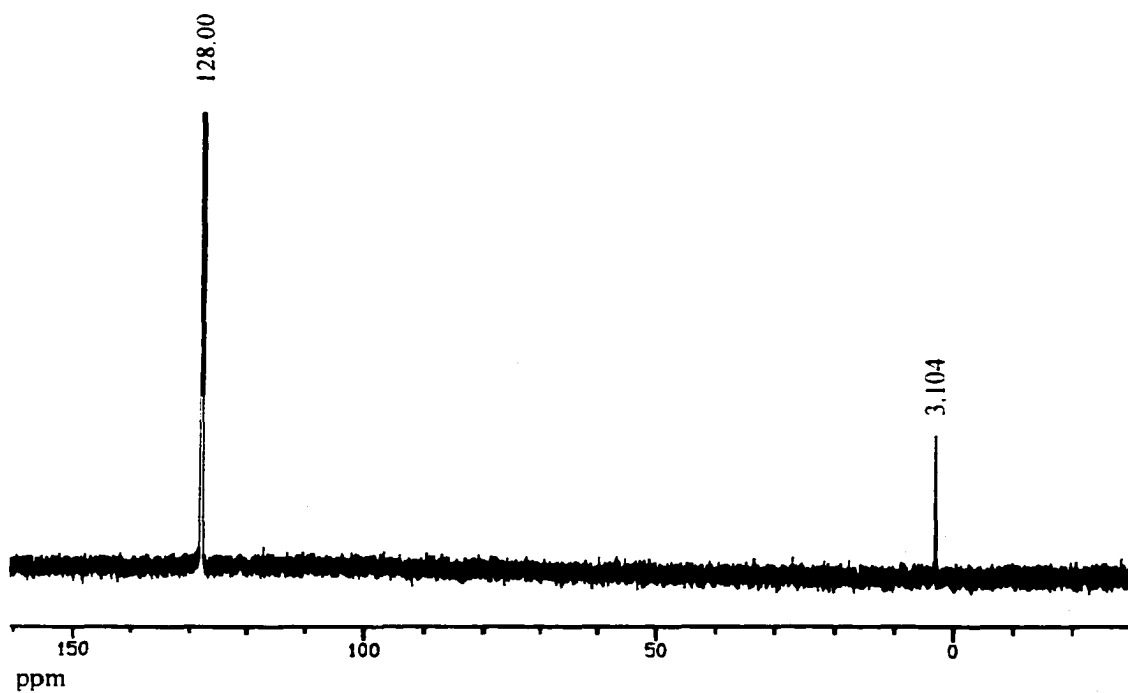


**Figure 15(b):**  $^{13}\text{C}$   $\{^1\text{H}\}$  NMR of the Zr-Tsi Cluster Complex in  $\text{C}_6\text{D}_6$

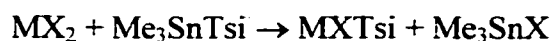
Attempts to synthesise  $\text{ZrTsi}_2\text{Cl}_2$  were unsuccessful and our findings indicated that only one substitution takes place around the Zr metal, since, even after prolonged reaction times no change was observed in the intensity of the  $^1\text{H}$  NMR resonance of LiTsi with respect to the  $\text{ZrCl}_3\text{Tsi}$  complex formed. The inability to synthesise a disubstituted Tsi product suggested that the Tsi ligand is too bulky to allow two such ligands to be bonded to the Zr atom.

The complexes  $\text{ZrCl}_3\text{X}$  or  $\text{ZrCl}_2\text{X}_2$  (where  $\text{X} = (\text{}^t\text{Bu}_2\text{PhO}), (\text{}^i\text{Pr}_2\text{PhO}), (\text{}^t\text{Bu}_2\text{PhN}), (\text{}^i\text{Pr}_2\text{PhN})$ ) were synthesised and were subsequently reacted with LiTsi. The presence of the R groups prior to the addition of the lithium salt should have aided in the stabilisation of the organometallic intermediate species isolated ( $\text{X-ZrCl}_2\text{Tsi}$ ). This is primarily due to the high stability of the early transition metal – oxygen or nitrogen bond (M-O, M-N). The reactions conducted between crystalline  $\text{ZrCl}_3\text{X}$  materials and LiTsi did not lead to the synthesis of a new organometallic species, but rather resulted in the formation of HTsi.

#### 1.3.4. $\text{Me}_3\text{SnTsi}$ and ${}^n\text{Bu}_3\text{SnTsi}$

Due to the repeated formation of the protonated ligand and benzyl-Tsi less basic ligands with lower reducing strengths were investigated in hope that this would suppress the formation of these side products. The choice of possible ligands were  $\text{TsiMgCl}$ ,  $\text{Tsi}_2\text{Mg}$ ,  $\text{TsiZnCl}$ ,  $\text{Tsi}_2\text{Zn}$ ,  $\text{Me}_3\text{SnTsi}$ ,  ${}^n\text{Bu}_3\text{SnTsi}$ ,<sup>27-30</sup> which have been previously synthesised and characterised by Eaborn and co-workers. From these reports it was learned that the Mg-Tsi and Zn-Tsi bonds are thermally stable and hence were not suitable for the present investigations.

From the reactions conducted between the Sn-Tsi reagents and transition metal complexes such as  $[\text{RhCl}(\text{CO})_2]_2$ ,  $\text{RuCl}_2(\text{C}_6\text{H}_6)\text{PPh}_3$ ,  $\text{IrCl}(\text{CO})(\text{PPh}_3)_2$ ,  $[\text{Ru}(\text{Cl})_2\text{C}_6\text{H}_6]_2$ ,  $\text{CoCl}_2$ ,  $\text{TaCl}_5$ ,  $\text{NbCl}_5$ , it was determined that the Sn reagents were extremely unreactive. There was no spectroscopic evidence to suggest the formation of a new organometallic-Tsi species, nor was there any evidence for the formation of the chlorides  $\text{Me}_3\text{SnCl}$  and  ${}^n\text{Bu}_3\text{SnCl}$ .



Where M is an organometallic species and X = a halogen.

For example, when  $\text{Me}_3\text{SnTsi}$  (0.253 mmol) was added to  $\text{TaCl}_5$  (0.253 mmol) or  $\text{NbCl}_5$  (0.253 mmol) in toluene, colour changes were observed from pale yellow (for  $\text{TaCl}_5$ ) or orange (for  $\text{NbCl}_5$ ) to a dark brown.  ${}^{13}\text{C}\{^1\text{H}\}$  and  ${}^1\text{H}$  NMR spectra for both reactions showed no change in the chemical shift of the tin reagent and hence no indication for the formation of a new organometallic species. No resonances attributed to HTsi or benzyl-Tsi were detected during the course of these reactions.

From these observations we conclude that the tin-Tsi reagents were too inert for the formation of the desired M-Tsi product. (M = Transition metal species from **Table 1**, Section 1.5)

## 1.4. Conclusion

Primarily all reactions conducted between LiTsi and the organometallic species documented led to the formation of HTsi. Studies have shown that HTsi was only formed in the presence of the organometallic precursors. The formation of HTsi did not occur when LiTsi was heated for long periods of time in solution in the absence of the organometallic complex.

From the reaction of  $\text{RuCl}_2(\text{C}_6\text{H}_6)\text{PPh}_3$  with LiTsi we believe that  $\text{RuClTsi}(\text{C}_6\text{H}_6)\text{PPh}_3$  may have been the kinetically favoured product formed. However, due to steric influences the Ru-Tsi bond possibly destabilised and for this reason the formation of the thermodynamically favoured 18-electron  $\text{RuCl}(\text{H})(\text{C}_6\text{H}_5\text{Tsi})\text{PPh}_3$  complex was observed. These results were confirmed via  $^1\text{H}$  NMR spectroscopic analysis.

For the reaction conducted between  $\text{ZrCl}_4$  and LiTsi, NMR analysis indicated the successful synthesis of Zr-Tsi, however, the isolation of the Zr-Tsi species proved difficult. Attempts to synthesise  $\text{ZrCl}_2\text{Tsi}_2$  were unsuccessful leading to the conclusion that the Tsi organic moiety is too bulky to allow two such ligands to be bonded to the Zr atom.

The reactions conducted between  $\text{TaCl}_5$  (or  $\text{NbCl}_5$ ) and LiTsi led to the isolation of benzyl-Tsi. The formation of this organic species is thought to occur via a 2-electron reductive elimination pathway between the solvent and/or Tsi alkyl groups and the organometallic precursor. This theory was further substantiated when the reaction between  $\text{TaBr}_5$  and LiTsi in toluene also led to the isolation of benzyl-Tsi.



In conclusion, LiTsi is a very reactive ligand. In the presence of an organometallic precursor this reagent readily attacked solvents prior to or after the decomposition of the intermediate formed M-Tsi species. We believe that due to the steric demands imposed on the metal atom face and the short M-C bond, this organometallic species is not stable and for this reason the reactions conducted resulted in side product formation. (M = Transition metal species)

Results obtained from the reactions conducted between HSiTsi or LiSiTsi ligands and Wilkinson's catalyst, Vaska's complex, the Rh analogue  $[\text{RhClCO}(\text{PPh}_3)_2]$  or  $\text{RuCl}_2(\text{C}_6\text{H}_6)\text{PPh}_3$  led to observed multiple TMS resonances in the  $^1\text{H}$  NMR spectrum. The formation of  $\text{Si}(\text{TMS})_4$  further confirmed the migration of TMS groups during the course of the reactions conducted. These results corroborated previous independent studies conducted by Wu, Li and Burchardt.<sup>45,46</sup>

Oxidative addition reactions of ITsi across four co-ordinate Ir(I) and Rh(I) complexes were attempted. From the reactions conducted it was concluded that the relative steric bulk surrounding the iodine atom of this ligand was found to be greater than originally anticipated and no spectroscopic evidence indicated the formation of a new I-M(III)-Tsi complex. The relative inertness of this ligand was further observed due to the inability to form Tsi-OTf, from a direct reaction of ITsi and AgOTf.

Reactions between  $\text{Me}_3\text{SnTsi}$  or  $^n\text{Bu}_3\text{SnTsi}$  and the organometallic complexes listed in **Table 1** (section 1.5) were investigated. From these studies the tin reagents appeared to be unreactive towards the organometallic species and hence too inert for the formation of the desired M-Tsi product.

## Future Work

One future ligand to consider for further applications for the synthesis of an electron deficient organometallic system could be: Bis[tris(trimethylsilyl)phenylsilane].<sup>52</sup>

**Figure 16.** This ligand undergoes direct metallation with MeLi to give the lithium salt Bis[tris(trimethylsilyl)phenylsilyl]lithium. This salt possesses no  $\alpha$  or  $\beta$  protons and hence  $\beta$  hydride elimination from the ligand to the metal will not occur.

Due to the phenyl substituent that lies planar between the adjacent TMS groups, the size of the ligand is smaller (when comparing cone angles) than the investigated tris(trimethylsilyl)methyl organic complex. For this reason the steric demands enforced on to the metal atom centre of the organometallic would be reduced and the thermal stability of the corresponding organometallic complexes may possibly be increased.

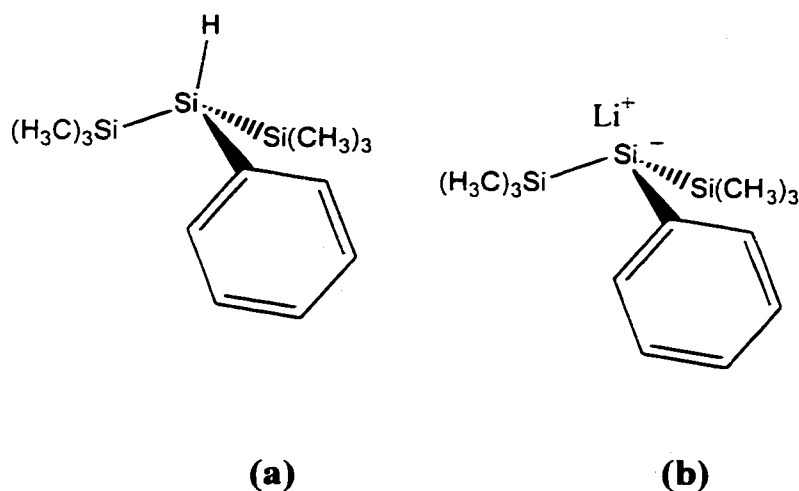


**Figure 16:** (a) Bis[tris(trimethylsilyl)phenylsilane] and (b) Bis[tris(trimethylsilyl)phenylsilyl]Lithium.

## 1.5. Experimental

### 1.5.1. General Methods

All the reactions were carried out under a dry and oxygen-free nitrogen atmosphere using Schlenk and Swivel frit techniques or by using an M-Braun Glove box (<2 ppm H<sub>2</sub>O, <1 ppm O<sub>2</sub>) at ambient temperature.

All solvents were pre-dried, degassed and maintained under vacuum or under an inert atmosphere of nitrogen prior to use. Ether, toluene, hexane pentane and THF were all distilled over sodium/benzophenone and kept under vacuum in sealed round bottom flasks. When required the solvents were vacuum transferred directly into the reaction vessels using Schlenk techniques. Deuterated benzene was degassed and dried over molten potassium, then vacuum transferred and stored over potassium mirror. Deuterated toluene and THF were dried over sodium/benzophenone and distilled under vacuum. n-Butyllithium and methyllithium were obtained from sure seal ALDRICH bottles and stored within the glove box. All potentially toxic products were destroyed in the appropriate manner. Chemical materials used for the reaction procedures were anaerobically weighed in an inert atmosphere of N<sub>2</sub> using the M-Braun Glove box unless otherwise stated.

*Physical and Analytical Measurements.* - Solution <sup>1</sup>H NMR and <sup>13</sup>C {<sup>1</sup>H} NMR spectra were recorded at 300 or 500 MHz with a Bruker Advance Spectrospin dpx 300/500 instrument. All the chemical shift values were recorded in ppm using d<sup>6</sup>-benzene, d<sup>8</sup>-THF as internal standards. The Mass Spectra were recorded on a Kraots MS80RF instrument. The X-ray data was collected on a SIEMENS SHELXTL - Ver.

5.03

The organometallic precursors investigated during the course of our studies are given in

**Table 1.**

<b>Element</b>	<b>Organometallic Species</b>
<b>Ti</b>	TiCl <sub>4</sub> , TiCl <sub>2</sub> (Cp) <sub>2</sub>
<b>Zr</b>	[ZrCl <sub>2</sub> Cp <sub>2</sub> ], [ZrCl <sub>3</sub> Cp*], ZrCl <sub>4</sub> , [ZrCl <sub>3</sub> ( <sup>i</sup> Pr <sub>2</sub> PhO)], [ZrCl <sub>3</sub> ( <sup>t</sup> Bu <sub>2</sub> PhO)], [ZrCl <sub>3</sub> ( <sup>i</sup> Pr <sub>2</sub> PhN)], [ZrCl <sub>3</sub> ( <sup>t</sup> Bu <sub>2</sub> PhN)]
<b>Nb</b>	NbCl <sub>5</sub>
<b>Ta</b>	TaCl <sub>5</sub> , Ta Me <sub>3</sub> Cl <sub>2</sub> , TaBr <sub>5</sub>
<b>Mn</b>	MnCl <sub>2</sub>
<b>Fe</b>	FeCl <sub>2</sub>
<b>Ru</b>	[Ru(C <sub>6</sub> H <sub>6</sub> )Cl <sub>2</sub> (PPh <sub>3</sub> )], [RuCl <sub>2</sub> (C <sub>6</sub> H <sub>6</sub> ) <sub>2</sub> ]*, [RuCl <sub>3</sub> (C <sub>6</sub> H <sub>6</sub> )]PF <sub>6</sub>
<b>Co</b>	CoCl <sub>2</sub>
<b>Rh</b>	RhI <sub>3</sub> , RhCl(P(Ph <sub>3</sub> )) <sub>3</sub> , [Rh(COD)Cl] <sub>2</sub> , [Rh(COE) <sub>2</sub> Cl] <sub>2</sub> , [RhCOD]SO <sub>3</sub> CF <sub>3</sub> , RhClCO(PPh <sub>3</sub> ) <sub>2</sub> *
<b>Ir</b>	IrI <sub>3</sub> , [Ir(COE) <sub>2</sub> Cl] <sub>2</sub> , [Ir(COD)Cl] <sub>2</sub> , IrClCO(PPh <sub>3</sub> ) <sub>2</sub> *

\* These materials, Ir(I), Rh(I) and Ru(II) species can also be used in oxidative addition reactions of the ligand across the four co-ordinate organometallic moiety by I-Tsi.

**Table 1:** Organometallic Species Investigated

### 1.5.2. Reaction of $\text{RuCl}_2\text{C}_6\text{H}_6(\text{PPh}_3) + \text{LiTsi}$

$\text{RuCl}_2\text{C}_6\text{H}_6\text{PPh}_3$  was prepared according to literature.<sup>53</sup> To a solution of  $\text{RuCl}_2\text{C}_6\text{H}_6\text{PPh}_3$  (250 mg, 0.489 mmol) in benzene was added LiTsi (222 mg, 0.489 mmol). The solution was left to stir under an inert atmosphere of nitrogen at room temperature for 30 minutes, during which time a colour change was observed from dark orange to deep red brown. Solvent removal under reduced pressure resulted in the isolation of a deep red brown solid. Crystallisation attempts were made from concentrated solutions from the following solvent(s): Hexane, Pentane, Ether, THF, Benzene, Toluene and Dichloromethane. All attempts were unsuccessful. This material is not air sensitive.  $^1\text{H}$  NMR ( $\text{C}_6\text{D}_6$ ): (1H,d)  $\delta$  -6.17 ppm, (27H, s)  $\delta$  0.36 ppm, (1H, dd)  $\delta$  3.25-3.29 ppm, (1H, d)  $\delta$  4.06-4.07 ppm, (1H, d)  $\delta$  5.49-5.51, (2H, ddd)  $\delta$  5.54-5.65 ppm, (6H, m)  $\delta$  7.8-7.9 ppm, (6H,m)  $\delta$  6.95-7.1 ppm, (3H, m) 6.87-6.9 ppm;  $^{13}\text{C}$  { $^1\text{H}$ } NMR ( $\text{C}_6\text{D}_6$ ):  $\delta$  3.8, 129.6, 134.3 ppm.

### 1.5.3. Reaction of $\text{LiSiTsi}$ and $\text{RhCl}(\text{PPh}_3)_3$

To a solution of  $\text{RhCl}(\text{PPh}_3)_3$  (225 mg, 0.243 mmol) in benzene was added LiTsi (110 mg, 0.243 mmol). The solution was left to stir under an inert atmosphere of nitrogen at room temperature for 72 hours, during which time a colour change was observed from red to deep red brown. Solvent removal under reduced pressure resulted in the isolation of a dark brown oil. NMR analysis of this residue gave the following resonances:  $^1\text{H}$  NMR ( $\text{C}_6\text{D}_6$ ): (27H, s)  $\delta$  0.19 ppm, (45H, m)  $\delta$  6.75-7.65;  $^{13}\text{C}$  { $^1\text{H}$ } NMR ( $\text{C}_6\text{D}_6$ ):  $\delta$  0.5 ppm,  $\delta$  131.5 ppm,  $\delta$  132.4 ppm,  $\delta$  132.5 ppm;  $^{31}\text{P}$  NMR ( $\text{C}_6\text{D}_6$ ):  $\delta$  25.2 ppm.

Crystallisation attempts from concentrated solutions of hexane, pentane, THF, diethyl-ether, toluene at  $-37^{\circ}\text{C}$  were unsuccessful. Cubic orange crystals were obtained from a THF/hexane mix at  $-37^{\circ}\text{C}$ , however NMR analysis of these crystals in  $\text{C}_6\text{D}_6$  showed no presence of Tsi or Phenyl groups.

#### 1.5.4. Synthesis of Benzyl-Tsi (A)

To a stirred solution of  $\text{TaCl}_5$  (404 mg, 1.13 mmol) in 10 ml toluene was added LiTsi (513 mg, 1.13 mmol, 1 equivalent) resulting in an immediate colour change from yellow to dark brown. The solution was left to stir at room temperature for 20 minutes. The solvent was removed at reduced pressure yielding a thick dark viscous residue. This was re-dissolved in hexane (20 ml) and filtered. The filtrate was reduced in volume under vacuum, resulting in a pale yellow oil, which was re-dissolved in the minimum volume of hexane. The saturated solution was left at  $-37^{\circ}\text{C}$  overnight. After this time clear transparent crystals had formed (213 mg, 58% yield) that were suitable for X-ray crystallographic analysis.  $^1\text{H}$  NMR ( $\text{C}_6\text{D}_6$ ):  $\delta$  0.14 ppm (27H, s),  $\delta$  3.10 ppm (2H, s),  $\delta$  7.06 ppm (3H, m),  $\delta$  7.2-7.3 ppm (2H, d, b);  $^{13}\text{C}$   $\{^1\text{H}\}$  NMR ( $\text{C}_6\text{D}_6$ ):  $\delta$  3.6 ppm,  $\delta$  36.2 ppm,  $\delta$  127.7-128.3 ppm.

### 1.5.5. Synthesis of Benzyl-Tsi (B)

To a stirred solution of  $\text{NbCl}_5$  (500 mg, 1.85 mmol) in 10 ml toluene was added LiTsi (841 mg 1.85 mmol, 1 equivalent) resulting in an immediate colour change from orange to dark brown. The solution was left to stir at room temperature for 20 minutes. The solvent was removed at reduced pressure to obtain a thick dark viscous residue. This was re-dissolved in hexane (25 ml) and filtered. The filtrate was reduced in volume under vacuum, resulting in a pale yellow oil, which was re-dissolved in the minimum volume of hexane. The saturated solution was left at  $-37^\circ\text{C}$  overnight. After this time clear transparent crystals had formed (395 mg, 65% yield) that were suitable for X-ray crystallographic analysis.

### 1.5.6. Reaction of $\text{Me}_3\text{TaCl}_2 + \text{LiTsi}$

To a cooled ( $-20^\circ\text{C}$ ) stirred solution of  $\text{Me}_3\text{TaCl}_2$  (31 mg, 0.1099 mmol) in 5 ml toluene was added LiTsi (50 mg, 0.1099 mmol, 1 equivalent) resulting in an immediate colour change from yellow to dark brown. The solution was left to stir at  $-20^\circ\text{C}$  for 10 minutes, during which time gas evolution was observed. The solvent was removed at reduced pressure to obtain a thick dark viscous residue. This was re-dissolved in pre cooled ( $-37^\circ\text{C}$ ) hexane (10 ml) and filtered. The filtrate was reduced in volume under vacuum, resulting in a pale yellow coloured oil. NMR analysis of this crude material gave the following resonances:  $^1\text{H}$  NMR ( $\text{C}_6\text{D}_6$ ):  $\delta -0.85$  ppm (1H, s),  $\delta 0.13$  ppm (27H, s),  $\delta 0.14$  ppm (27H, s),  $\delta 3.11$  ppm (2H, s),  $\delta 6.9-7.26$  ppm (5H, m);  $^{13}\text{C}$   $\{^1\text{H}\}$  NMR ( $\text{C}_6\text{D}_6$ ):  $\delta 3.6$  ppm,  $\delta 36.2$  ppm,  $\delta 127.7-128.3$  ppm.

### 1.5.7. Reaction of $\text{ZrCl}_4 + \text{LiTsi}$

Using swivel frit and Schlenk line techniques  $\text{ZrCl}_4$  (250 mg, 1.07 mmol) and  $\text{LiTsi}$  (488 mg, 1.07 mmol) were mixed together in the solid state under an inert atmosphere of nitrogen. The apparatus was cooled under vacuum to  $-78^\circ\text{C}$  and dried degassed THF was vacuum transferred into the reaction vessel. The agitating mixture was left to warm to room temperature over 16 hours. A colour change was observed from pale yellow to dark yellow. The solution volume was reduced under vacuum giving a yellow oily residue. This residue was washed several times with hexane and the filtrate collected. The filtrate volume, transparent yellow in colour, was reduced and the residue re-dissolved in  $\text{C}_6\text{D}_6$  for NMR analysis. Recrystallisation attempts of this material (196.7 mg) from saturated solutions of hexane at low temperature ( $-37^\circ\text{C}$ ) resulted in the formation of clear cubic crystals of  $\text{LiCl}$  (14 mg, 7.32% yield). Attempts to isolate and hence purify any new zirconium species were unsuccessful.  $^1\text{H}$  NMR ( $\text{C}_6\text{D}_6$ ):  $\delta$  0.23 ppm (27H, s);  $^{13}\text{C}$  { $^1\text{H}$ }; NMR  $\delta$  3.1 ppm.



## Chapter 2

### Investigations into Mesoporous Niobium Oxide – Cobaltocene Composites: the First Example of Superparamagnetism in Molecule-Based Clusters.

#### 2.1. Introduction

In 1992 Mobil discovered M41S,<sup>54,55</sup> a new family of hexagonally packed mesoporous<sup>56</sup> (alumino) silicate molecular sieves with a pore size regime of 15-100 Å and pore volumes exceeding 1000 m<sup>2</sup>g<sup>-1</sup>. These materials were the first molecular sieves with pore sizes greater than zeolites (<15Å). Microporous zeolites are used in industry as molecular sieves for separating molecules of different sizes. Due to their restricted pore sizes, reactions are limited to small molecules and substrates. For this reason, the isolation of larger pore sized mesoporous materials, such as MCM-41 (a member of the M41S family), was a great breakthrough. The high surface areas of these materials could potentially result in higher catalytic activity as compared to the microporous zeolites and the increased pore sizes would allow for the fixation of large active complexes within the mesophases. As a result, M41S materials have highly desirable properties making them ideal candidates for catalytic applications where increased surface areas and larger pore sizes are required for high catalytic activity.

The discovery of mesoporous materials has inspired research in areas that include sorption and phase transitions in confined spaces,<sup>57</sup> ion exchange,<sup>58,59</sup> the formation of intrachannel metal, metal oxide, and semiconductor clusters,<sup>60</sup> and the inclusion of various metal complexes and other guest species within the mesostructure.<sup>61</sup> These

investigations have been made possible due to the individual properties, both chemical and physical, that mesoporous materials exhibit.

### 2.1.1. MCM-41 and M41S Physical Properties and Synthesis

M41S materials are synthesised either via the self-assembly of molecular aggregates or via supramolecular assemblies.<sup>62</sup> The formation of the inorganic mesostructure relies predominantly on the self-assembly of the organic surfactants in solution. Surfactants consist of a hydrophilic head group and hydrophobic long tail group. In the presence of water the self organisation of the organic groups results in micelle structures, thus the contact between the incompatible ends of the organic moieties is minimised. It is the formation of the spherical components that gives the characteristic framework of the inorganic oxide. The most common method for the synthesis of these mesoporous materials is via Liquid Crystal Templating (LCT).<sup>55</sup>

Liquid Crystal Templating is an electrostatic interaction between the anionic inorganic precursor ( $I^-$ ) and the cationic organic surfactant ( $S^+$ ). For example, with regards to MCM-41, the silicate material ( $I^-$ ) forms inorganic walls between the ordered organic surfactant micelles ( $S^+$ ) giving an  $I^-S^+$  system. Huo *et al.* first reported this interaction in 1994.<sup>63,64</sup> Generally, the synthesis of these materials occurs under basic reaction conditions ( $pH > 7$ ). Under extreme acidic conditions (i.e.  $pH \approx 2$ ) the inorganic silicate species  $I$  is cationic and for this reason a counteranion ( $X^-$ ) is required for the synthesis to lead to the formation of the mesostructure giving an  $S^+X^-I^+$  system. Consequently, there are two routes, basic and acidic, used to make molecular sieves of various mesophases.

Other preparative methods for the formation of the silica based mesoporous materials have been proposed. Tanev and Pinnavaia<sup>65</sup> demonstrated that mesoporous silica can be prepared via the specific hydrogen bonding interactions of an alkylamine ( $S^0$ ) head group and a hydroxylated silica source such as tetraethylorthosilicate ( $I^0$ ). In this instance, the materials are "locked by the long-range ordering of the pores."<sup>65</sup> Hence, "a higher degree of interparticle mesoporosity is achieved."<sup>65</sup> This route leads to the isolation of mesoporous silicates with thicker walls and a higher thermal stability than those prepared via LCT.

The mesoporous structure is extremely dependent on the specific surfactant chain length. The longer the hydrophobic chain length, the greater the residual pore size of the hexagonally packed cylindrical mesopores, and vice versa. The pore size can also be controlled via the intercalation of layered silicates with the surfactant species as evidenced recently by Kresge and co-workers.<sup>54</sup> Furthermore, organic species (such as 1,3,5-trimethylbenzene) may be placed inside the hydrophobic regions of the micelles. This leads to an increase in the overall micelle diameter. The mesostructure is also dependent on the specific concentration of the surfactant used. For example, to achieve the hexagonal array, a surfactant:inorganic precursor (S:I) ratio of  $1:<1$  is required. Variation of these ratios leads to the isolation of cubic (S:I) 1:1-1.5, or lamellar (S:I) 1:1.2-2 mesostructured composites.

## 2.1.2. Non (Alumino) Silicate Bases Mesoporous Materials

In 1994, Huo and co-workers investigated non-silicate based composites.<sup>64</sup> Their research led to the isolation of novel mesostructured oxides in which the metal precursor used included: Sb, Fe, Zn, Pb, W and Mo.<sup>63,64,66</sup> Unfortunately, many of the isolated mesophases were layered and did not yield porous materials upon removal of the surfactants. For reactions where hexagonally-packed mesostructured materials were successfully synthesised, the structure later collapsed following solvent removal and calcination. This observation was remarked upon as being “due to the lack of the complete condensation of the inorganic framework.”<sup>64,65</sup>

In 1995, Antonelli and Ying<sup>67</sup> successfully synthesised the first inorganic, non silicate mesostructured materials from titanium isopropoxide (I) and phosphate surfactants (S) via a modified sol-gel process. \* This mesoporous species, designated Ti-TMS (Tech. Molecular Sieve), was the first example of a structurally stable hexagonally packed mesoporous transition metal oxide molecular sieve. Ti-TMS was synthesised with a narrow pore size distribution and high surface area in the regime of  $200 \text{ m}^2\text{g}^{-1}$ .

Further advances by Antonelli and Ying led to the isolation of the first Nb oxide and Ta oxide based mesostructures. Both were obtained without the addition of chelating agents.<sup>68,69,70</sup> As with the Ti-TMSI materials, the organic surfactants were pre-treated with the metal alkoxides in the absence of the solvent (water) to form the metal-ligand surfactants. Amine surfactants were chosen due to the strong M-N (M = Nb or Ta) bond formed. The addition of water to the reaction mixture led to the surfactant self assembly

and the formation of the metal alkoxide species. This process is also recognised as Ligand Assisted Templating (LAT) and enables the researchers to control the pore size distribution of the mesoporous transition metal oxides, analogous to the M41S family of aluminosilicates. Attempts to synthesise these materials via conventional LCT led to the isolation of mesostructured products, where the uncondensed transition metal salts were unstable upon surfactant removal.

As with (alumino) silicate materials, the mesostructure of these transition metal mesoporous composites was dependent on the specific S:I ratio used. A variation in the S:I ratio led to the isolation of mesophases with different mesostructures as illustrated in **Table 2**.

<b>Material</b>	<b>Mesostructure</b>	<b>S:I Ratio</b>
<b>Nb-TMS1</b>	<b>Hexagonal</b>	<b>&lt;1.25</b>
<b>Nb-TMS2</b>	<b>Hexagonal</b>	<b>1.5</b>
<b>Nb-TMS3</b>	<b>Cubic</b>	<b>1</b>
<b>Nb-TMS4</b>	<b>Lamellar</b>	<b>2</b>

**Table 2:** A Variation in the S:I Ratio Leads to the Isolation of Mesoporous Materials with Differing Mesostructures.<sup>57,69</sup>

Antonelli, Wong and Ying<sup>71</sup> reported the successful isolation of the first Zr-TMS mesoporous composite with surface areas of  $560 \text{ m}^2\text{g}^{-1}$  in 1997. In the same manner as the Ti-TMS composite, the surface areas, pore sizes and pore volumes of the Zr-TMS

---

\*Addition of 1 mol equivalent of acetylacetonone (chelating agent) to the titanium isopropoxide prior to hydrolysis slowed the rate of condensation of the titanium alkoxide precursor, thus resulting in a better interaction between the metal and the organic surfactant.

species could be accurately controlled by altering the chain lengths of the templating alkylphosphate molecules. Unfortunately, isolation of a well-defined mesoporous phase for the Zr species proved difficult. Recent developments by Antonelli,<sup>72</sup> however, have led to the synthesis of mesoporous Zr-TMS with higher surface areas than those previously documented.<sup>71</sup> The preparation of this material was achieved via LAT with carboxylate surfactants in place of the previously used phosphate surfactants. Furthermore, these carboxylate surfactants were removed via acid treatment and not via conventional methods such as calcination.

The successful synthesis of these well-ordered transition metal-oxide based mesoporous materials was a great achievement. Unlike the traditional silicate-based inorganic mesoporous materials, transition metals are capable of existing in various oxidation states. As a result, the oxides of the transition metals can be finely tuned for use in electromagnets and catalytic applications. One such example was first documented in 1997 by Tian *et al.*<sup>73</sup> Their investigations led to the synthesis of a stable well ordered Mn oxide mesoporous material (designated MOMS-1). This transition metal mesoporous composite possessed semiconducting properties that were brought about by the Mn mixed oxidation state ( $\text{Mn}^{3+}$  and  $\text{Mn}^{4+}$ ) system within the lattice of the composite. The conductivity values reported for the semiconducting material ranged from  $5.0 \times 10^{-8} \text{ (ohm cm)}^{-1}$  before surfactant removal to  $8.1 \times 10^{-6} \text{ (ohm cm)}^{-1}$  after calcination was complete, thus showing temperature dependent semiconducting properties.

### 2.1.3. Catalytic Properties

Initial catalytic applications focused on the incorporation of guest species into the MCM-41 framework.<sup>74,75</sup> For example, either the heteroatom guest species was deposited on to the surface of the mesoporous framework or the functional groups were covalently anchored to the mesoporous channel walls.<sup>76</sup> Intrachannel reactions, such as the polymerisation of preadsorbed monomers, have also been achieved.<sup>77</sup>

More recently, scientists have investigated the fixation of catalytically active complexes on to the walls of the MCM-41 porous framework, hence combining homogeneous catalysis with a heterogeneous catalyst support.<sup>78,80</sup> One example involves the addition of an inorganic metal species to the reaction mixture prior to the formation of the pure mesoporous material. Cheng and Zhou<sup>79</sup> have recently shown that Gallium (Ga) can potentially be added to the synthesis mixture and incorporated into MCM-41 after the precipitation of the pure mesostructured silicate. To date, doped MCM-41 materials have been used for catalytic applications. Unfortunately, doping levels have proven to be low and are at best 1-2 mol %, with the exception of Zr,<sup>80</sup> whereby doping levels reached as high as 17 mol %.

### 2.1.4. Intercalation of Organometallic Species into the Mesoporous Framework

The manipulation of mesoporous materials by intercalation of organometallic species within the host lattice framework could potentially lead to new composites possessing conducting, semiconducting or even superconducting properties.<sup>81</sup> Furthermore, the ability to finely tune the reduction of the metallic species within the

walls of the composites could potentially lead to the isolation of novel mesoporous materials with varying chemical and physical properties. Ozin and co-workers previously addressed this phenomenon, whereby they successfully synthesised an iron based ceramic species with "tuneable magnetic properties."<sup>82</sup> In this instance, magnetic measurements on the ceramic indicated superparamagnetic behaviour with a blocking temperature ( $T_b$ ) of 30K.

For the purpose of our investigations we chose to explore the intercalation of highly reducing species into the framework of the mesoporous transition metal oxides previously synthesised by Antonelli and Ying.<sup>67-70</sup> It was hoped that electron transfer reactions between the host and the guest would occur leading to novel materials with a reduced mesostructure. Not only would these be the first reduced mesoporous oxides, but also the presence of free electrons in the mesostructure could potentially lead to composites with novel electronic and magnetic properties.

To date, the transition metal oxides that have been successfully synthesised with crystalline mesostructures include Ti<sup>67</sup>, Zn,<sup>83</sup> Nb<sup>68,69</sup> and Ta.<sup>70</sup> Presently, the majority of these mesoporous materials are insulators with the metal atoms in their highest oxidation states. One such example is Nb<sub>2</sub>O<sub>5</sub> (Nb +5), which is an insulator, whereas NbO (Nb +2) displays metallic properties. Nevertheless, the ability to finely tune these oxidation states would result in materials with potentially more interesting properties and perhaps even the first mesoporous oxides with metallic properties. For this reason, the composites would be capable of acting as hosts for a broad range of inorganic and organic guest species. Researchers<sup>84</sup> have shown that conducting polymers can be intercalated inside the channels of the hexagonal mesoporous silica host MCM-41. While these materials



possess very interesting magnetic and electrical properties, the silicate composites do not possess the variable oxidation states of analogous mesoporous materials synthesised from transition metal oxides.

Recent studies within Antonelli's group,<sup>85</sup> have led to the isolation of the first example of a reduced molecular sieve (Nb-TMS1), attained via the intercalation of alkali metals into the lattice of the mesoporous composite. These novel materials have tuneable electronic properties dependent on the specific loading level of the alkali metal species (Li, Na, K, Cs, and Rb). These investigations demonstrated that mesoporous transition metal oxides differ substantially from M41S materials in that they can simultaneously act as host lattices and electron acceptors. For this reason, a new area in mesoporous materials chemistry has been unveiled, leading to possible reactions that couple the intercalation of guest species and electron transfer mechanisms within the mesoporous host. Subsequent investigations within our group demonstrated that the intercalation of bisbenzene chromium into the niobium oxide mesoporous framework led to the isolation of a novel material with one-dimensional mixed oxidation state organometallic wires in the pore structure.<sup>86</sup> Ye, Trudeau and Antonelli<sup>87</sup> also showed that the intercalation of alkali metal fullerides into the mesoporous niobium-oxide host composite led to the formation of a material with conducting fulleride wires present within the mesostructure. This study provided the first experimental evidence that the  $n = 3$  state of  $K_3C_{60}$  is actually a Mott-Hubbard insulator, as suggested by calculation.

For the purpose of our studies we chose to investigate cobaltocene as the intercalating organometallic species. Cobalt has long been known for influencing the magnetic properties of mixed alloy systems, often showing strong ferromagnetic,<sup>88,89,90,91</sup>

superconducting<sup>81</sup> and in some cases superparamagnetic<sup>92,93,94,95</sup> properties. Consequently from our investigations, we expect the mesoporous composite to possess unusual magnetic properties. Previous studies have illustrated the successful intercalation of cobaltocene into layered systems such as sulphide and selenide<sup>96</sup> materials. Thus, we anticipate that since cobaltocene is highly reducing it should similarly react with mesoporous niobium oxide.

### 2.1.5. Cobaltocene (Co<sup>2+</sup>)

Cobalt metal is ferromagnetic and can exist in as many as 6 different oxidation states.<sup>97</sup> An even number oxidation state leaves the Co compounds paramagnetic, whereas an odd numbered oxidation state leaves the Co compounds diamagnetic. The first documented synthesis of CoCp<sub>2</sub>, in the mid 1950's, was achieved via the reaction of NaCp with [Co(NCS)<sub>2</sub>(NH<sub>3</sub>)<sub>4</sub>] in liquid ammonia. Characterisation of cobaltocene was found to be troublesome via conventional NMR methods because the <sup>1</sup>H NMR spectra showed a very broad signal due to the presence of the 1 unpaired electron.

Cobaltocene is a purple black pyrophoric paramagnetic crystalline solid (mp. 173°C) with an electron configuration of [Ar]3d<sup>7</sup>. X-ray molecular structures have determined that CoCp<sub>2</sub> is isostructural to FeCp<sub>2</sub> and that the two cyclopentadienyl (Cp) rings are planar, parallel and staggered with an average Co-C bond distance of 2.096Å (210 pm).

Synthesis of cobaltocinium, Co(III), a diamagnetic 18 electron system, is achieved by mild oxidation of CoCp<sub>2</sub> by FeCl<sub>3</sub> or O<sub>2</sub> and aqueous acid. Cobaltocene is highly electron rich. Hence, it is ideal for the reduction of the Nb +5 state to Nb +4 state

in the mesostructure. Investigations into the reactivity for both cobaltocene and cobaltocinium have shown that while  $\text{CoCp}_2$  is too reactive to undergo ring substitution reactions and  $\text{CoCp}_2^+$  is too inert, there is no tendency for either organometallic species to form dimers in solution. For these reasons, we believe that cobaltocene will be an ideal candidate for the reduction of the Nb metal within the mesoporous framework.<sup>98</sup> Furthermore, studies conducted by O'Hare<sup>81</sup> and co-workers in 1999, have emphasised how the magnetic properties of  $\beta$ -ZrN can be altered after the intercalation of cobaltocene between the layers of the organometallic species. The observations made, showed that the isolated products possessed superconducting properties, with a Curie temperature ( $T_c$ ) equal to 14 K. Thus, cobaltocene intercalates of mesoporous Nb oxide may also be superconducting, although superconducting behaviour in this particular study was limited to the structure of the Zr-N lamellar.

### 2.1.6. Characterisation of the Isolated Products

For the purposes of our investigations, analysis of the intercalated mesoporous transition metal species will be achieved via the following techniques.

#### i. X-ray Photoelectron Spectroscopy (XPS)

XPS is a very powerful tool for the study of molecular bonding.<sup>99</sup> Binding Energies (B.E.) are characteristic of the atoms being identified for each species and slight changes in the registered B.E. for any given element is dependent on the nature of the chemical environment of the sample. These changes in the core level B.E., or chemical shifts, are due to alterations in the electron density of the valence shell. The more highly oxidized the species is, the higher the B.E. For example, an increase in B.E. is observed

for a transition of Co (II) to Co (III), while a decrease in B.E. is observed for Nb (V) to Nb (IV).

XPS studies have shown that cyclopentadienyl complexes of the same metal (Co) in the neutral and cationic state follow the above trend.<sup>100</sup> For example, the B.E. for the Co metal 2p<sub>3/2</sub> resonance increases with increasing oxidation state. The results given for these specific studies (XPS data are referenced to C (C,H) 1s region at 285.0 eV) are listed in **Table 3**.

<b>Organometallic Species</b>	<b>Oxidation State</b>	<b># Unpaired electrons</b>	<b>M 2p<sub>3/2</sub></b>
(C <sub>5</sub> H <sub>5</sub> )Co(C <sub>5</sub> H <sub>6</sub> )	(I)	0	779.7 (2)
(C <sub>5</sub> H <sub>5</sub> ) <sub>2</sub> Co	(II)	1	780.2 (1)
[(C <sub>5</sub> H <sub>5</sub> ) <sub>2</sub> Co]PF <sub>6</sub>	(III)	0	781.7 (2)

**Table 3:** XPS Reference Data for Co 2p 3/2 Region of Co(II) and Co(III) Species.<sup>100</sup>

## ii. **Electron Paramagnetic Resonance (EPR)**

Electron Paramagnetic Resonance (EPR) is used as a tool to better understand the covalency and ground state structure of materials. The analysis detects changes in electron spin configuration and is dependent on the presence of permanent magnetic dipoles within the system. In fact, it is the reversal spin in an applied magnetic field of these paramagnetic systems that is recorded. The g value of a particular species is dependent on the particular paramagnetic ion, its oxidation state and co-ordination number and is responsible for the position of a registered absorption peak. For this reason, EPR spectra of solid materials often result in the acquisition of very broad peaks and consequently conditions must be met in order to obtain refined peaks from which

useful information may be gathered. One such method is to have a low concentration of unpaired electrons dissolved in a diamagnetic host structure. A second method is to conduct the analysis at liquid He temperatures (4.2 K) which often helps when line broadening peaks are due to the material possessing short relaxation times and hence broad resonances at room temperature. Unfortunately, in the case of cobaltocene, this problem cannot always be addressed in this manner since  $\text{CoCp}_2$  has very slow relaxation times. Even when EPR analysis is conducted at 4.2 K the characteristic hyperfine splitting (8 resonances detected for Co nuclear spin  $I = 7/2$ ) is generally very difficult to observe. For this reason, EPR measurements conducted on cobaltocene have not been conducted in the powdered or the single crystal state. Instead scientists<sup>101</sup> have investigated mixtures of  $\text{CoCp}_2$  in diamagnetic 'hosts' of  $\text{FeCp}_2$ . In all cases, the percentage of  $\text{CoCp}_2$  within the materials investigated did not exceed 5-7%. The results from these investigations showed that in order to observe a well resolved Co hyperfine structure the analysis had to be conducted along the z axis of the  $\text{CoCp}_2$ /organometallic system. The x and y axis spectra gave a broad line with no hyperfine splitting evidenced for the transition metal species. Hence, in light of these results, the researchers deduced that the spin-lattice relaxation time is angular dependant. For these experiments the g factors obtained were 1.67 and 1.74 for a  $\text{CoCp}_2/\text{FeCp}_2$  mixed system. These results correlate to those previously calculated in 1960 by R. Robertson and H. McConnell.<sup>102</sup>

EPR analysis can also be used to observe the presence of free electrons in the walls of the composite. By analysing temperature dependent spectra, one can gauge the density of states at the Fermi level and hence, the degree of metallic behaviour throughout the system.

### iii. **Ultraviolet Reflectance spectroscopy (UV)**

The information attained from these spectra gives one an insight into the transitions of the electrons between the outermost energy levels of the material being investigated. UV and Visible spectroscopy has a variety of applications associated with the local structure of materials because the positions of the absorption bands are sensitive to co-ordination environment and bond character. For the purposes of the present investigations, the recorded UV spectra was expected to possess:

- A broad peak at ca. 260 nm, due to the Nb-O sp valence to conduction band, as evidenced from UV spectra for the mesoporous Nb starting materials. Similarly, with respect to the Ti and Ta-oxide based materials their respective M-O sp valence to conduction bands register at ca. 250 nm.
- A broad peak at 400-420 nm consistent with the referenced cobaltocinium<sup>103</sup>  $\pi-\pi^*$  transition
- A broad peak ca. 580 nm attributed to the free electron in the walls of the mesoporous composite, relevant to the Nb4d- $\pi^*$  impurity band-to-conduction band transition.<sup>85</sup>

### iv. **X-ray Powder diffraction (XRD)**

XRD studies are very important and useful in qualitative phase analysis due to the fact that every crystalline material possesses its own characteristic powder diffraction pattern. In fact, the powder pattern has two characteristic features, the d-spacing of the lines and their intensities. XRD conducted on the products formed will give an indication as to whether the pore structure for the mesoporous material has been retained or destroyed. Retention of the pore structure is evidenced by the presence of a peak that

will be unchanged, un-shifted and superimposable on that of the starting material. Line broadening for one spectrum to the next is indicative of a transition from a well-ordered material mesostructure to a less ordered amorphous mesostructure.

**v. Nitrogen Adsorption Studies**

This analysis enables the researcher to determine the Brunauer, Emmette, Teller. (BET) surface area of the material. the Horvath Kawazoe (HK) cumulative pore volume of the product and the HK pore size of the material after the intercalation of the organometallic into the system. For our studies, we expect to see a drop in both the BET surface area and the pore volume for the product when comparisons are made to the mesoporous starting materials. This observation will only arise if no degradation of the organometallic has occurred upon intercalation into the pores of the mesostructure. That is to say that the pores within the mesoporous structure become saturated with the organometallic and hence, the open pore framework of the starting material is reduced in surface area and pore volume.

**vi. Scanning Electron Microscopy (SEM)**

SEM is an instrument designed primarily for studying the surfaces of solids at high magnifications. Unfortunately, for our purposes the instrument resolution is not high enough and it will be difficult to accurately resolve the 20 Å pores of the mesoporous material. For this reason, the SEM images will be primarily used to study the effect of particle size on the physical behaviour of the composite. Images obtained should also give us an indication as to the composition of the material surfaces and pore

structures of the composite when comparisons are made between the starting material and the product. Thus, the starting material is expected to have well defined pore structure, whereas the product isolated is expected to display a less well-defined image. The latter is anticipated since the pore divots should be more shallow and darker in colour (as compared to the starting material) due to the adsorption of the organometallic cobaltocene species into the pores of the mesoporous material.

**vii. Elemental Analysis (E.A.)**

Elemental analysis of the isolated composites will provide information from which the empirical formulas for each species can be calculated. Comparisons of the starting materials to the intercalated products should show:

- An increase in carbon content relevant to the addition of the organometallic (due to the presence of the biscyclopentadienyl rings) and
- a clear indication as to the calculated M:Co (M = Nb, Ti, Ta) mole ratio for each product obtained.

**viii. Superconducting Quantum Interference Device (SQUID) Magnetometer Studies**

SQUID Magnetometry allows the researcher to probe into the magnetic properties of the material under investigation. Experiments are usually conducted at low temperatures and varying field strengths to determine the effect of both on the system. Plots of Magnetisation versus (vs.) Temperature (M vs. T) and Field vs. Magnetisation (H vs. B) are conducted to give a clear indication as to whether the material is paramagnetic



or superparamagnetic. These magnetic properties can be determined according to the relevant magnetic plots obtained. For example, with regards to the B vs. H plots, little to no hysteresis indicates the isolation of a material with paramagnetic properties, while an observed hysteresis for the plot indicates a material with superparamagnetic or ferromagnetic properties.

Similarly for the M vs. T plots of these materials from 5 K to 100 K at variable field strengths (100 G, 250 G, 500 G and 10000 G), an observed Zero Field Cooled (ZFC) Field Cooled (FC) bifurcation is indicative of a material possessing superparamagnetic properties, while no bifurcation normally indicates a paramagnetic material.

## 2.2. Results and Discussion

### 2.2.1. Synthesis of a Superparamagnetic Cobaltocene – Mesoporous Niobium Composite. (1)

When excess cobaltocene ( $\text{CoCp}_2$ ) was added to a toluene solution of trimethylsilated mesoporous niobium oxide (Nb-TMS1) (prepared with an octadecylamine template) possessing a Brunauer, Emmett, Teller (BET) surface area of  $450 \text{ m}^2\text{g}^{-1}$ , an Horvath Kawazoe (HK) pore size of  $20 \text{ \AA}$ , a cumulative pore volume of  $0.295 \text{ cm}^3\text{g}^{-1}$ , a calculated wall thickness of  $32 \text{ \AA}$  and a central peak in the X-ray powder diffraction pattern (XRD) at  $d = 45 \text{ \AA}$ , a change in colour from faun (Nb-TMS1) to dark olive green was observed. Filtration followed by repeated washings with toluene led to the isolation of a dark olive green air sensitive material **1** with a BET surface area of  $230.82 \text{ m}^2\text{g}^{-1}$ , an HK pore size of  $20 \text{ \AA}$ , a cumulative pore volume of  $0.209 \text{ cm}^3\text{g}^{-1}$  and an XRD diffraction peak centred at  $d = 45 \text{ \AA}$ . These data show that the mesostructure had been retained. **Figure 17(a)** shows the nitrogen adsorption isotherm for the trimethylsilated mesoporous starting material Nb-TMS1 while **Figure 17(b)** shows the isotherm for material **1**. The XRD pattern for the trimethylsilated Nb-TMS1 is shown in **Figure 18(b)**, while **Figure 18(a)** shows that for **1**.

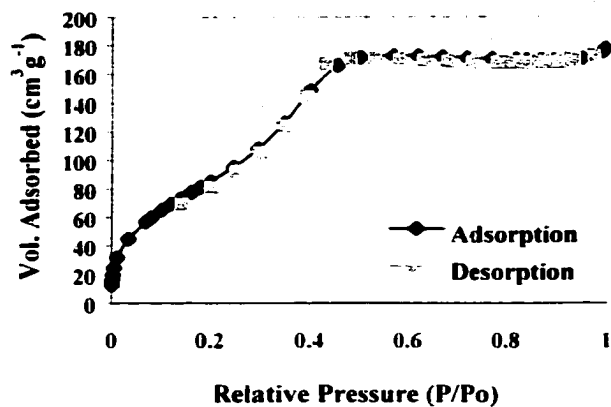


**Figure 17(a):** Nitrogen Adsorption Isotherm for the Trimethylsilated Nb-TMS1 Starting Material.

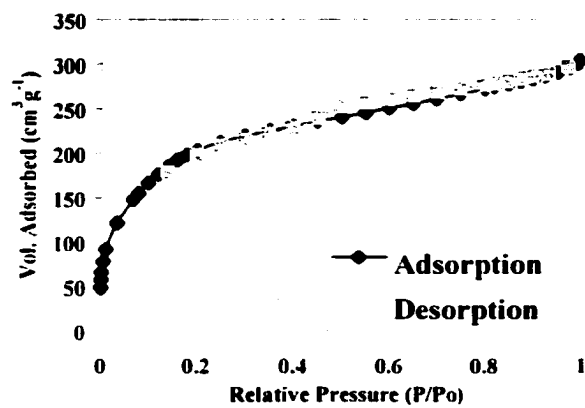


**Figure 17(b):** Nitrogen Adsorption Isotherm for Material 1.

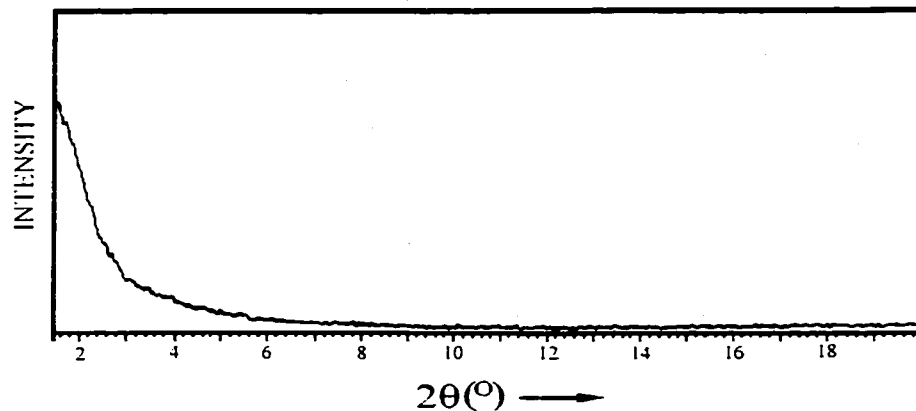


**Figure 18(a): XRD Diffraction Pattern for 1.**

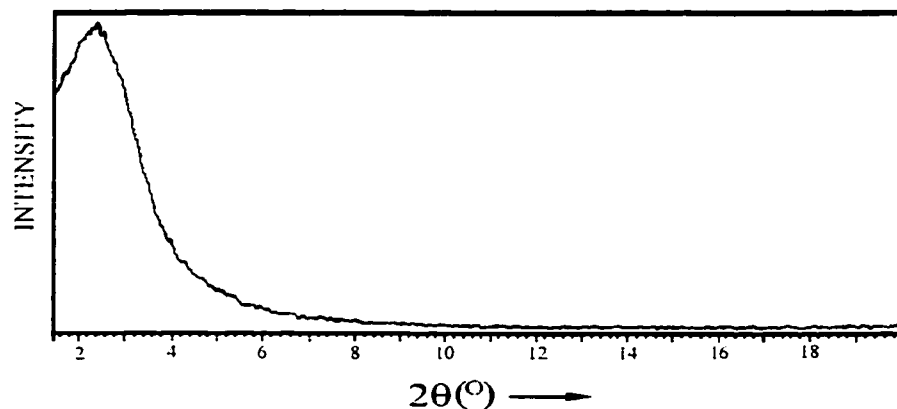
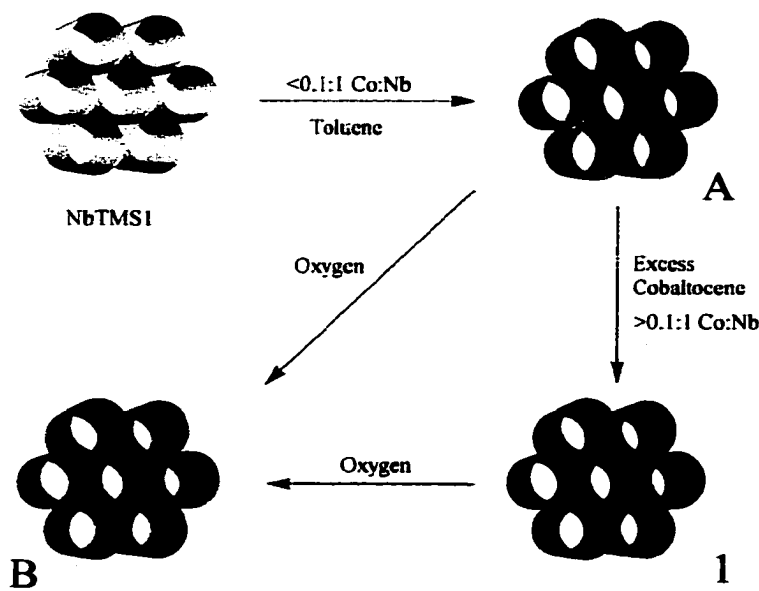


**Figure 18(b): XRD Diffraction Pattern for Trimethylsililated Nb-TMS1.**

Elemental analysis gave the following calculated empirical formulas:  $C_{14}H_{59}NNb_{18}SiO_{73}$  for the trimethylsililated Nb-TMS1 starting material and  $C_{75}H_{142}N_2SiNb_{34}Co_5O_{136}$  for material **1**. The increase in carbon content, when comparing the starting material (5.38%) to material **1** (13.47%) is consistent with the retention of the cyclopentadienyl rings in the intercalated cobalt (Co) species. For **1** the Nb:Co mol ratio was calculated as 1:0.147. This ratio relates to the saturation loading level of  $CoCp_2$

within the composite. Oxidation of **1** led to a colour change from dark olive green to bright green **B** (Scheme 5). Elemental analysis of the oxidized material gave a calculated empirical formula of  $C_{43}H_{124}N_2Nb_{23}Co_3SiO_{124}$  with a Nb:Co mol ratio of 1:0.130.



**Scheme 5:** Synthesis of Nb-TMS1CoCp<sub>2</sub> (**1**). Giving the Non Saturated Mesoporous Species **A** (Black) and Upon Further Additions of CoCp<sub>2</sub> the Saturated Product –Material (**1**) Dark Green in Colour. Oxidation of Both Species Led to the Isolation of the Bright Green Coloured Material **B**.

X-ray Photoelectron Spectroscopy (XPS) of **1** (calibrated to the Carbon C-(C,H) ion at 284.8 eV) was conducted to determine the degree of electron transfer in composite **1**.<sup>99,100</sup> The Co 2p 3/2 region, **Figure 19(a)**, indicated that at saturation the mesoporous material **1** contained both Co (II), 779.3 eV and Co (III), 780.9 eV, corresponding to Cp<sub>2</sub>Co and Cp<sub>2</sub>Co<sup>+</sup>. The calculated Co(II):Co(III) ratio of this material was 1:1.07 derived from the intensities for each species. There was no evidence from the spectrum that either cobalt metal nor cobalt oxide (at the expected binding energy of 778 eV) were

present. This indicated that no decomposition of the cobaltocene had occurred within the system.

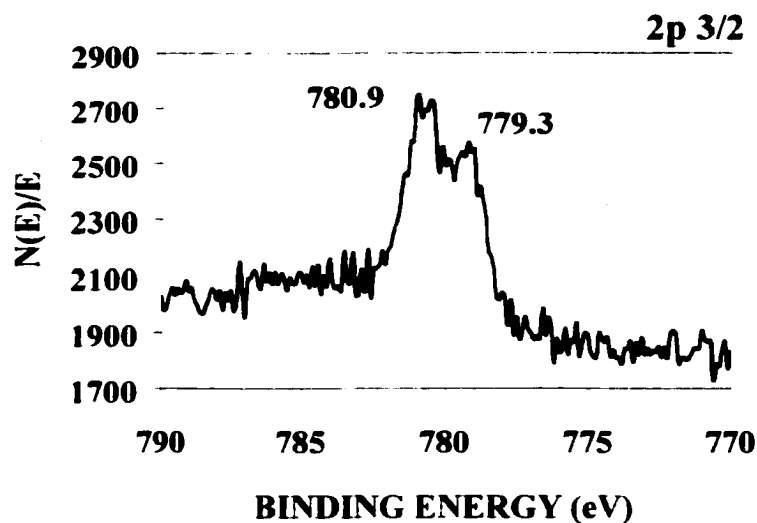


**Figure 19(a):** XPS Spectrum for Co 2p 3/2 Region for **1**.

The inverse result (reduction of an element leads to a reduction in observed binding energy) was observed for the niobium 3d 5/2, 3/2 region (**Figure 19(b)**). The Nb 3d 5/2, 3/2 region for **1** showed emissions at 206.9 eV and 209.6 eV respectively. These values had shifted from those for the trimethylsilated Nb-TMS1 starting material at 207.8 eV and 210.5 eV respectively, indicating a slight reduction from the V to IV state. No peaks could be assigned to the Nb metal at 202 eV.<sup>104</sup> Interestingly, no observable reaction occurred between cobaltocene and pure Nb<sub>2</sub>O<sub>5</sub> in toluene. This is because the amorphous nature of the walls allows for the presence of acceptor states of lower binding energy than in the bulk oxide. This effect is common in amorphous solids, which generally have much wider bandwidths than their crystalline counterparts.<sup>85</sup>

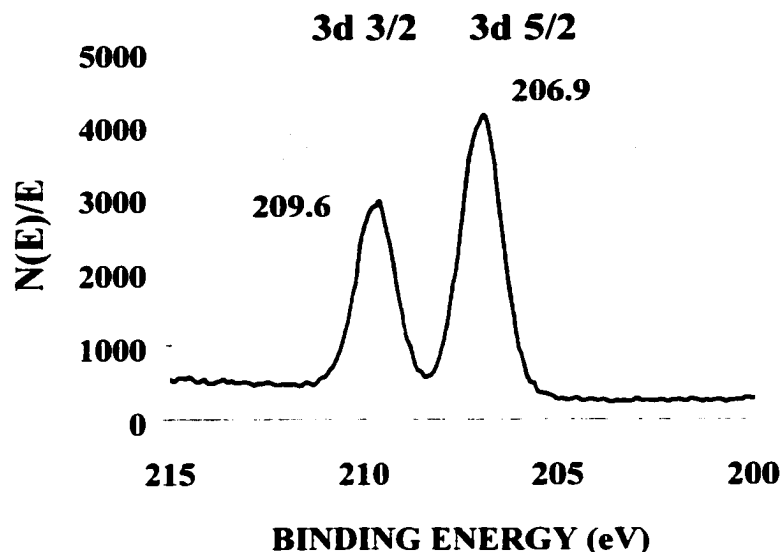


**Figure 19(b):** XPS Spectrum for Nb 3d 5/2, 3/2 Region for 1.

Electron Paramagnetic Resonance (EPR) analysis of compound 1, **Figure 20**, showed two peaks, one correlating with the free electron (3376 G) within the composite and the second smaller peak (3239 G) corresponding to the paramagnetic cobaltocene species. Since cobaltocinium has no unpaired electrons and is diamagnetic, no observable EPR signal for this species is detectable. Previous studies have shown<sup>101,102</sup> that refined EPR spectra of pure cobaltocene are generally difficult to achieve even at liquid He temperatures (4.2 K). This is due to the very slow relaxation rate of the organometallic moiety compared to the analysis time scale. A refined peak is obtainable by doping the cobaltocene into a non-paramagnetic species such as ferrocene. For the purpose of our investigations analysis temperatures below 77K were not experimentally possible. For this reason, the peaks attributed to the Co(II) were broad and less well resolved than those referenced in literature.

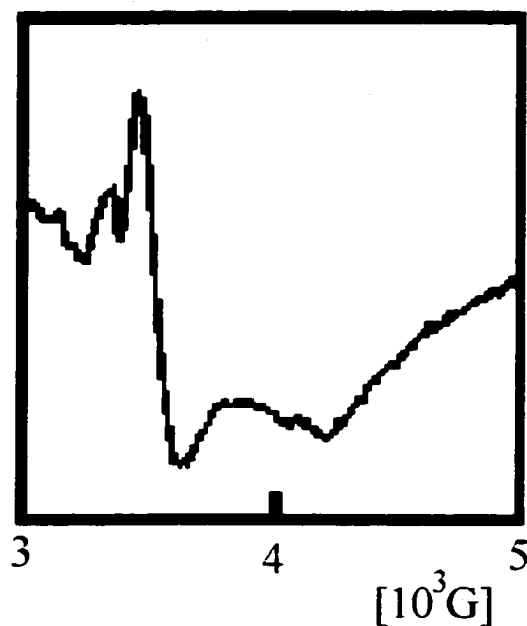


**Figure 20: EPR Spectrum for 1.**

The Ultraviolet (UV) visible reflectance spectrum of **1** showed three broad peaks at 260 nm, 420 nm and 580 nm. The peak at 260 nm corresponds to the Nb-O 2p valence band-to-conduction band transition with a band gap of roughly 3.3 eV.<sup>105</sup> The peak at 420 nm corresponds to the cobaltocinium<sup>106</sup> cation  $\pi$ - $\pi^*$  transition and further supports that an electron transfer from the cobaltocene to the mesoporous framework had occurred. This peak further confirms the presence of cobaltocinium in the mesoporous material and indicates that the composite has retained its structural integrity after intercalation of the organometallic. The broad peak at 580 nm corresponds to a transition from a Nb4d cobaltocene impurity band to the conduction band.<sup>105</sup>

Conductivity measurements for pressed pellets of material **1**, under an inert atmosphere of nitrogen, showed that the composite was an insulator with conductivity values of  $10^{-7}$  ohm<sup>-1</sup> cm<sup>-1</sup> or less. Cyclic voltammograms for both the trimethylsilated Nb-TMS1 starting material and that for the product **1** indicated no conductivity patterns



and hence negligible drain currents flowing through the system. These insulating properties have also been observed for Nb-TMS1 materials reduced with the alkali metals, Na, K, Li, Cs and Rb.<sup>85</sup>

Low temperature magnetic measurements conducted on a SQUID Magnetometer revealed that **1** was superparamagnetic and consequently, the mesostructure consists of a framework within which separate magnetic regions, referred to as domains, exist. The size of these domains is generally in the order of  $<1 \mu\text{m}$  and when subjected to thermal fluctuations these magnetic regions can easily reverse the direction of the samples magnetic moment (a property normally associated with nanoclusters of soft magnetic materials and ferrofluids).<sup>107</sup> This is the first report of a molecular superparamagnet, and the origin of this behaviour is thus an issue of great importance.

The Magnetisation versus Temperature plot (M vs. T), conducted at varying field strengths (100 G, 250 G, 500 G and 10000 G) from 5 to 100 K, illustrated the expected crossover between the Zero-Field Cooled (ZFC) and Field Cooled (FC) regions indicative of superparamagnetism. (**Figure 21(a)**).

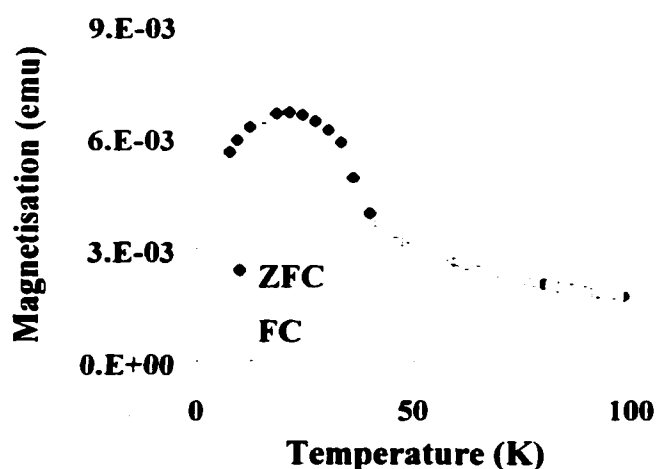


**Figure 21(a):** M vs. T Plot (At 250 G) for **1** Illustrating the ZFC FC Bifurcation.

Material 1 exhibited a mean blocking temperature ( $T_b$ ) of 18 K relevant to the maximum magnetisation achieved in the ZFC region. Below this temperature the superparamagnetic particles are blocked, and thus are restricted from rotating freely in response to the applied magnetic field.<sup>108</sup> Above 18 K the material exhibited standard Curie behaviour whereby the magnetic permeability is inversely proportional to temperature. The temperature dependence of the ZFC and FC plots indicated that superparamagnetism is present within nanoclusters of the composite and the observed increase in the FC region was consistent with the presence of ultrafine superparamagnetic particles.<sup>109</sup>

The Magnetisation vs. Field (B vs. H) plot of 1 conducted at two temperatures (10 K and 300 K) above and below the mean blocking temperature (18 K) is shown in **Figure 21(b)**.

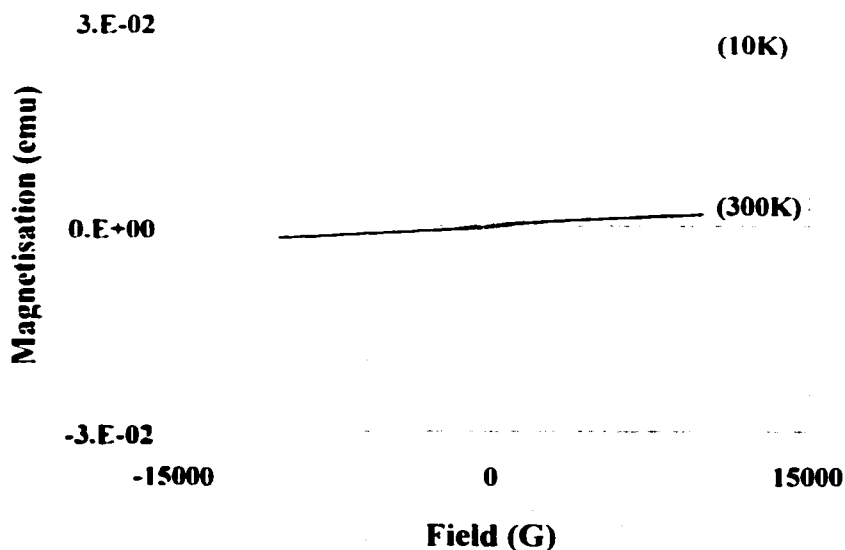


**Figure 21(b):** B vs. H Plot for 1 obtained at 10 K and 300 K.

At lower temperatures (10 K) the magnetisation of the sample increased and gave a symmetric curve with low hysteresis indicative of superparamagnetic materials. At saturation magnetisation ( $M_s$ ) for material 1 (achieved at  $2.68 \times 10^{-2} \text{ emu g}^{-1}$ ), the increase in magnetisation slowed substantially and approximately linearly with the increase in field strength. This is said to be the intrinsic magnetisation for the system and is equal to the value of magnetisation within a single domain.<sup>110</sup> At higher temperatures, 300 K, a rapid linear increase dependent on the increasing applied magnetic field was observed. Saturation magnetisation for the composite at this elevated temperature (300 K) was not attained. From the B vs. H plot at 10 K, the size of the precipitates can be calculated. Assuming the superparamagnetic behaviour is a property of all the particles having the same spherical volume, we can apply the data from the graph to the Langevin Function:<sup>111</sup>

$$M = M_s \left\{ \coth(\alpha) - \frac{1}{\alpha} \right\}, \quad \alpha = \frac{\mu_0 M_{Co} V H}{K_B T}$$

where M is the magnetisation of the sample.  $M_s$  is the saturation magnetisation of the sample,  $M_{Co}$  is the magnetisation of cobalt,  $K_B$  is the Boltzman's constant, V is the volume of the precipitates, T is the Temperature for the plot (K),  $\mu_0$  is the permeability magnetic moment for the sample, coth is the hyperbolic cotangent. H is the applied field and  $\alpha$  is the particle magnetic moment. The calculated diameter for the Co particles within this composite was 14 nm, indicating that cobaltocene phases within a single nanotube are responsible for the superparamagnetic behaviour of the mesoporous material. Scanning Electron Microscope (SEM) images of these composites gave an average mesoporous particle size of 10  $\mu\text{m}$ , much larger than the calculated

superparamagnetic domain size, adding further support to the view that the superparamagnetic regions are within one or several adjacent pores and hence do not span across entire particles. Cigar-shaped  $\text{Fe}_2\text{O}_3$  nanoclusters of similar size and with similar B vs. H curves to material **1** have been reported previously by Ying *et al.*<sup>109</sup>

### 2.2.2. Probing the Effect of Wall Thickness on a Superparamagnetic Cobaltocene Mesoporous Niobium Composite (**2**)

It is unclear whether the superparamagnetism arises in this system from the cobaltocene clusters within the pore structure, or whether there is some co-operative effect between the magnetic moments of these particles and the unpaired electrons in the walls of the mesostructure. Therefore, we chose to investigate how variation of wall thickness, while keeping the HK pore size the same, would effect the system. To a toluene solution of trimethylsilated Nb-TMS1 (prepared from a dodecylamine template) with a BET surface area of  $947 \text{ m}^2\text{g}^{-1}$ , a cumulative pore volume of  $0.62 \text{ cm}^3\text{g}^{-1}$ , an HK pore size of  $20 \text{ \AA}$ , a calculated wall thickness of  $20 \text{ \AA}$  and an XRD diffraction pattern centred at  $d = 35 \text{ \AA}$  was added excess  $\text{CoCp}_2$ . The nitrogen adsorption isotherm and the XRD diffraction pattern for the trimethylsilated Nb-TMS1 material are shown in **Figures 22(a)** and **23(a)** respectively. The precipitate immediately changed in colour from a faun (for that of the trimethylsilated mesoporous material, Nb-TMS1) to dark olive green. The solution was left to stir under an inert atmosphere of nitrogen for several days then filtered with toluene until the filtrate remained clear. The isolated product (**2**), with a BET surface area of  $220 \text{ m}^2\text{g}^{-1}$ , a cumulative pore volume of  $0.15 \text{ cm}^3\text{g}^{-1}$ , an HK pore size of  $19\text{-}20 \text{ \AA}$  and an XRD diffraction pattern at  $d = 36 \text{ \AA}$ , was then dried in *vacuo*. The

drop in pore volume, BET surface area and HK pore size in the product was consistent with partial occlusion of the pores by the organometallic species. The nitrogen adsorption isotherm and the XRD diffraction pattern for **2** are shown in **Figures 22(b)** and **23(b)** respectively.

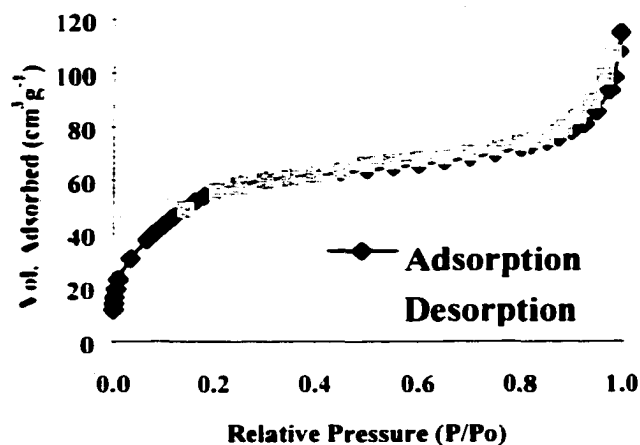


**Figure 22(a)** Nitrogen Adsorption Isotherm for Trimethylsilylated Nb-TMS1.

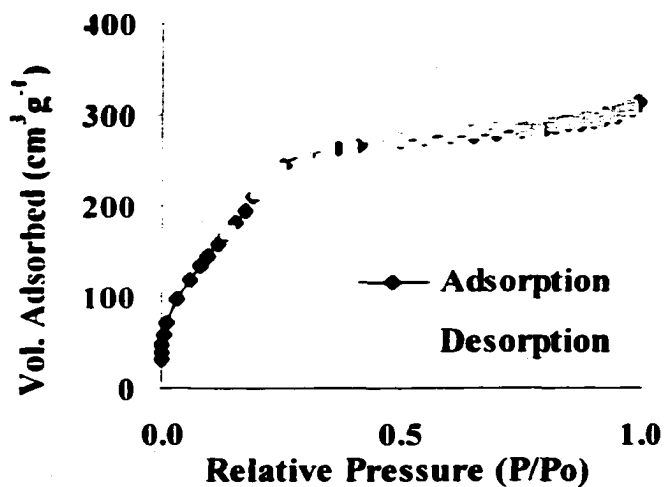


**Figure 22(b):** Nitrogen Adsorption Isotherm for **2**.

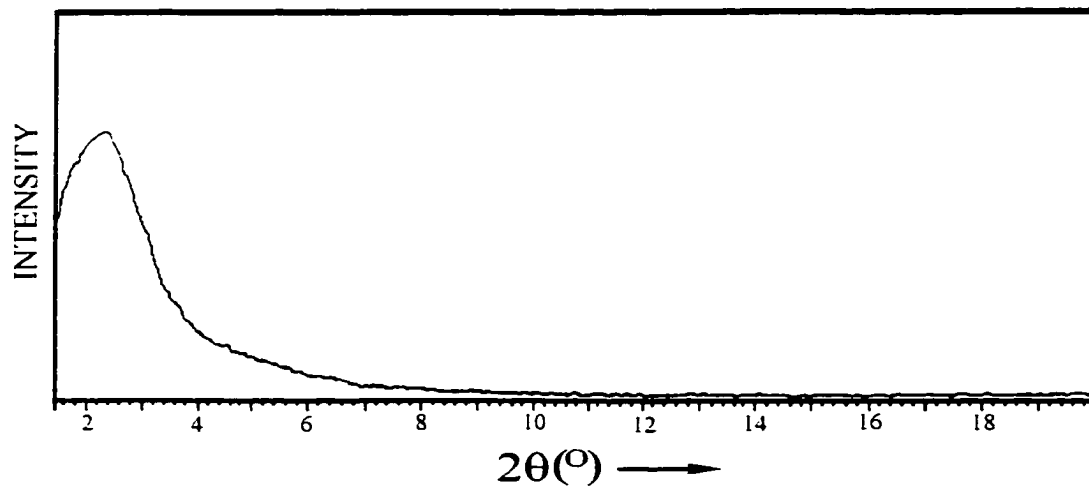


**Figure 23(a):** XRD Diffraction Pattern for Trimethylsilated Nb-TMS1.

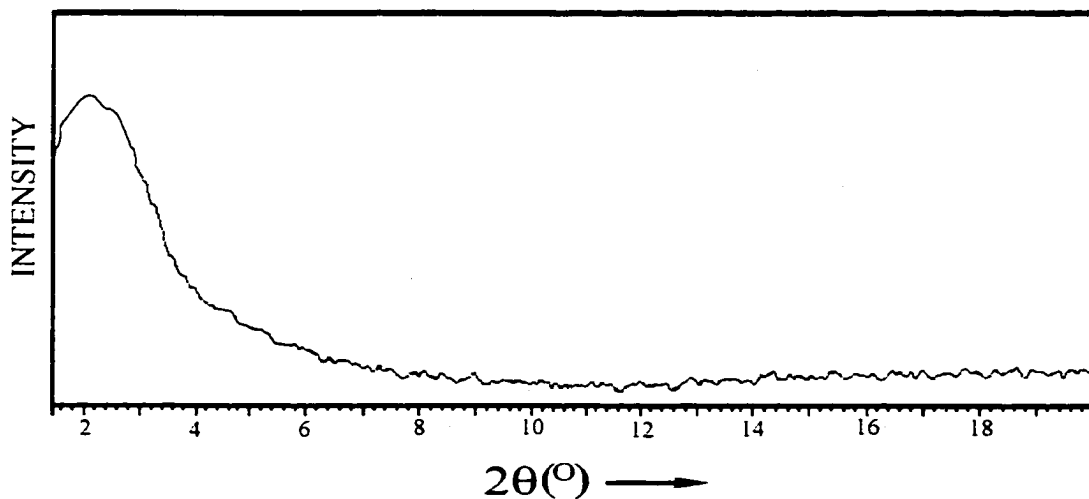


**Figure 23(b):** XRD Diffraction Pattern for Material 2.

Elemental analysis (E.A.) gave a calculated empirical formula:  $C_9H_{38}NNb_{17}SiCl_5O_{53}$  for the trimethylsilated Nb-TMS1 composite and  $C_{435}H_{614}N_8Nb_{86}SiCo_{42}Cl_{23}O_{380}$  for the isolated product material 2. The calculated Co:Nb

mol ratio of 0.5:1.0 showed an increase from the ratio previously calculated for the thicker walled mesoporous material 1 (0.147:1.0). Elemental analysis also reflected an increase in carbon content from 3.85% to 22.29%, consistent with retention of the cyclopentadienyl rings on the organometallic Co species.

XPS analysis (**Figure 24**) for the Co 2p 3/2 region of the mesoporous composite 2 gave a Co(II):Co(III) (779.7 eV and 781.1 eV respectively) mol ratio of: 1:1.03, a slight change from that of the thicker walled composite 1, indicating that a change in wall thickness of the material, while holding the pore size constant, had little effect on the ratio of Co(II):Co(III) in the isolated product. The Nb 3d 5/2, 3/2 region (**Figure 25(a)**) showed a slight reduction in binding energy for material 2 (206.9 eV, 209.8 eV) when compared to the starting trimethylsilated Nb-TMS1 material (207.6 eV, 210.4 eV) shown in **Figure 25(b)**, indicating that partial reduction of the niobium from the +5 to the +4 oxidation state had once again been achieved and was consistent with results obtained for material 1.

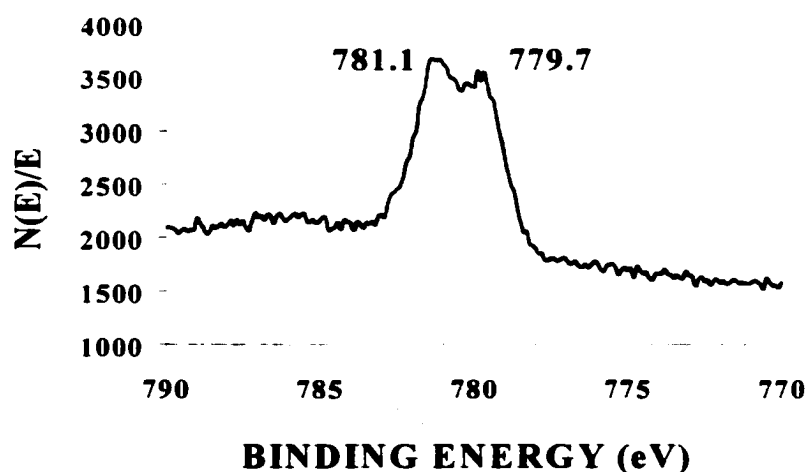


**Figure 24:** XPS Co 2p 3/2 Region for 2.

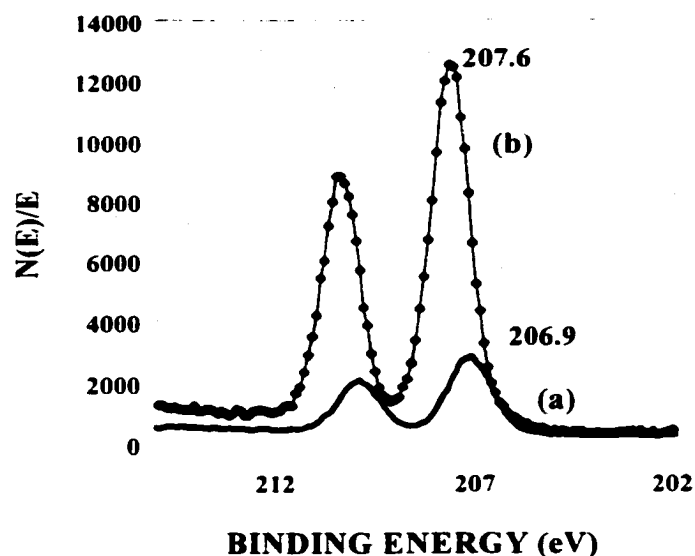


**Figure 25:** XPS Nb 3d 5/2, 3/2 Regions for the Trimethylsilated Nb-TMS1 (a) Composite and that for **2** (b).

Surprisingly, XPS studies revealed (as evidenced from XPS data for the Cl 2p 3/2, 1/2 region) the presence of chlorine within the system. The chlorine is thought to exist as hydrochloric acid (HCl) present on the surface of the material and is the major product formed when Nb-TMS1 is treated with excess chlorotrimethylsilane (TMSCl). In previous studies,<sup>112,113</sup> silylation of mesoporous materials with TMSCl has shown to enhance the stability towards moisture and compression due to the improved hydrophobicity of the mesostructures. This process was adopted to ensure complete ‘capping’ of dangling hydroxyl (OH) groups within the mesoporous cavities. Once treated, the mesoporous material was thoroughly dried to remove all volatile species such as the solvent – diethyl ether, any excess TMSCl and HCl. Unfortunately, complete



removal of the HCl from the system had proven to be difficult and E.A. had revealed that the Cl content within these systems was consistently 5-6% by weight.

The UV reflectance spectrum of this saturated material showed the presence of peaks at 260 nm, 420 nm (broad) and 580 nm (broad) consistent with those discussed for the previous sample of the Nb based material 1.

The EPR spectrum for **2** (**Figure 26**) registered a peak at 3384 G assigned to the presence of the free electron in the Nb-based mesoporous material and a minor peak (3241 G) for the neutral cobaltocene present within the mesostructure. The second peak is consistent with the presence of the paramagnetic cobalt species within the pores.<sup>114,115</sup>

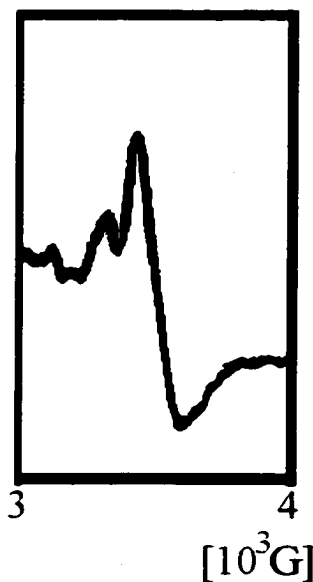


**Figure 26:** EPR Spectrum for 2.

Magnetic measurements conducted at low temperatures on a SQUID magnetometer revealed that for both the M vs. T (**Figure 27**) and B vs. H (**Figure 28**) plots material **2** was superparamagnetic.

The M vs. T plot for the intercalated composite **2** showed a visible ZFC FC bifurcation correlating to a mean blocking temperature of 18 K, indicating that the superparamagnetic properties observed for these systems are not effected by a reduction in wall thickness for the mesoporous material and that the superparamagnetism arose from the Co contributions and not from the Nb-oxide mesostructure.

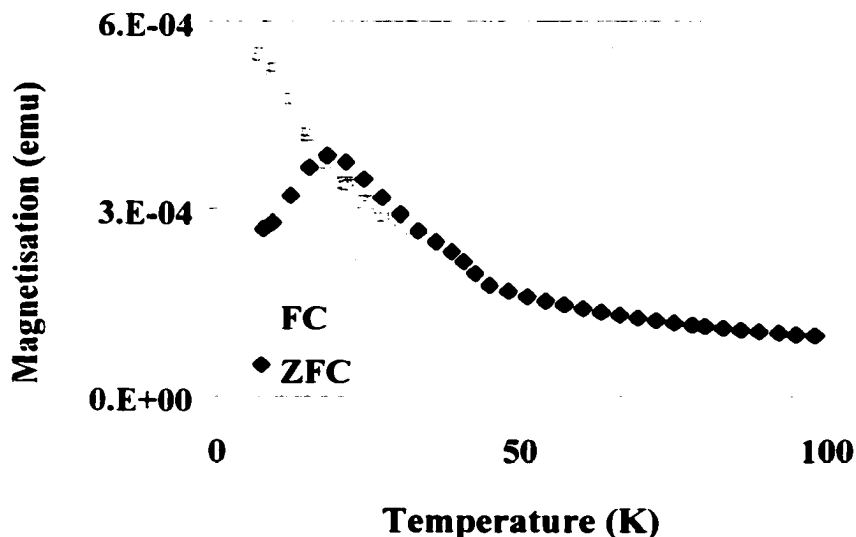


**Figure 27: M vs. T Plot for 2.**

The B vs. H plots (10 K) further confirmed the superparamagnetic properties of this material because the sample magnetisation increased with field giving a symmetric hysteresis loop for the plot and a  $M_s$  value of  $6.02 \times 10^{-2} \text{ emu g}^{-1}$ . Furthermore, application of the Langevin Function at 10 K gave a mean particle domain size of 14 nm. SEM images gave a mean particle size of 10  $\mu\text{m}$ .

At elevated temperatures (300 K), the material showed a rapid linear increase in magnetisation as the field was increased. No hysteresis was observed and  $M_s$  was not reached for the system. These plots further underlined that a change in wall thickness had little influence on the superparamagnetic properties of these materials and that because of this, the free electrons in the wall have only a small or no effect on the magnetic properties of the composites.

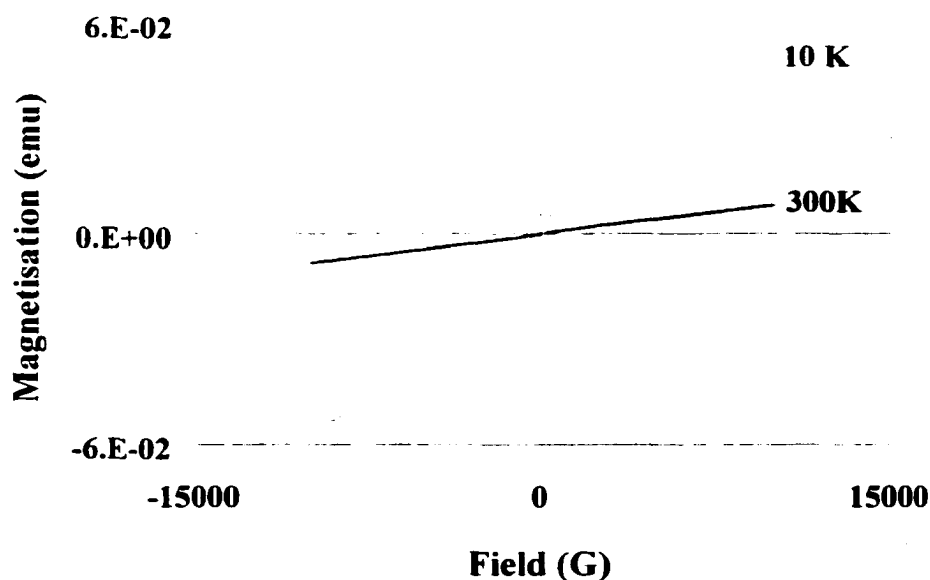


**Figure 28: B vs. H Plot for 2.**

Conductivity measurements on pressed pellets and cyclic voltammograms of material 2 revealed the product to be an insulator, consistent with results from the previously discussed material 1.

### 2.2.3. Probing the Effect of Pore Size on a Superparamagnetic Cobaltocene Mesoporous Niobium Composite (3)

To investigate the effect of pore size on the superparamagnetic properties in these materials, we prepared a trimethylsilated Nb-TMS1 sample (synthesised with an octadecylamine template), with a BET surface area of  $870 \text{ m}^2\text{g}^{-1}$ , a cumulative pore volume  $0.655 \text{ cm}^3\text{g}^{-1}$ , an HK pore size of  $29 \text{ \AA}$  and a calculated wall thickness of  $20 \text{ \AA}$ . After treatment with excess cobaltocene (in toluene) the isolated dark olive green product **3** had a new reduced BET surface area of  $187 \text{ m}^2\text{g}^{-1}$ , a cumulative pore volume of  $0.217 \text{ cm}^3\text{g}^{-1}$  and an HK pore size of  $26 \text{ \AA}$ . The nitrogen adsorption isotherm for the trimethylsilated Nb-TMS1 material is shown in **Figure 29(a)** while the isotherm for material **3** is shown in **Figure 29(b)**.

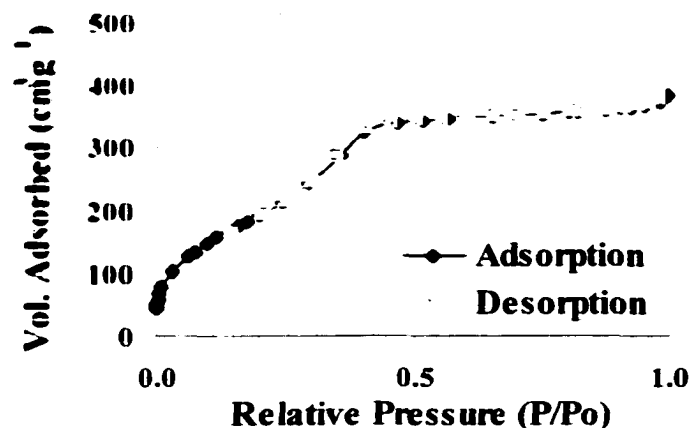


**Figure 29(a):** Nitrogen Adsorption Isotherm for the Trimethylsilated Nb-TMS1 Mesoporous Material.

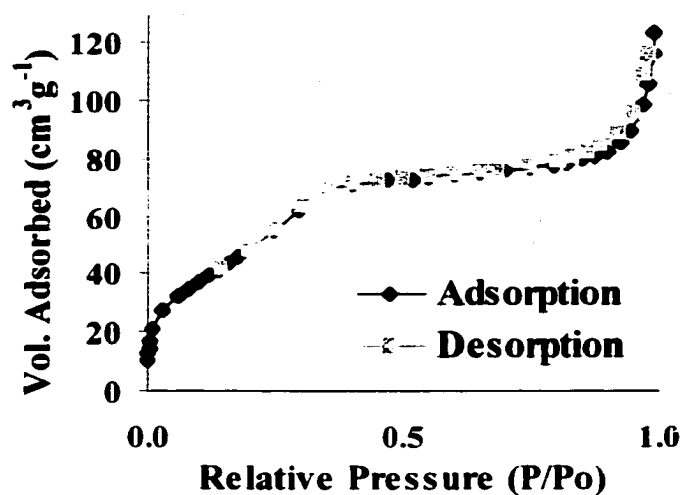


**Figure 29(b):** Nitrogen Adsorption Isotherm for Material **3**.

XRD diffraction patterns for the Nb-TMSI trimethylsilated starting material ( $d = 45 \text{ \AA}$ ) and for **3** ( $d = 46 \text{ \AA}$ ) indicated that upon intercalation of the organometallic retention of the mesostructure was observed as expected. (**Figure 30(a) and 30(b)** respectively).

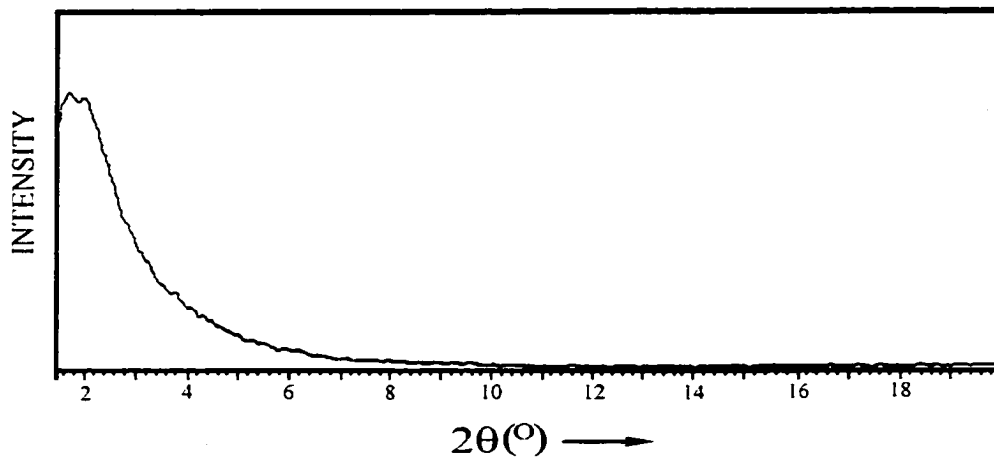


**Figure 30(a):** XRD Diffraction Pattern for the Trimethylsilated Mesoporous Material Nb-TMS1.

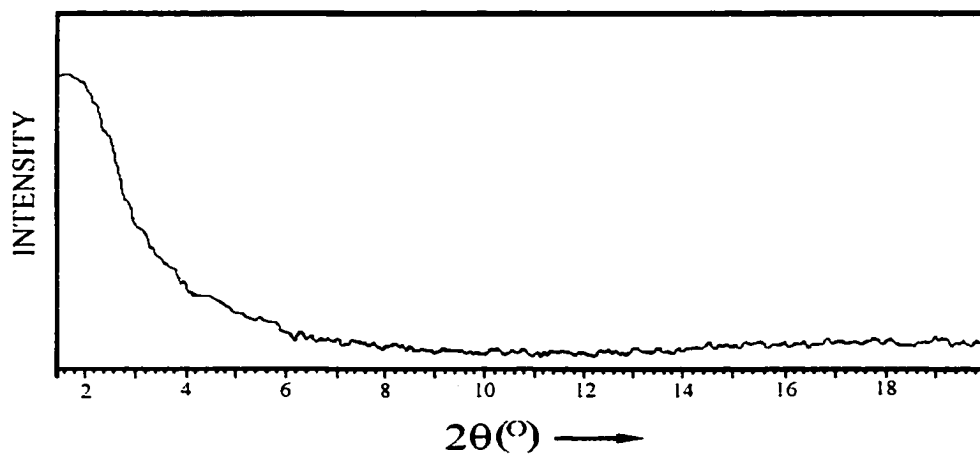


**Figure 30(b):** XRD Diffraction Pattern Obtained for 3.

Elemental analysis of the trimethylsilated mesoporous Nb-TMS1 composite gave a calculated empirical formula of  $C_{21}H_{90}N_3Nb_{46}SiCl_{13}O_{144}$ , while that for material 3 gave

$C_{367}H_{444}N_6Nb_{53}SiCo_{26}Cl_{14}O_{230}$  and a Nb:Co mol ratio of 1.0:0.5. As in the previous intercalated mesoporous materials **1** and **2**, a substantial increase in carbon content between the starting material (3.34 %) and the product (28.24%) was observed. This is consistent with the retention of the cyclopentadienyl rings on the Co moiety.

XPS (**Figure 31(a)**) analysis of the Co 2p 3/2 region for **3** gave an integrated intensity ratio of Co(II) to Co(III) of 1:1.13 respectively, a slight change from that previously observed for both materials **1** and **2** (1:1.03). From these observations, we concluded that a shift to larger pore size had little effect on the level of adsorption and retention of the organometallic moiety in this system. The Nb 3d 5/2, 3/2 region of this material (**Figure 31(b)**) shows a peak at 206.9 eV and 209.6 eV consistent with partial reduction of the Nb to an average state between +4 and +5. This reduction was consistent with results previously observed for materials **1** and **2**.

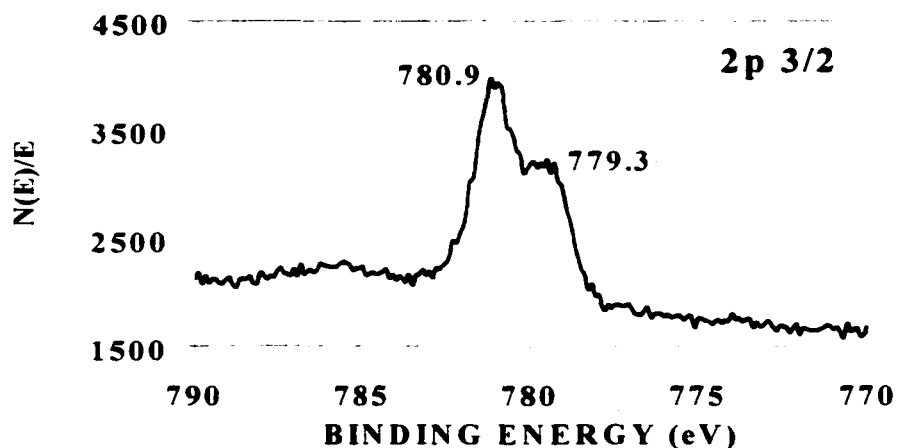


**Figure 31(a):** XPS Spectrum of the Co 2p 3/2 Region for **3**.

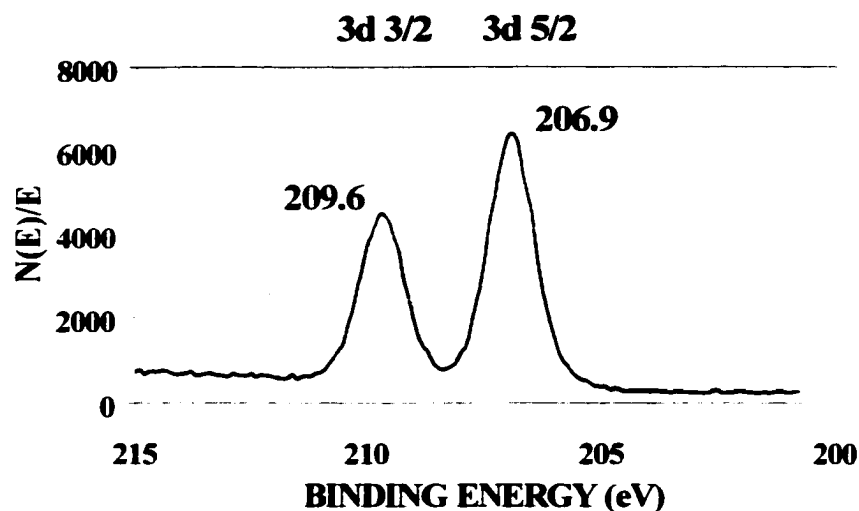


**Figure 31(b):** XPS Spectrum of the Nb 3d 5/2, 3/2 Region for **3**.

The EPR spectrum for material **3** was virtually identical to the spectra recorded for materials **1** and **2** showing the one large peak for the free electron in the Nb-oxide based mesostructure and the second smaller peak for the paramagnetic cobaltocene species. The UV reflectance spectrum of material **3** showed absorbances at 260 nm, 420 nm (broad) and 580 nm (broad) consistent with those for materials **1** and **2**. Cyclic Voltammograms for both the trimethylsilated Nb-TMS1 and the composite **3** indicated that the materials were insulators, consistent with conductivity measurements of pressed pellets showing conductivity values of  $10^{-7} \text{ ohm}^{-1} \text{ cm}^{-1}$ .

When investigating the magnetic properties of material **3** at low temperatures, superparamagnetism was again observed. From the M vs. T analysis (**Figure 32(a)**) a mean blocking temperature ( $T_b$ ), for the ZFC region was observed at 18 K consistent with the materials **1** and **2**.



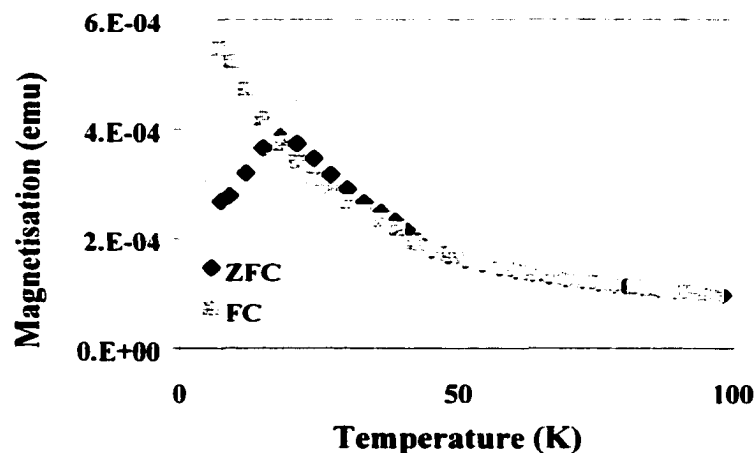


**Figure 32(a): M vs. T Plot for 3.**

**Figure 32(b)** shows the B vs. H plot of **3** at 10 K giving the expected hysteresis loop, with  $M_s$  equal to  $6.39 \cdot 10^{-2} \text{ emu g}^{-1}$ . The B vs. H plot at 300 K gave no hysteresis and the linear increase with increasing applied field was again observed. We conclude from these results that a change in pore size does not effect the magnetic behaviour of the mesoporous composite.

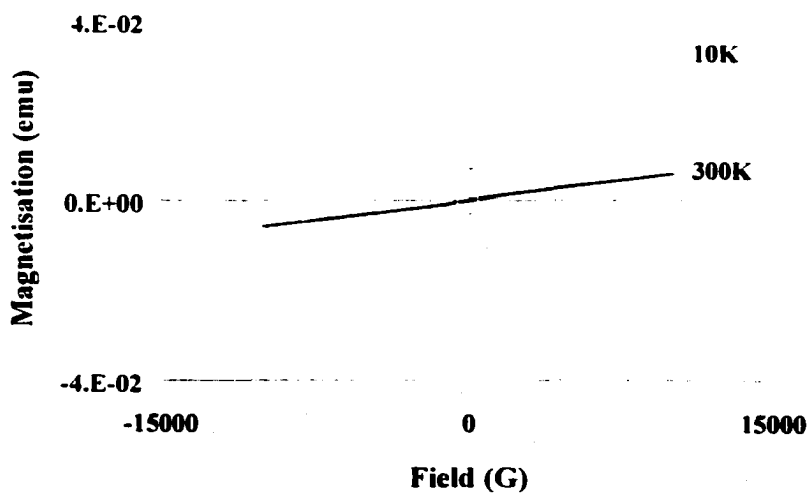


**Figure 32(b): B vs. H Plot for 3.**

Application of the Langevin Function gave a mean particle domain size of 15.3 nm, consistent with the increase in pore size for the composite.

SEM analysis of the trimethylsilated Nb-TMS1 mesoporous material (**Figure 33(a)**) and the image of the composite **3** (**Figure 33(b)**) gave a mean particle size of 9  $\mu\text{m}$ .

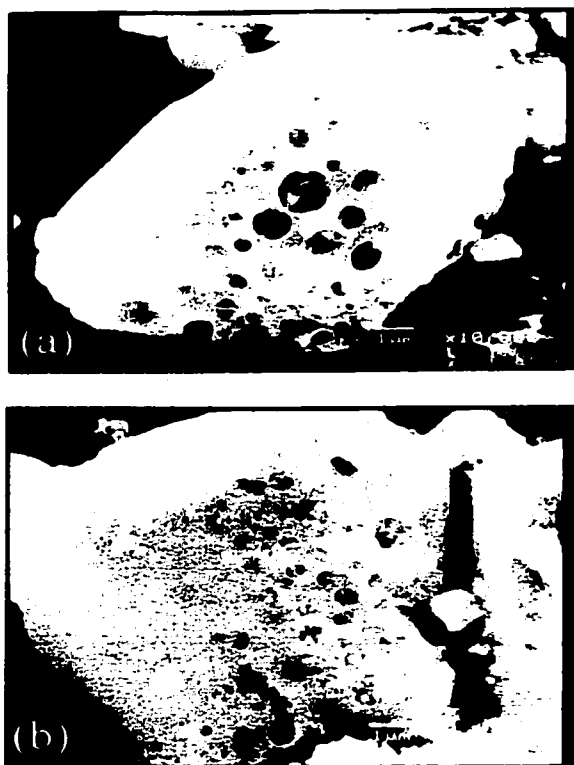


**Figure 33:** SEM Images for (a) Trimethylsilated Mesoporous Nb-TMS1 and (b) **3**.

### 2.2.3.1. An Investigation into the Critical Loading Level and Critical Co(II):Co(III) Ratio Required for the Onset of the Superparamagnetic Transition.

In order to find the critical loading level (Co:Nb mol ratio) and the critical Co(II):Co(III) ratio required for the onset of superparamagnetism within this system, samples of trimethylsilated niobium (Nb-TMS1) were reacted with 0.1 (4) or 0.3 (5) equivalents of cobaltocene (as calculated on the basis of E.A. of the parent oxide ca. 57% Nb by weight). For material 4 the BET surface area showed a drop from 870 m<sup>2</sup>g<sup>-1</sup> (for the trimethylsilated Nb-TMS1 material) to 751.50 m<sup>2</sup>g<sup>-1</sup>, the cumulative pore volume of this material also decreased from 0.655 cm<sup>3</sup>g<sup>-1</sup> to 0.650 cm<sup>3</sup>g<sup>-1</sup>, indicating that intercalation of the organometallic into the framework of the mesoporous material had been achieved. The XRD diffraction pattern for this composite remained unchanged from that of the parent oxide at  $d = 45 \text{ \AA}$ , indicating that the mesostructure was fully retained upon adsorption of the organometallic.

In composite 5, a reduction in the BET surface area (from 870 m<sup>2</sup>g<sup>-1</sup> to 735.42 m<sup>2</sup>g<sup>-1</sup>) and cumulative pore volume (from 0.655 cm<sup>3</sup>g<sup>-1</sup> to 0.634 cm<sup>3</sup>g<sup>-1</sup>) was observed. These results were consistent with the intercalation of the organometallic moiety within the mesoporous material. Whether the mesoporous material was reacted with 0.1 (4), 0.3 (5) or 0.5 (3) equivalents of cobaltocene the XPS spectrum showed the presence of cobaltocinium within the material. The Co(II):Co(III) intensity ratios changed from 1:1.13 (as calculated for material 3) to 1:1.17 for 5. **Figure 31(a), 34(a)**. While there is cobaltocinium in material 4 (**Figure 34(b)**) there is very little cobaltocene, hence the Co(II):Co(III) ratio could not be calculated. In all cases, partial reduction of Nb from +5 to +4 was observed.

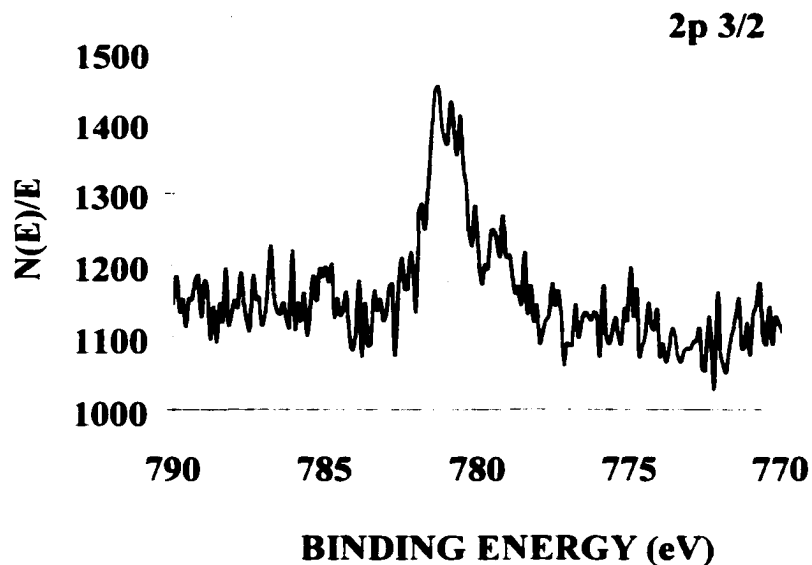


**Figure 34(a):** XPS Spectrum for the Co 2p 3/2 Region for 5.

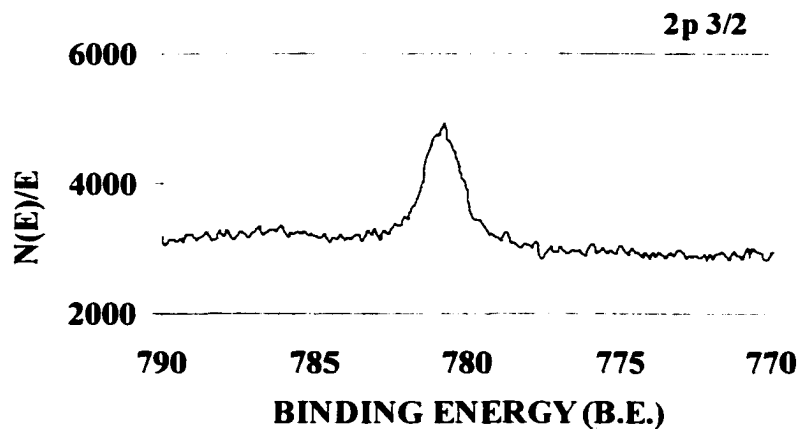


**Figure 34(b):** XPS Spectrum for the Co 2p 3/2 Region for 4.

EPR studies conducted on 4 showed two peaks, one for the paramagnetic Co(II) species and the second larger peak at corresponding to the free electron from the mesoporous composite. The observance of Co(II) (not observed in the XPS studies) was

attributed to the extremely sensitive EPR measurements (detecting paramagnetic species to concentrations as low as  $1 \times 10^{-11}$ ). The peaks were lower in intensity than those for materials **1**, **2** and **3**, consistent with a decreased amount of cobaltocene in the pore structure.

EPR studies conducted on product **5** showed two peaks, one relevant to the free electron within the walls of the mesoporous material centred at 3306.51 G and the second smaller resonance due to the presence of cobaltocene within the mesostructure (ca. 3200 G), consistent with the XPS studies conducted on this material. The G values for this composite correlate more favourably to those measured for materials **1**, **2** and **3**. The EPR peak intensity observed for the cobaltocene paramagnetic species for both **4** and **5** was much lower than that for material **3**, indicating that much less Co(II) was present within these systems.

Low temperature SQUID magnetometry measurements (M vs. T, **Figure 35**) indicated that material **4** was paramagnetic, whereas material **5** (**Figure 36**) showed a superparamagnetic transition with a mean blocking temperature of 18 K. Hence, superparamagnetism occurs in this system when the Co:Nb ratio was increased beyond 0.1:1.0.

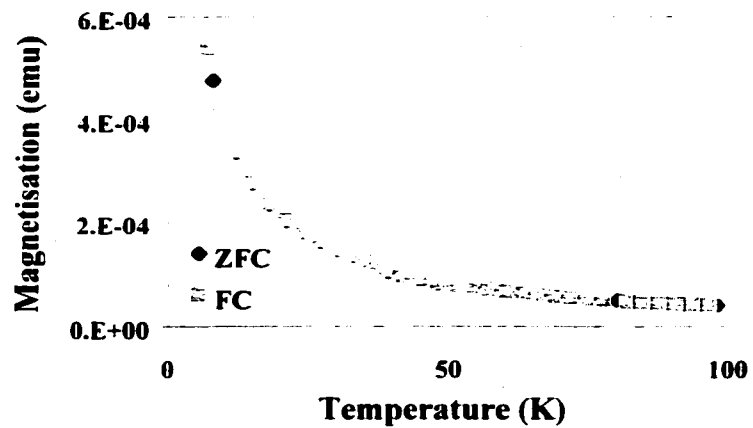


Figure 35: M vs. T Plot for 4.

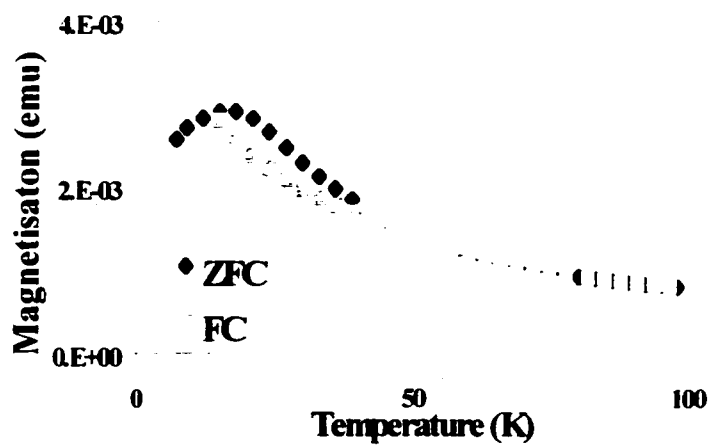
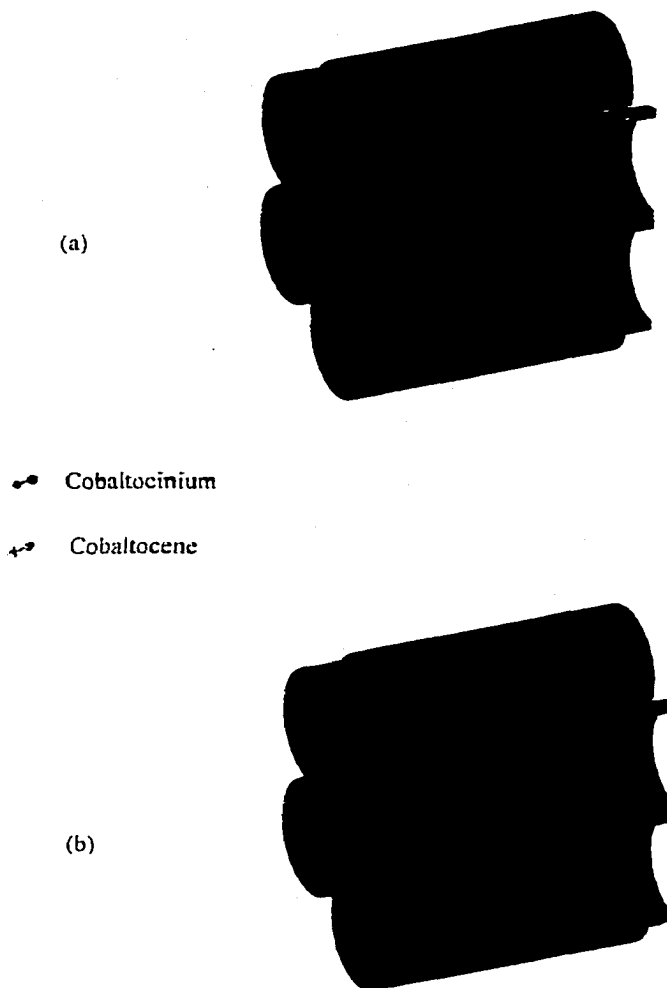


Figure 36: M vs. T Plot for 5.



**Scheme 6:** A Schematic Representation of the Theoretical Composition of the Mesoporous Material after Intercalation of the Organometallic Species into the Lattice of the Composite (a) with Less than or Equal to 0.1 Equivalents of  $\text{CoCp}_2$  to Nb; (b) with Greater than 0.1 Equivalents of the Organometallic to Nb Ratio, within the Mesoporous Material.

Based on these particular studies it can be concluded that superparamagnetism is indeed dependant on the ratio of Co (II) to Co (III) within the synthesised material and that this transition will not occur until the Co:Nb ratio is  $>0.1:1.0$  or until the Co(II):Co(III) ratio is less than 1:1.17 respectively. Furthermore, the unique behaviour of these

systems has demonstrated that very subtle changes in the loading level of these materials can lead to a dramatic alteration of magnetic properties.

### 2.2.3.2. Probing the Thermal Stability of Composite 3.

Heat treatment of composite 3 for 14 hours at 50°C (under vacuum in a sealed quartz tube) led to a noticeable loss of cobaltocene from the system – as evidenced via XPS analysis of the Co 2p 3/2, 1/2 region. **Figure 37(b)** illustrates this phenomenon for the heat-treated material 3 (showing a very broad spectrum) when compared to the non heat-treated spectrum of the same composite (**Figure 37(a)**). The organometallic composition within this heated material is likely to comprise of a mixture of Co oxide, cobaltocene and cobaltocinium. However, due to the broad line shape of the spectrum it is difficult to determine which precise Co species is present within the mesoporous material.

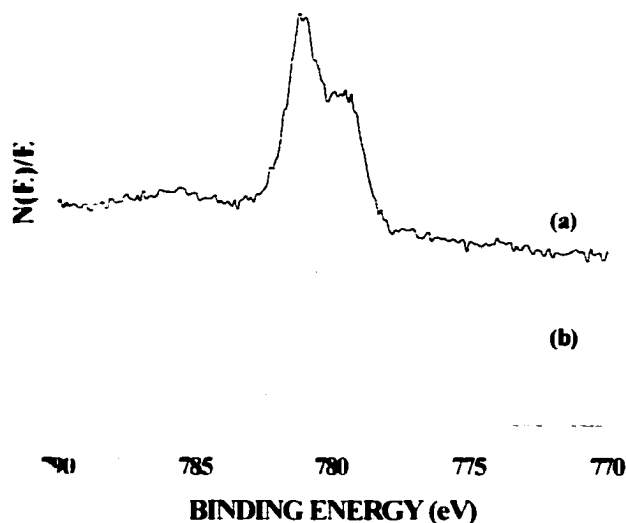


**Figure 37:** XPS Spectrum for the Co 2p 3/2 region, Comparing Non-Heat Treated Material 3(a), to that of the Heated Sample (b).



Further evidence indicating the apparent loss of cobaltocene from the system under these conditions was observed when analysing the EPR spectra for these materials. A noticeable reduction in the  $\text{CoCp}_2$  paramagnetic peak height distribution was detected when compared to the non heat-treated material. We attributed this observed loss to the reaction of the unreduced cobaltocene within the mesoporous framework with water liberated from internal condensation reactions beneath the surface inside the mesopores of the composite.

A broadening of peaks was also observed when comparing the Nb 3d 5/2, 3/2 XPS region of these two samples. **Figure 38(a)** (non heat-treated) **Figure 38(b)** (heat-treated).

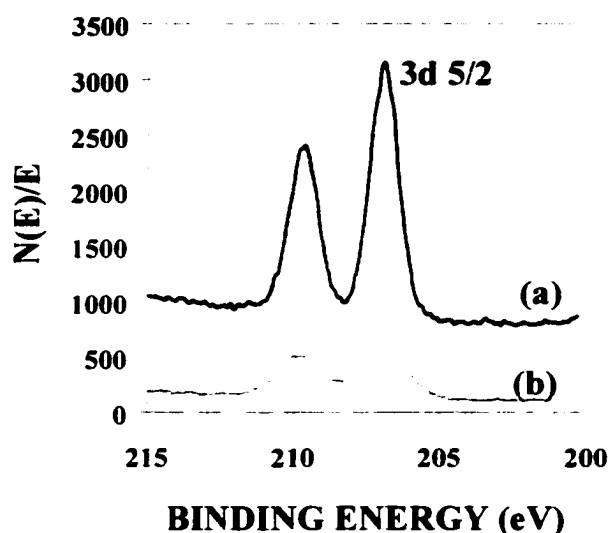


**Figure 38:** XPS Spectrum for the Nb 3d 5/2, 3/2 region, Comparing Non-Heat Treated Material **3 (a)**, to that of the Heated Sample **(b)**.

Analysis of the XPS O1s region revealed that upon thermal treatment two new oxygen species were observed at 529.8 eV and 531.9 eV as compared to the shift of the

non heated material at 530.2 eV. This is consistent with the reaction of the unreduced CoCp<sub>2</sub> species with the water liberated from within the mesopores of the material. However, from the spectroscopic data attained it is difficult to accurately determine the precise nature of the oxygen species present.

We can conclude from these studies that these intercalated mesoporous materials are heat sensitive and that upon thermal treatment, XPS analysis indicated the loss of cobaltocene from within the composite.

#### 2.2.4. Effect of Wall Composition on Superparamagnetic Cobaltocene Mesoporous Materials.

In order to probe into the effect of changing the composition of the walls and hence, the oxidising ability of the structure, we examined cobaltocene composites of mesoporous Ti and Ta oxide.

##### 2.2.4.1. Ti-TMS1 CoCp<sub>2</sub> (6)

When a sample of phosphate free trimethylsilated Ti-TMS1, with a BET surface area of 500 m<sup>2</sup>g<sup>-1</sup>, a cumulative pore volume of 0.275 cm<sup>3</sup>g<sup>-1</sup>, an HK pore size of 24 Å and a broad XRD peak centred at  $d = 56$  Å (**Figure 39(a)**), was treated with excess cobaltocene in toluene for several days followed by filtration and extensive washings, a new dark blue material (**6**) with a BET surface area of 298 m<sup>2</sup>g<sup>-1</sup>, an HK pore size of 23 Å and a pore volume of 0.182 cm<sup>3</sup>g<sup>-1</sup> and a similar XRD pattern (**Figure 39(b)**) to the parent oxide was isolated. The nitrogen adsorption isotherm for the trimethylsilated Ti-TMS1 material is shown in **Figure 40(a)**, while **Figure 40(b)** shows that for material **6**.

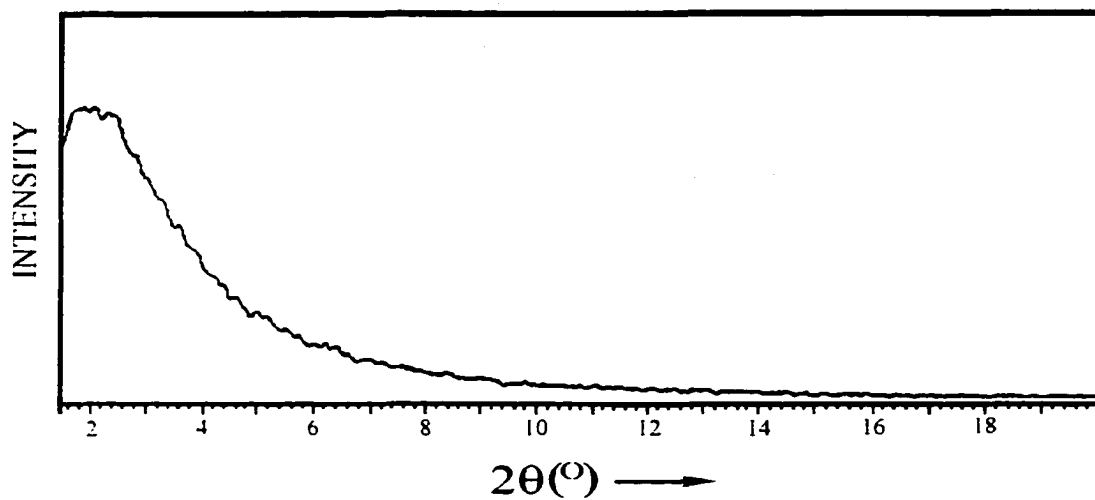


**Figure 39(a):** XRD Diffraction Pattern of Trimethylsilated Ti-TMS1.

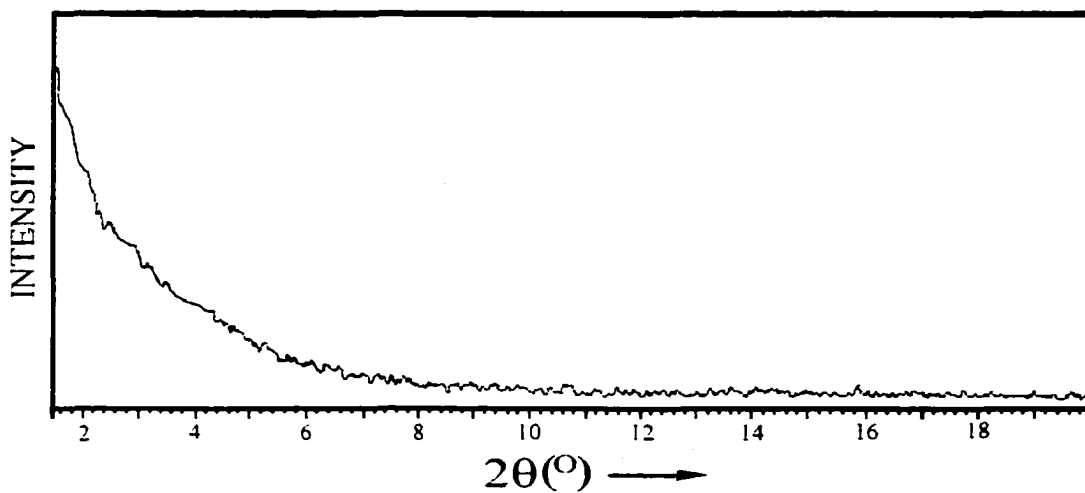


**Figure 39(b):** XRD Diffraction Pattern of **6**.

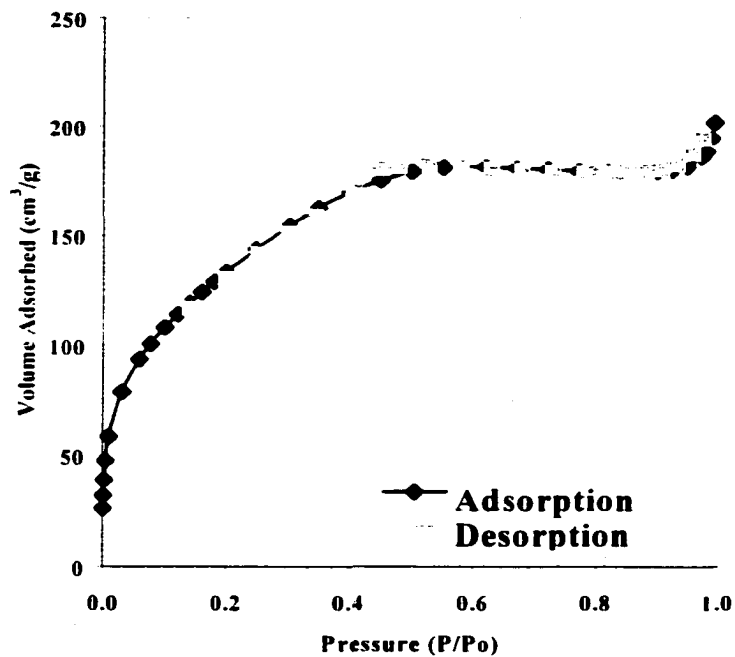


**Figure 40(a):** Nitrogen Adsorption Isotherm of a Sample of Trimethylsilated Ti-TMS1.

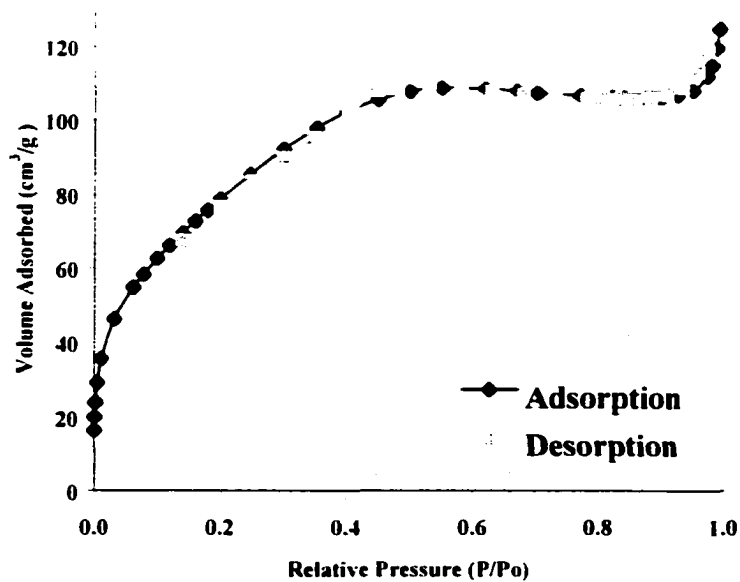


**Figure 40(b):** Nitrogen Adsorption Isotherm of 6.

Both the nitrogen adsorption isotherms and XRD data demonstrated that retention of the mesostructure was achieved for the system after intercalation of the organometallic.

Upon oxidation, a colour change was observed from dark blue to bright green. Elemental analysis of the trimethylsilylated Ti-TMS1 material gave the following calculated empirical formula  $C_{26}H_{80}Ti_{30}SiO_{122}$  and  $C_{205}H_{358}Ti_{125}SiCo_{11}O_{440}$  for the saturated non-oxidized product, **6**. From this analysis, the calculated Co:Ti mol ratio for the product was 0.088:1.0. When comparisons were made with respect to the M:Co (M = Nb, Ti) ratio we observed that the Ti (**6**) material had a significantly lower Ti:Co ratio, than that of the Nb materials, indicating that the Ti-TMS1 absorbed much less cobaltocene than the Nb composites. This was possibly due to the increased difficulty to substantially reduce the Ti species from the +4 oxidation state to the +3 oxidation state as compared to that of the Nb-TMS1 species. This was further reflected in the XPS Ti 2p  $3/2$  (458.4 eV) and 2p  $1/2$  (464 eV) regions for **6** (**Figure 41(a)**) that showed a very minor shift to a lower binding energy (459.1 eV and 464.9 eV respectively), indicating a partial reduction of the Ti oxide walls (**Figure 41(b)**).<sup>116</sup>

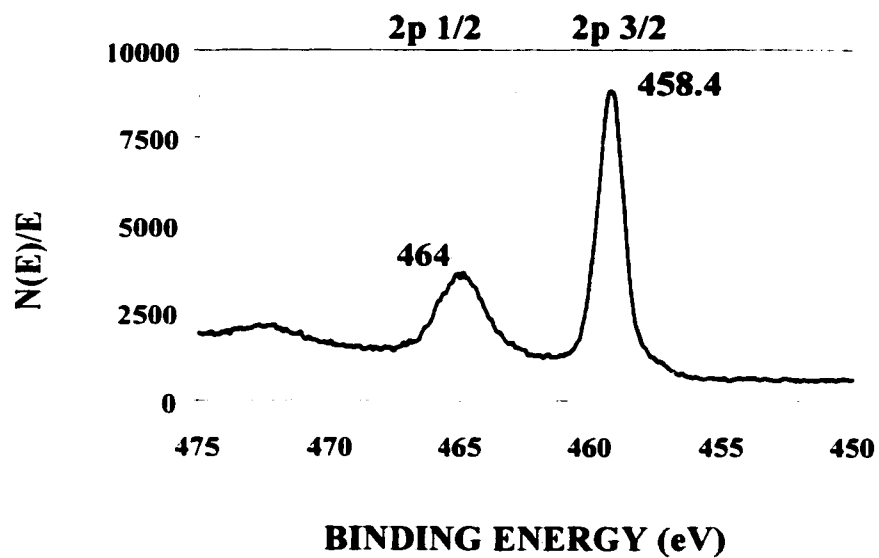


**Figure 41(a):** XPS Spectrum of Ti 2p 3/2, 1/2 Region for 6.

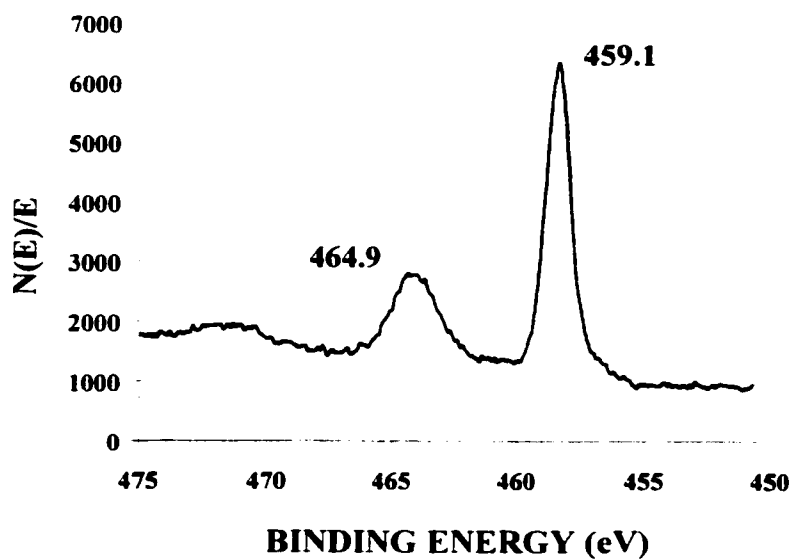


**Figure 41(b):** XPS Spectrum of Ti 2p 3/2, 1/2 Region for the Trimethylsilated Ti-TMS1 Composite.

**Figure 41(c)** shows the Co 2p 3/2 region for this system. Primarily, there was no peak associated with the Co(II) species, indicating a decreased amount of the organometallic in the pore structure. For this reason an intensity ratio for the Co(II):Co(III) was difficult to calculate.

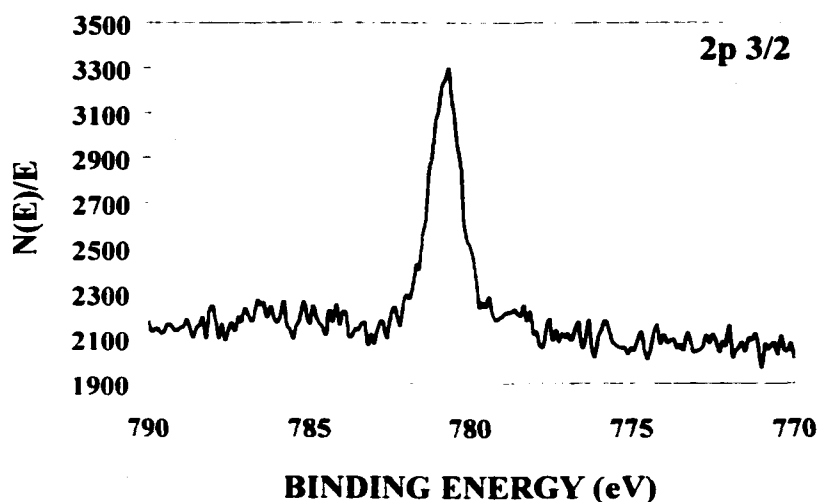


**Figure 41(c):** XPS Spectrum of the Co 2p 3/2 Region for 6.

The UV reflectance spectrum of this material showed absorbances at 250 nm for the Ti-O sp valence band-to-conduction band (VB-CB) transition,<sup>100</sup> 480 nm for the cobaltocinium cation  $\pi$ - $\pi^*$  transition (evidence that again the cobaltocene was oxidized to cobaltocinium without decomposition within the mesostructure) and a broad absorbance at roughly 590 nm for the Ti 3d-cobaltocene  $\pi^*$  impurity band-to-conduction band transition confirming the presence of Co(III) in the structure and the transfer of an electron to the titanium oxide mesostructure.

The EPR spectrum of the isolated product 6 (**Figure 42**) showed a major peak at 3357 G for the free electron. This is attributed to the free electron in the Ti-oxide walls

and a minor peak corresponding to the neutral cobaltocene species. The registered Co(II) peak was lower in intensity than for the Nb spectra reflecting a decreased amount of cobaltocene in the pore structure.

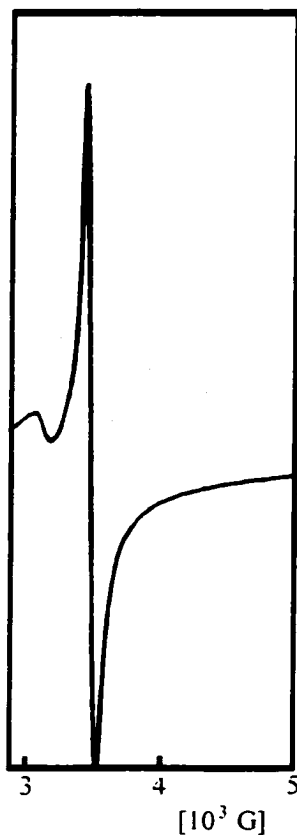


**Figure 42:** EPR Spectrum For 6.

Low temperature magnetic measurements (M vs. T and B vs. H) showed that this material was paramagnetic with no sign of a superparamagnetic transition. (**Figure 43** and **Figure 44** respectively). Neither hysteresis was observed for the M vs. T plot, nor was there any observable ZFC FC bifurcation. For the B vs. H graph, there was no observable hysteresis at 10 K or at 300 K. In fact, at both temperatures **6** exhibited a



rapid linear increase in magnetisation as the field increased. This phenomenon is common for materials exhibiting paramagnetic properties. We attributed these observations to the very low loading level of cobaltocene in the material. The SEM images gave an average particle size for **6** of 12.5  $\mu\text{m}$ .

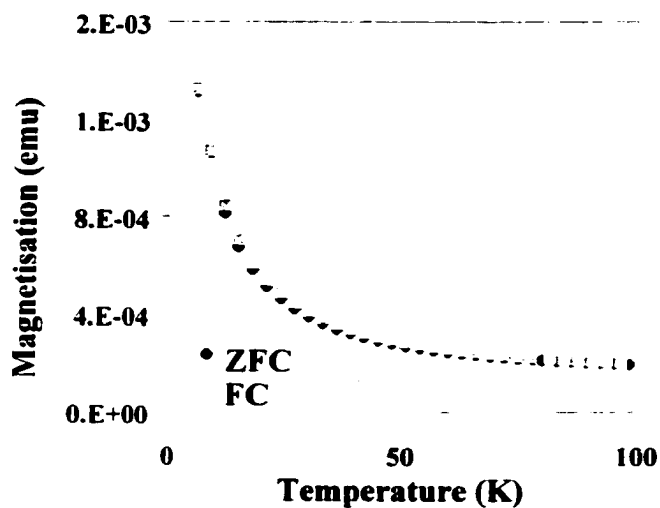


**Figure 43: M vs. T Plot for Material 6.**

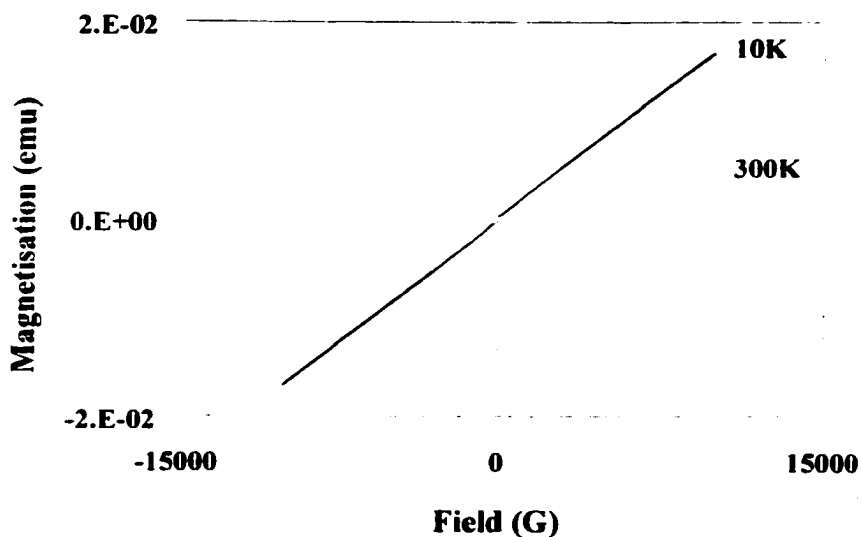


**Figure 44: B vs. H Plot for Material 6.**

A change in wall composition from Nb to Ti had a significant effect on the magnetic properties for the system. Superparamagnetism was strongly dependent on the loading level of cobaltocene within the composite. For this reason, the small pore Ti-TMS1 material **6**, which was more difficult to reduce and had more cobaltocinium present in the pore structure (relevant to the larger pore Nb-TMS1 materials), showed no superparamagnetic properties.

#### 2.2.4.2. Ta-TMS1 CoCp<sub>2</sub> (**7**)

When a sample of trimethylsilated Ta-TMS1, with a BET surface area of 420 m<sup>2</sup>g<sup>-1</sup>, a cumulative pore volume of 0.116 cm<sup>3</sup>g<sup>-1</sup>, an HK pore size of 20 Å and an XRD peak centred at  $d = 34$  Å (**Figure 45(a)**), was treated with excess cobaltocene in toluene for several days followed by filtration and extensive washing a new light green material (**7**) with a reduced BET surface area of 311 m<sup>2</sup>g<sup>-1</sup>, an HK pore size of 19 Å, a pore volume of 0.055 cm<sup>3</sup>g<sup>-1</sup> and a virtually identical XRD pattern was isolated (**Figure 45(b)**). The nitrogen adsorption isotherm for the trimethylsilated Ta-TMS1 material is shown in **Figure 46(a)**, while **Figure 46(b)** shows that for material **7**.

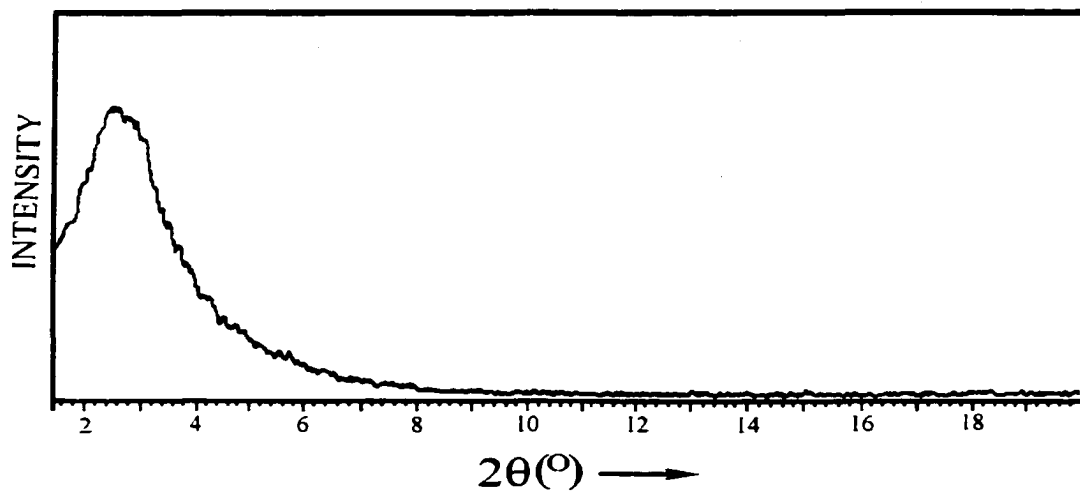


**Figure 45(a):** XRD Diffraction Pattern for the Trimethylsilated Ta-TMS1 Mesoporous Material.

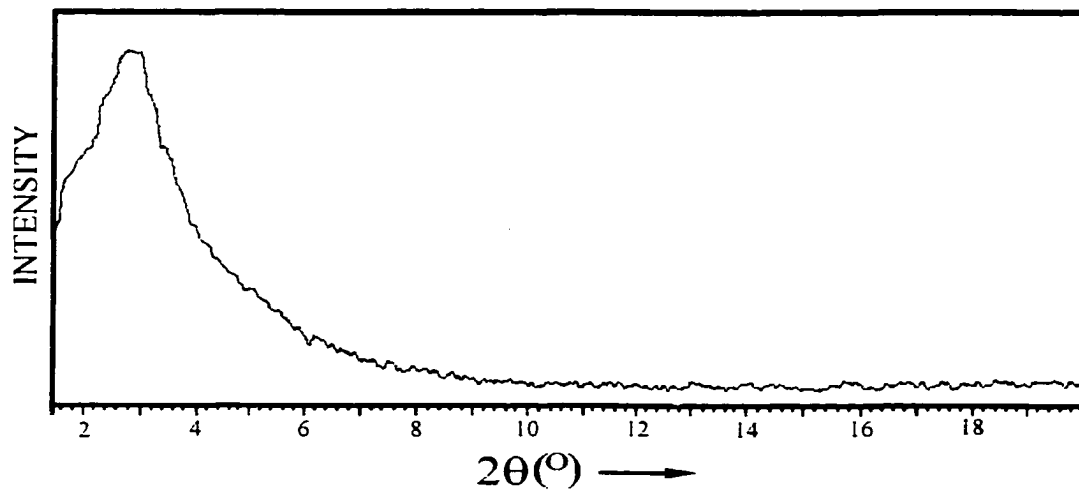


**Figure 45(b):** XRD Diffraction Pattern for material 7.

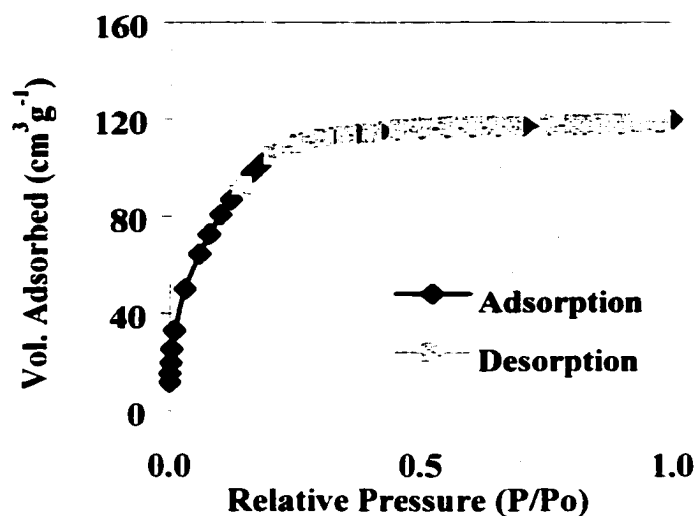


**Figure 46(a):** Nitrogen Adsorption Isotherm for the Trimethylsilated Ta-TMS1 Mesoporous Composite.

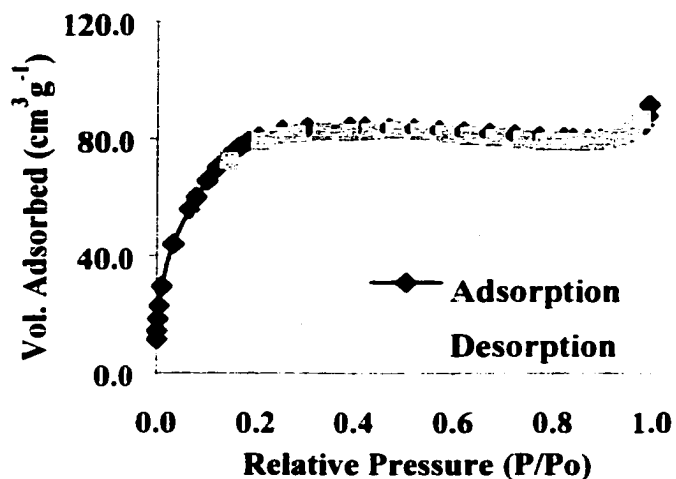


**Figure 46(b):** Nitrogen Adsorption Isotherm for material 7.

As with the Ti-TMS1 materials, both the nitrogen adsorption isotherms and XRD data demonstrated that retention of the mesostructure was achieved for the system after intercalation of the organometallic. Oxidation of the product led to a slight colour change from green to pale green. Elemental analysis of the trimethylsilated Ta-TMS1 material gave a calculated empirical formula of  $C_{10}H_{29}Ta_6SiO_{27}$  and for the mesoporous product

(7)  $C_{36}H_{68}Ta_{15}SiCoO_{76}$ . From this analysis the calculated Co:Ta mol ratio for **7** was 0.087:1.0, lower than that observed for the Nb materials indicating that the Ta-TMS1 had absorbed much less cobaltocene which was possibly due to the increased difficulty to reduce the Ta from the +5 oxidation state to the +4 oxidation state as compared to that of the Nb-TMS1 materials. This was further reflected in the XPS Ta 4f 7/2 (26.3 eV) and 4f 5/2 (28.1 eV) regions of **7** (**Figure 47(a)**) that indicated a very minor shift to lower binding energy (26.9 eV and 28.7 eV respectively) when compared to the trimethylsilated Ta-TMS1 material (**Figure 47(b)**).

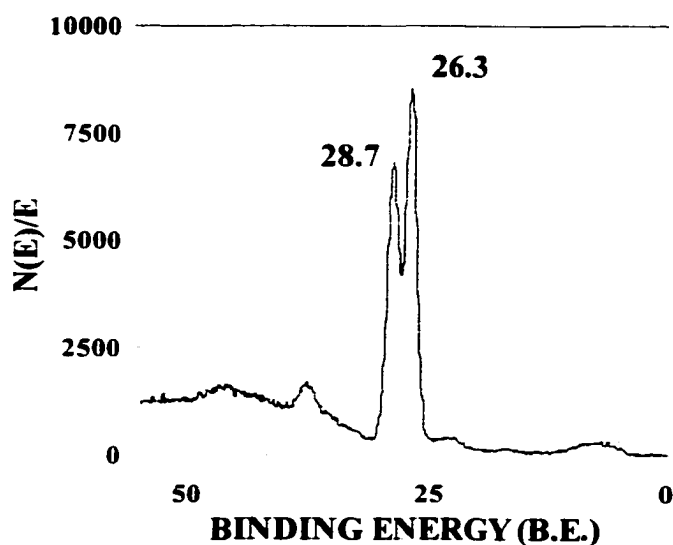


**Figure 47(a):** XPS Spectrum for Ta 4f 7/2, 5/2 Region for **7**.

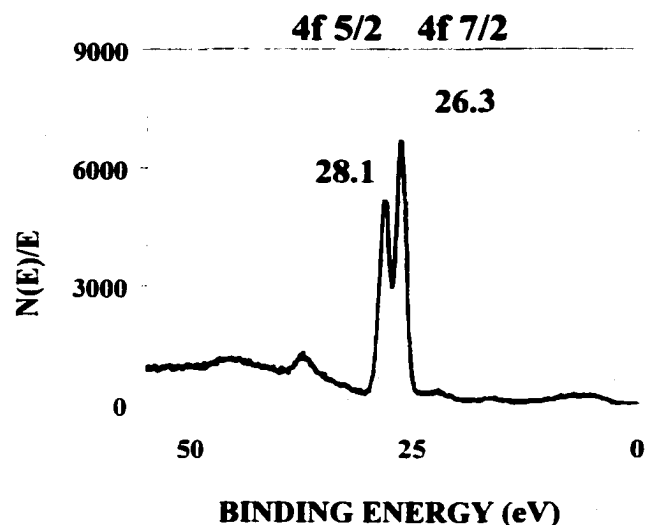


**Figure 47(b):** XPS Spectrum for Ta 4f 7/2, 5/2 Region for Trimethylsilated Ta-TMS1 Mesoporous Composite.

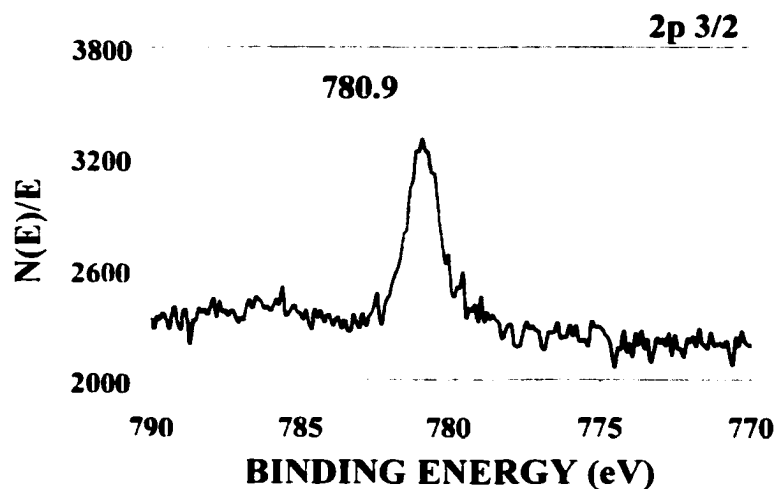


**Figure 47( c):** XPS Spectrum for Co 2p 3/2 Region for 7.

Analysis of the XPS spectrum for the Co 2p 3/2 region (**Figure 47( c)**) indicated that the vast majority of the cobalt species detected within the sample was in the form of cobaltocinium. There was no peak correlating to the Co(II) species, indicating a

decreased amount of the organometallic in the pore structure. For this reason an intensity ratio for the Co(II):Co(III) was difficult to calculate.

The UV spectrum of this material showed absorbances at 250 nm for the Ta-O sp valence band-to-conduction band (VB-CB) transition, 480 nm for the cobaltocinium cation  $\pi$ - $\pi^*$  transition, and a broad absorbance at roughly 590 nm for the Ta 5d-cobaltocene  $\pi^*$  impurity band-to-conduction band transition, confirming the presence of Co(III) in the structure and the transfer of an electron to the tantalum oxide mesostructure.

The EPR spectrum (**Figure 48**) for **7** clearly showed two peaks, the larger peak reflecting the free electron from the Ta mesoporous framework (3387 G) and the minor peak reflecting that of the cobaltocene species. again this peak was lower in intensity than those recorded for the Nb-based materials and reflects a decreased amount of cobaltocene in the pore structure of the mesoporous material.

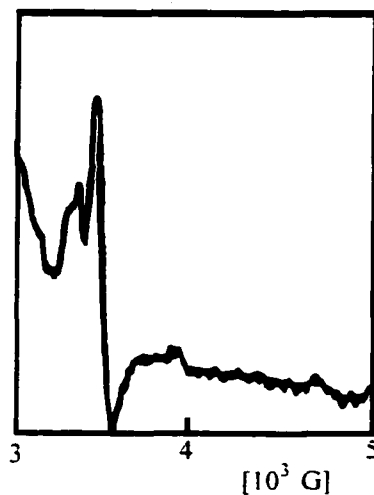


**Figure 48:** EPR Spectrum for Material 7.

Low temperature magnetic measurements for both M vs. T and B vs. H plots indicated that 7 was paramagnetic with no sign of a superparamagnetic transition at 18 K. Very minor amounts of hysteresis were detected for the M vs. T, ZFC FC plot and no identifiable bifurcation for these two regions was observed. In the same respect, no hysteresis was observed for the B vs. H plots at both 10 K and 300 K, **Figure 49(a)** and **49(b)** respectively. We attribute the paramagnetic properties of this material to the very low loading level of the cobaltocene within the system. The SEM images of the product 7 gave a mean calculated particle size of 8.5  $\mu\text{m}$ .

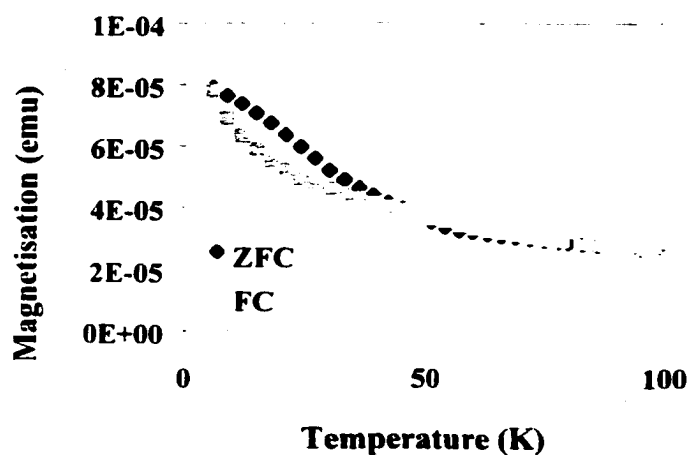


**Figure 49(a): M vs. T Plot for 7.**



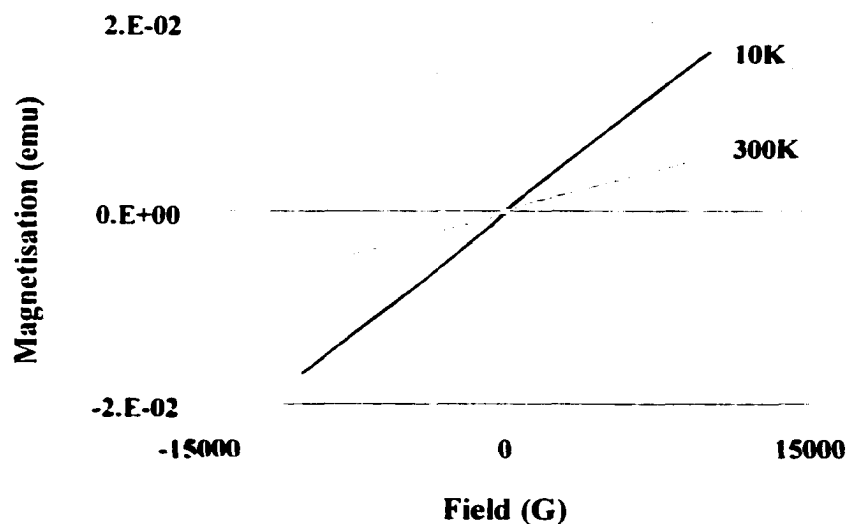


**Figure 49(b): B vs. H Plots at 10 K and 300 K for 7.**

In summary, a change in wall composition from Nb to Ta does in fact have a significant effect on the magnetic properties for the system. Superparamagnetism appears to be strongly dependent on the loading level of cobaltocene within the system and for this reason the smaller pore Ta-TMS1 materials, which are more difficult to reduce and have more cobaltocinium present in the pore structure (relevant to the larger pore Nb-TMS1 materials), showed only paramagnetic behaviour.

### 2.2.5. Host-Guest Equilibrium Effects on the Mesoporous Composites. (8)

While coulombic forces can readily be invoked to explain why the Co(III) resides in the reduced, and therefore negatively charged pore structure of the material, the fact that the excess Co(II) could not be washed out indicated that there are strong host guest effects at play governed by an equilibrium between solvation by toluene and inclusion in the pore structure. In order to further probe into the factors contributing to the Co:Nb loading level we chose to investigate samples of mesoporous Nb-TMS1 dried in an oven at 180°C without treatment by trimethylsilylchloride. Once dried the mesoporous Nb-TMS1 was added to a saturated solution of cobaltocene in toluene and left to stir for several days under nitrogen at room temperature. Filtration of the reaction mixture, followed by repeated washings with toluene, led to the isolation of a fine green precipitate (8). Elemental analysis of the product showed that the maximum molar adsorption ratio was roughly 0.3:1.0 Co:Nb, lower than that observed for materials 2 and 3 (0.5:1.0 Co:Nb respectively). We attributed this decrease in molar adsorption to the decreased hydrophobicity of the internal pores on leaving the dangling Nb-OH linkages inside the cavities intact without capping by TMS groups. This technique has been adopted in previous studies and the results given for these investigations indicate that treatment of MCM-41 with TMSCl does in fact increase the relative hydrophobicity of the respective composite.<sup>112,113</sup>

UV data confirmed the presence of three species, observed at 260 nm, 420 nm and 580 nm respectively correlating to those previously observed.

### 2.3. Conclusion

We have successfully isolated the first example of a superparamagnetic system based on a molecular ensemble rather than an extended solid.

The results presented from these studies have demonstrated that superparamagnetism within the transition metal oxide mesoporous materials was strongly dependent on both the cobaltocene loading level (where the Nb:Co ratio must exceed 1.0:0.1) and the Co(II):Co(III) ratio within the composites. A change in wall thickness for the mesoporous composites had little effect on the superparamagnetic behaviour suggesting that the superparamagnetism was dependent on the unpaired cobaltocene electrons and not the free electrons in the walls of the structure. A change in pore volume did not effect the magnetic properties of these materials and superparamagnetism was again observed. The change in pore volume had little effect on the Co(II):Co(III) ratio where for larger pore Nb-oxide based materials the ratio was 1.0:0.3 and for smaller pore Nb-TMS1 materials the ratio changed to 1.0:1.13. A change in the wall composition from large pore Nb to small pore Ti and Ta mesoporous materials did have an effect on the magnetic properties exhibited by these materials. The smaller pore Ti and Ta species were paramagnetic due to the very low cobaltocene loading level observed within these systems M:Co 1.0:0.088 which was below the critical value required of 1.0:0.1 for the onset of superparamagnetism (M = Ti or Ta). These materials were more difficult to reduce, had a large amount of cobaltocinium present within the mesopores and very little cobaltocene as evidenced via XPS analysis.

Strong host guest equilibrium effects play an important role in the cobaltocene loading level within the mesopores and for this reason Nb-TMS1 samples not treated

with trimethylsilylchloride absorbed much less cobaltocene (Nb:Co 1.0:0.3) when compared to the trimethylsilated Nb-TMS1 composites (Nb:Co, 1.0:0.5).

Thermal treatment had little effect on the superparamagnetic properties however a decrease in cobaltocene, as evidenced by XPS, studies was noted. This decrease was consistent with the condensation reactions between the organometallic moiety and the internal walls of the mesoporous composite. Furthermore, when analysing the O 1s region of the XPS spectrum for this material a noticeable broadening of the O 1s peak giving two new species (when compared to the non heat-treated material) was noted.

## 2.4. Experimental

### 2.4.1. General Methods

Nitrogen adsorption data was collected on a Micromeritics ASAP 2010. X-ray diffraction patterns ( $\text{CuK}\alpha$ ) were recorded in a sealed glass capillary on a Seimens D-500  $\theta$ - $2\theta$  diffractometer. All XPS peaks were reference to the Carbon C-(C.H) peak at 284.8 eV and the data were obtained using a Physical Electronics PHI-5500 using charge neutralisation. The conductivity measurements were recorded on a Jandel 4-point universal probe head combined with a Jandel resistivity unit. The band gaps were recorded from powder UV-visible spectra collected on an Ocean Optics S2000 fibre optics spectrometer equipped with an Analytical Instrument Systems Light Source emitter with a tungsten halogen lamp and an Ocean Optics UV 0.4 mm, 2M reflection probe. EPR samples were prepared under vacuum and the data collected on a Brüker X-band ESP 300E EPR spectrometer. Scanning Electron Microscopy (SEM) analysis was conducted on a JOEL JSM-5800LV Scanning Microscope. Magnetic measurements were conducted on a Quantum Design SQUID magnetometer MPMS system with a 5 Tesla magnet. Infrared spectra were recorded on a Bomen Michelson 100 Spectrometer. Galbraith Laboratories 2323 Sycamore Dr., Knoxville, TN 37921-1700, USA, performed all elemental analysis data (conducted under an inert atmosphere).

Toluene was distilled from sodium benzophenone and stored under an inert atmosphere of nitrogen. Chlorotrimethylsilane was obtained from Aldrich and distilled over calcium hydride. Cobaltocene was obtained from Aldrich and used without further purification.

Mesoporous materials were synthesised according to literature: Nb-TMS1,<sup>68,69</sup> Ta-TMS1<sup>70</sup> and Ti-TMS1.<sup>67</sup> The infrared (IR) spectra for all composites showed no evidence of a hydrocarbon C-H stretch. Unless otherwise stated these materials were treated with excess chlorotrimethylsilane (TMSCl) in dried and degassed diethyl ether for 16 hours under an inert atmosphere of nitrogen. The solvent was removed under reduced pressure and the new mesoporous composite washed several times with diethyl ether and dried in *vacuo*.

All reactions were carried out under an inert atmosphere of nitrogen and the products isolated stored at  $-37^{\circ}\text{C}$ .

### 2.4.2. Synthesis of Nb-TMS1CoCp<sub>2</sub> (1)

To a toluene suspension of the trimethylsilated Nb-TMS1.\* prepared with an octadecylamine template, with a Brunauer, Emmett, Teller (BET) surface area of 450 m<sup>2</sup>g<sup>-1</sup>, an Horvath Kawazoe (HK) pore size of 20 Å, a cumulative pore volume of 0.295 cm<sup>3</sup>g<sup>-1</sup>, a calculated wall thickness of 32 Å and a central peak in the X-ray powder diffraction pattern (XRD) at d = 45 Å, was added excess cobaltocene.

The reaction mixture was left to stir under an inert atmosphere of nitrogen for several days then filtered and the precipitate washed several times with toluene until the filtrate remained clear. The isolated product 1, olive green in colour, with a BET surface area of 230.82 m<sup>2</sup>g<sup>-1</sup>, an HK pore size of 20 Å, a cumulative pore volume of 0.209 cm<sup>3</sup>g<sup>-1</sup> and an XRD diffraction peak centred at d = 45 Å, was dried under reduced pressure and stored at -37°C. Elemental analysis for the isolated product gave: 13.47% C, 2.14% H, 0.5% N, 46.53% Nb, 0.42% Si, 32.49% O, 4.45% Co, with a calculated empirical formula of C<sub>75</sub>H<sub>142</sub>N<sub>2</sub>SiNb<sub>34</sub>Co<sub>5</sub>O<sub>136</sub> and a calculated Co:Nb mol ratio of 0.147:1.0.

---

\* Elemental analysis of the trimethylsilated Nb-TMS1 material gave: 5.38% C, 1.9% H, 0.5% N, 53.88% Nb, 0.9% Si, 37.44% O, with a calculated empirical formula of C<sub>14</sub>H<sub>59</sub>NNb<sub>18</sub>SiO<sub>73</sub>

### 2.4.3. Synthesis of Material 2

To a toluene suspension of the trimethylsilated Nb-TMS1,\* (prepared from a dodecylamine template) with a BET surface area of  $947 \text{ m}^2\text{g}^{-1}$ , a cumulative pore volume of  $0.62 \text{ cm}^3\text{g}^{-1}$ , an HK pore size of  $20 \text{ \AA}$ , a calculated wall thickness of  $20 \text{ \AA}$  and an XRD diffraction pattern centred at  $d = 35 \text{ \AA}$  was added excess  $\text{CoCp}_2$ .

The reaction mixture was left to stir under an inert atmosphere of nitrogen for several days then filtered and the precipitate washed several times with toluene until the filtrate remained clear. The isolated product 2, olive green in colour, with a BET surface area of  $220 \text{ m}^2\text{g}^{-1}$ , a cumulative pore volume of  $0.15 \text{ cm}^3\text{g}^{-1}$ , an HK pore size of  $19\text{-}20 \text{ \AA}$  and an XRD diffraction pattern at  $d = 36 \text{ \AA}$ , was then dried in *vacuo* and stored at  $-37^\circ\text{C}$ . Elemental analysis for the isolated product gave: 22.29% C, 2.64% H, 0.5% N, 34.25% Nb, 0.12% Si, 25.95% O, 3.54% Cl, 10.7% Co, with a calculated empirical formula of:  $\text{C}_{435}\text{H}_{614}\text{N}_x\text{Nb}_x\text{SiCl}_{123}\text{O}_x$  and a Co:Nb calculated mol ratio of 0.5:1.0

---

\* Elemental analysis of the trimethylsilated Nb-TMS1 material gave: 3.85% C, 1.38% H, 0.5% N, 56.9% Nb, 1.02% Si, 30.47% O, 5.9% Cl, with a calculated empirical formula of:  $\text{C}_9\text{H}_{38}\text{NNb}_{17}\text{SiCl}_5\text{O}_{53}$ .



#### 2.4.4. Synthesis of Material 3

To a toluene suspension of the trimethylsilated Nb-TMS1,\* (synthesised with an octadecylamine template). with a BET surface area of  $870 \text{ m}^2\text{g}^{-1}$ , a cumulative pore volume  $0.655 \text{ cm}^3\text{g}^{-1}$ , an HK pore size of  $29 \text{ \AA}$ , a calculated wall thickness of  $20 \text{ \AA}$  and an XRD diffraction pattern centred at  $d = 45 \text{ \AA}$ , was added excess  $\text{CoCp}_2$ .

The reaction mixture was left to stir under an inert atmosphere of nitrogen for several days then filtered and the precipitate washed several times with toluene until the filtrate remained clear. The isolated product **3**, olive green in colour, with a BET surface area of  $187 \text{ m}^2\text{g}^{-1}$ , a cumulative pore volume of  $0.217 \text{ cm}^3\text{g}^{-1}$ , an HK pore size of  $26 \text{ \AA}$  and an XRD diffraction pattern centred at  $d = 46 \text{ \AA}$ . was dried in *vacuo* and stored at  $-37^\circ\text{C}$ . Elemental analysis for the isolated product gave: 28.24% C, 2.86% H, 0.5% N, 31.58% Nb, 0.18% Si, 23.62% O, 9.75% Co, 3.27% Cl, with a calculated empirical formula of:  $\text{C}_{367}\text{H}_{444}\text{N}_6\text{Nb}_{53}\text{SiCo}_{26}\text{Cl}_{14}\text{O}_{230}$  and a Co:Nb calculated mol ratio of 0.5:1.0.

---

\* Elemental analysis of the trimethylsilated Nb-TMS1 material gave: 3.34% C, 1.22% H, 0.5% N, 57.21% Nb, 0.38% Si, 31.02% O, 6.33% Cl, with a calculated empirical formula of:  $\text{C}_{21}\text{H}_{90}\text{N}_3\text{Nb}_{46}\text{SiCl}_{13}\text{O}_{144}$

#### 2.4.4.1. Synthesis of Materials 4 and 5

To a toluene suspension of the trimethylsilated Nb-TMS1, (synthesised with an octadecylamine template), with a BET surface area of  $870 \text{ m}^2\text{g}^{-1}$ , a cumulative pore volume  $0.655 \text{ cm}^3\text{g}^{-1}$ , an HK pore size of  $29 \text{ \AA}$ , a calculated wall thickness of  $20 \text{ \AA}$  and an XRD diffraction pattern centred at  $d = 45 \text{ \AA}$ , was added 0.1 (**4**) or 0.3 (**5**) equivalents of  $\text{CoCp}_2$  as calculated on the Nb percent content for the trimethylsilated Nb-TMS1 material (ca. 57% Nb by weight).

Both reaction mixtures were left to stir under an inert atmosphere of nitrogen for several days then filtered and the precipitates washed several times with toluene until the filtrate remained clear.

The isolated product **4**, green in colour, with a BET surface of  $751.50 \text{ m}^2\text{g}^{-1}$ , a cumulative pore volume of  $0.650 \text{ cm}^3\text{g}^{-1}$ , an HK pore size of  $26 \text{ \AA}$  and an XRD peak centred at  $d = 46 \text{ \AA}$ , was dried in *vacuo* and stored at  $-37^\circ\text{C}$ .

The isolated product **5**, green in colour, with a BET surface area of  $735.42 \text{ m}^2\text{g}^{-1}$ , a cumulative pore volume of  $0.634 \text{ cm}^3\text{g}^{-1}$ , an HK pore size of  $26 \text{ \AA}$  and an XRD peak centred at  $d = 46 \text{ \AA}$ , was dried in *vacuo* and stored at  $-37^\circ\text{C}$ .

#### 2.4.4.2. Heat treatment of Material 3

Material **3** was isolated and vacuumed sealed in a 3 mm quartz EPR tube. The sample was left in a heated oven equipped with a temperature-controlled thermostat, for 14 hours at  $50^\circ\text{C}$ .

### 2.4.5. Synthesis of Material 6

To a toluene suspension of the trimethylsilated Ti-TMS1,\* with a BET surface area of  $500 \text{ m}^2\text{g}^{-1}$ , a cumulative pore volume of  $0.275 \text{ cm}^3\text{g}^{-1}$ , an HK pore size of  $24 \text{ \AA}$  and a broad XRD peak centred at  $d = 56 \text{ \AA}$ , was added excess cobaltocene. The solution gradually lightened, indicating absorption of the organometallic, and the mesoporous solid went from a light white colour to a deep blue. After several days and additional stirring to ensure complete absorption of the cobaltocene, product **6**, with a BET surface area of  $298 \text{ m}^2\text{g}^{-1}$ , an HK pore size of  $23 \text{ \AA}$ , a pore volume of  $0.182 \text{ cm}^3\text{g}^{-1}$  and a broad XRD peak centred at  $d = 56 \text{ \AA}$ , was collected by suction filtration and washed several times with toluene. Material **6** was dried in *vacuo* at  $10^{-3}$  torr and stored at  $-37^\circ\text{C}$ . Elemental analysis for the isolated product gave: 14.93% C, 2.18% H, 0.17% Si, 42.67% O, 3.91% Co, 36.14% Ti, with a calculated empirical formula of  $\text{C}_{205}\text{H}_{358}\text{Ti}_{125}\text{SiCo}_{11}\text{O}_{440}$  and a Ti:Co calculated mol ratio of 1.0:0.088

---

\* Elemental analysis for the Trimethylsilated Ti-TMS1 composite gave: 8.06% C, 2.11% H, 0.72% Si, 51.01% O, 38.1% Ti; with a calculated empirical formula of  $\text{C}_{26}\text{H}_{80}\text{Ti}_{30}\text{SiO}_{122}$

#### 2.4.6. Synthesis of material 7

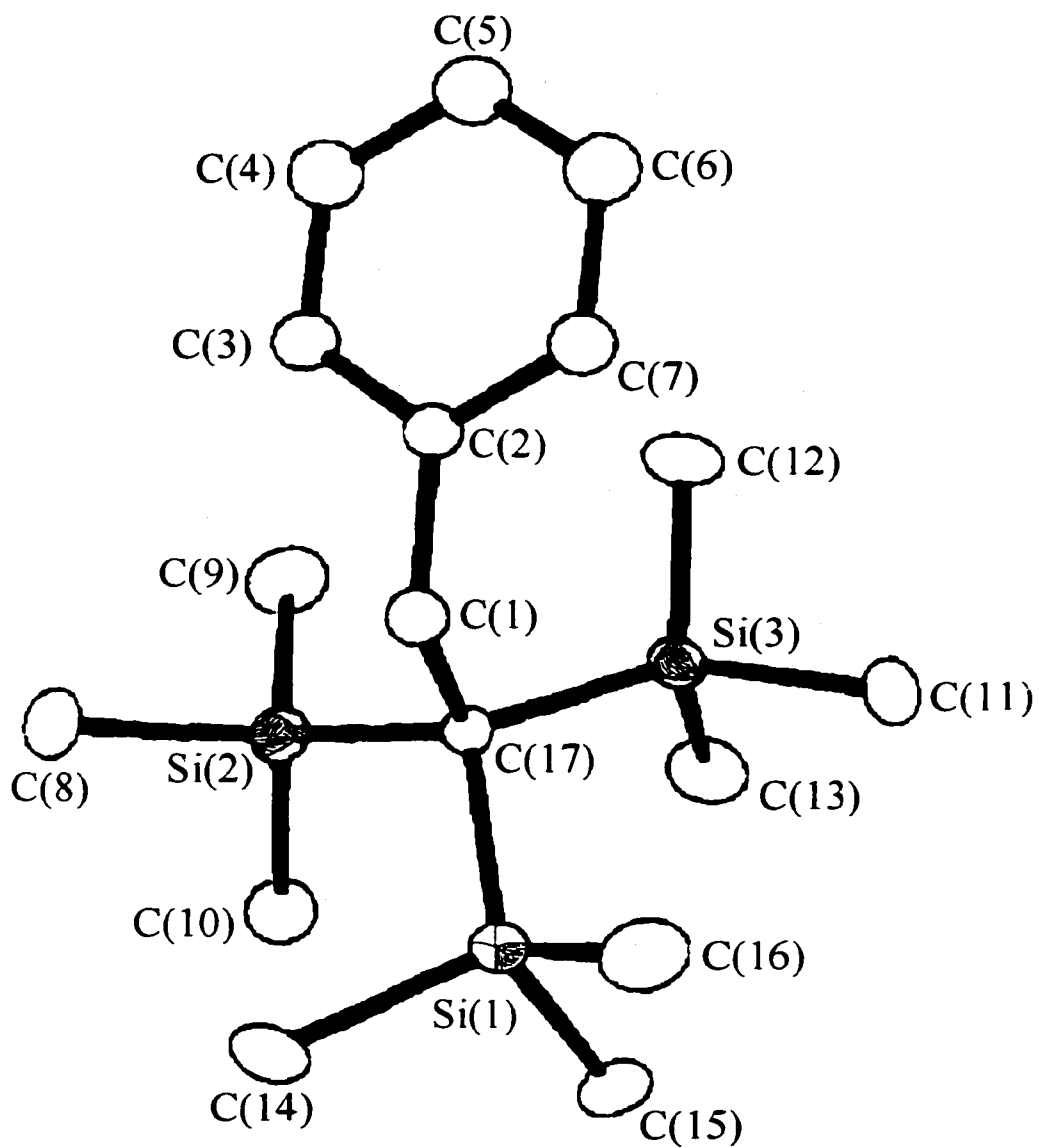
To a toluene suspension of the trimethylsilated Ta-TMS1,\* with a BET surface area of  $420 \text{ m}^2\text{g}^{-1}$ , a cumulative pore volume of  $0.116 \text{ cm}^3\text{g}^{-1}$ , an HK pore size of  $20 \text{ \AA}$  and an XRD peak centred at  $d = 34 \text{ \AA}$ , was added excess cobaltocene. The solution gradually lightened, indicating absorption of the organometallic, and the mesoporous solid went from a light white colour to green. After several days and additional stirring to ensure complete absorption of the cobaltocene, product 7, with a BET surface area of  $311 \text{ m}^2\text{g}^{-1}$ , an HK pore size of  $19 \text{ \AA}$ , a pore volume of  $0.055 \text{ cm}^3\text{g}^{-1}$  and an XRD diffraction pattern with a peak centred at  $d = 34 \text{ \AA}$ , was collected by suction filtration and washed several times with toluene. Material 7 was dried in *vacuo* at  $10^{-3}$  and stored at  $-37^\circ\text{C}$ . Elemental analysis for the isolated product gave: 9.61% C, 1.51% H, 0.62% Si, 26.91% O, 1.72% Co, 59.63% Ta, with a calculated empirical formula of  $\text{C}_{36}\text{H}_{68}\text{Ta}_{15}\text{SiCoO}_{76}$  and a Ta:Co calculated mol ratio of: 1.0:0.087.

---

\* Elemental Analysis for the Trimethylsilated Ta-TMS1 composite gave: 7.08% C, 1.66% H, 1.6% Si, 24.89% O, 64.77% Ta; with a calculated empirical formula of  $\text{C}_{10}\text{H}_{29}\text{Ta}_6\text{SiO}_{27}$

3.1 Appendix A

ORTEP of Benzyl-Tsi



### 3.2. Appendix B

#### Relevant X-ray Parameters Used in Calculating the Structure for Benzyl-Tsi

Empirical Formula	C <sub>17</sub> H <sub>34</sub> Si <sub>3</sub>	
Formula Weight	322.7106	
Temperature	293(2) K	
Wavelength	0.71073	
Crystal System	Triclinic	
Space Group	P-1	
Unit Cell Dimension	a = 8.913(3) Å	α = 81.55(2)
	b = 9.470 (2) Å	β = 87.64(2)
	c = 12.757(3) Å	γ = 76.37(3)
Volume, Z	1035.1(5) Å <sup>3</sup> , 2	
Density, Calculated	1.623 kg/m <sup>3</sup>	
Absorption Coefficient	1.139 mm <sup>-1</sup>	
F(000)	520	
Theta Range for Data Collection	1.61 to 25.00°	
Limiting Indices	-11 < h < 11, -12 < k < 12, -16 < l < 8	
Reflections Collected	5373	
Independent Reflections	3539 [R (int) = 0.0727]	
Refinement Method	Full-matrix Least-squares on F <sup>2</sup>	
Data/Results/Parameters	3532/0/181	
Goodness-of-fit on F <sup>2</sup>	1.179	
Final R Indices [I > 2σ(I)]	R1 = 0.0450, wR2 = 0.1483	
R Indices (all Data)	R1 = 0.0550, wR2 = 0.1750	
Largest Diff. Peak and Hole	0.256 and -0.233 e. Å <sup>-3</sup>	

## 3.3. Appendix C

## Relevant Structural Data for Benzyl-Tsi

## Positional Data

Atom	x	y	z	U (eq)
Si(1)	3548(1)	9284(1)	7992(1)	50(1)
Si(2)	1002(1)	7497(1)	8374(1)	51(1)
Si(3)	4057(1)	6246(1)	7150(1)	49(1)
C(1)	1817(3)	8950(2)	6345(2)	47(1)
C(2)	1323(2)	8226(2)	5480(2)	44(1)
C(3)	-23(3)	7733(3)	5534(2)	56(1)
C(4)	-429(3)	7065(3)	4737(2)	72(1)
C(5)	476(4)	6908(3)	3857(3)	81(1)
C(6)	1792(4)	7441(3)	3762(2)	73(1)
C(7)	2207(3)	8093(3)	4568(2)	56(1)
C(8)	-812(3)	9013(3)	8250(2)	73(1)
C(9)	404(4)	5776(4)	8193(3)	85(1)
C(10)	1587(3)	7193(4)	9808(2)	76(1)
C(11)	5795(3)	6699(4)	6429(3)	76(1)
C(12)	3384(3)	4997(3)	6358(2)	68(1)
C(13)	4770(4)	5017(3)	8415(2)	82(1)
C(14)	2131(4)	10801(3)	8547(3)	76(1)
C(15)	5000(3)	8387(4)	9060(2)	74(1)
C(16)	4618(4)	10300(4)	6952(3)	82(1)
C(17)	2557(2)	7983(2)	7404(2)	38(1)

**Bond Lengths (Å)**

Bond	Length
C(1)-C(2)	1.512(0.003)
C(2)-C(3)	1.382(0.003)
C(3)-C(4)	1.376(0.004)
C(4)-C(5)	1.360(0.004)
C(5)-C(6)	1.377(0.004)
C(6)-C(7)	1.379(0.004)
C(2)-C(7)	1.383(0.003)
C(1)-C(17)	1.589(0.003)
C(17)-Si(1)	1.912(0.002)
Si(1)-C(8)	1.887(0.003)
Si(1)-C(9)	1.876(0.003)
Si(1)-C(10)	1.886(0.003)
C(17)-Si(2)	1.942(0.002)
Si(2)-C(14)	1.879(0.003)
Si(2)-C(15)	1.882(0.003)
Si(2)-C(16)	1.884(0.003)
C(17)-Si(3)	1.919(0.002)
Si(3)-C(11)	1.873(0.003)
Si(3)-C(12)	1.875(0.003)
Si(3)-C(13)	1.883(0.003)

**Bond Angles (°)**

Bond	Angle
C(16)-Si(2)-C(15)	105.5(2)
C(16)-Si(2)-C(14)	103.2(2)
C(15)-Si(2)-C(14)	107.00(14)
C(16)-Si(2)-C(17)	111.99(12)
C(15)-Si(2)-C(17)	115.52(12)
C(14)-Si(2)-C(17)	112.65(12)
C(9)-Si(1)-C(8)	106.3(2)
C(9)-Si(1)-C(10)	104.2(2)
C(8)-Si(1)-C(10)	106.20(14)
C(9)-Si(1)-C(17)	114.68(13)
C(8)-Si(1)-C(17)	110.93(11)
C(10)-Si(1)-C(17)	113.83(11)
C(12)-Si(3)-C(11)	105.61(14)
C(12)-Si(3)-C(13)	103.46(14)
C(11)-Si(3)-C(13)	106.8(2)
C(12)-Si(3)-C(17)	116.12(11)
C(11)-Si(3)-C(17)	111.71(12)
C(13)-Si(3)-C(17)	112.35(12)
C(2)-C(1)-C(17)	120.1(2)
C(7)-C(2)-C(3)	117.4(2)
C(7)-C(2)-C(1)	119.6(2)
C(3)-C(2)-C(1)	122.9(2)
C(4)-C(3)-C(2)	121.4(3)
C(3)-C(4)-C(5)	120.4(3)
C(6)-C(5)-C(4)	119.5(3)
C(5)-C(6)-C(7)	120.0(3)
C(6)-C(7)-C(2)	121.2(2)
C(1)-C(17)-Si(3)	112.96(13)
C(1)-C(17)-Si(1)	102.86(13)
Si(3)-C(17)-Si(1)	109.84(10)
C(1)-C(17)-Si(2)	111.35(13)
Si(3)-C(17)-Si(2)	110.67(10)
Si(1)-C(17)-Si(2)	108.81(10)



## 4. References

---

- 1 (a) W. D. Jones, F. J. Feher, *Acc. Chem. Res.*, **1989**, *22*, 91-100; (b) J. Kickham, D. Stephan, *Angew. Chem. Int. Ed. Engl.*, **2000**, In Press.
- 2 S. S. Stahl, J. A. Labinger, J. E. Bercaw, *Angew. Chem. Int. Ed. Engl.*, **1998**, *37*, 2180-2192.
- 3 G. Peaff, *C & EN Northeast News Bureau*, *October 24*, **1994**, 13-15.
- 4 H. Basch, K. Mogi, D. G. Musaev, K. Morokuma, *J. Am. Chem. Soc.*, **1999**, *121*, 7249-7256.
- 5 E. M. Siegbahn, *Inorg. Chem.*, **1999**, *38*, 2880-2889.
- 6 Y. Ma, R.G. Bergman, *Organometallics*, **1994**, *13*, 2548-2550.
- 7 (a) R. H. Crabtree, *Chem. Rev.*, **1995**, *95*, 987-1007; (b) B. A. Arndsten, R. G. Bergman, T. A. Mobley, T. H. Peterson, *Acc. Chem. Res.*, **1995**, *28*, 154-162.
- 8 W. A. G. Graham, J. K. Hoyano, *J. Am. Chem. Soc.*, **1982**, *104*, 3723-3725.
- 9 (a) A. H. Janowicz, R. G. Bergman, *J. Am. Chem. Soc.*, **1982**, *104*, 352; (b) A. H. Janowicz, R. G. Bergman, *J. Am. Chem. Soc.*, **1983**, *105*, 3929-3938.
- 10 (a) R. G. Bergman, *Science*, **1984**, *223*, 902; (b) M. J. Wax, J. M. Stryker, J. M. Buchanan, C. A. Kovac, R. G. Bergman, *J. Am. Chem. Soc.*, **1984**, *106*, 1121-1122.
- 11 L. A. Kushch, V. V. Lavrushko, Y. S. Misharin, A. P. Shilov, *Nouv. J. Chim.*, **1983**, *7*, 729-733.
- 12 (a) J. A. Labinger, A. M. Herring, D. K. Lyon, G. A. Luinstra, J. E. Bercaw, I. T. Horvath, K. Eller, *Organometallics*, **1993**, *12*, 895; (b) J. A. Labinger, G. A. Luinstra, J. E. Bercaw, *J. Am. Chem. Soc.*, **1993**, *115*, 3004-3005; (c) J. A. Labinger, G. A. Luinstra, J. E. Bercaw, S. S. Stahl, L. Wang, *Organometallics*, **1994**, *13*, 755-756; (d) G. A. Luinstra, L. Wang, S. S. Stahl, J. A. Labinger, J. E. Bercaw, *J. Organomet. Chem.*, **1995**, *504*, 75-91; (e) S. S. Stahl, J. A. Labinger, J. E. Bercaw, *J. Am. Chem. Soc.*, **1996**, *118*, 5961-5976; (f) M. W. Holtcamp, L. M. Henling, M. W. Day, J. A. Labinger, J. E. Bercaw, *Inorg. Chim. Acta.*, **1998**, *270*, 467-478.

- 
- 13 C. C. Cummins, S. M. Baxter, P. T. Wolczanski, *J. Am. Chem. Soc.*, **1988**, *110*, 8731-8733.
- 14 D. S. Glueck, F. J. Hollander, R. G. Bergman, *J. Am. Chem. Soc.*, **1989**, *111*, 2719-2721.
- 15 T. A. Hanna, A. M. Baranger, R. G. Bergman, *J. Org. Chem.*, **1996**, *61*, 4532-4541.
- 16 D. M. Antonelii, J. E. Bercaw, Unpublished Results.
- 17 P. Burger, R. G. Bergman, *J. Am. Chem. Soc.*, **1993**, *115*, 10462-10463.
- 18 (a) B. A. Arndtsen, R. G. Bergman, *Science*, **1995**, *270*, 1970-1973; (b) J. C. W. Lohrenz, H. Jacobsen, *Angew. Chem. Int. Ed. Engl.*, **1996**, *35*, 1305-1307.
- 19 (a) *Catal. Today*, **1997**, *37*, 1; (b) R. A. Periana, D. J. Taube, E. R. Evitt, D. G. Loffler, P. R. Wentreck, G. Voss, T. Masuda, *Science*, **1993**, *259*, 340-342.
- 20 R. A. Periana, D. J. Taube, S. Gamble, T. Satoh, H. Fuji, *Science*, **1998**, *280*, 560-564.
- 21 D. Wolf, *Angew. Chem. Int. Ed.*, **1998**, *37*, 3351-3353.
- 22 K. Mylvaganam, G. B. Bacskay, N. S. Hush, *J. Am. Chem. Soc.*, **1999**, *121*, 4633-4639.
- 23 C. Eaborn, Z-R Lu, P. B. Hitchcock, J.D. Smith, *Organometallics*, **1996**, *15*, 1651-1655.
- 24 L. Merker, M. J. Scott, *J. Am. Chem. Soc.*, **1963**, *85*, 2243-2244.
- 25 (a) *Inorganic Synthesis*, **1990**, *27*, 238-239; (b) A. G. Avent, C. Eaborn, P. B. Hitchcock, G. A. Lawless, P. D. Lickiss, M. Mallien, J. D. Smith, A. D. Webb, B. Wrackmeyer, *J. Chem. Soc., Dalton Trans.*, **1993**, 19-24, 3259-3264.
- 26 R. Bassindale, A. J. Bowles, M. A. Cook, C. Eaborn, A. Hudson, R. A. Jackson, A. E. Jukes, *J. Chem. Soc. Chem. Comm.*, **1970**, 559.
- 27 A. Cook, C. Eaborn, A. E. Jukes, D. R. M. Walton, *J. Organomet. Chem.*, **1970**, *24*, 529-535.
- 28 C. Eaborn, P. B. Hitchcock, J. D. Smith, A. C. Sullivan, *J. Chem. Soc., Chem. Commun.*, **1983**, 827-828.
- 29 Z. Auibe, C. Eaborn, *J. Organomet. Chem.*, **1984**, *269*, 217-218.

- 
- 30 (a) C. Eaborn, N. Retta, J. D. Smith, *J. Organomet. Chem.*, **1980**, *190*, 101-106; (b) C. Eaborn, J. D. Smith, *Coordination Chem. Rev.*, **1996**, *154*, 125-149.
- 31 S. Al-Juaid, C. Eaborn, A. Habtemariam, P. B. Hitchcock, J. D. Smith. *J. Organomet. Chem.*, **1992**, *437*, 41-48.
- 32 C. Eaborn, P. Hitchcock, J. D. Smith, A. C. Sullivan, *J. Chem. Soc., Chem. Commun.*, **1985**, 534-535.
- 33 C. Chatgillialogu, M. Ballestri, D. Vecchi, *Tetrahedron Letters*, **1996**, *37*, 6383-6386.
- 34 (a) B. E. Douglas, D. H. McDaniel, J. J. Alexander, *Concepts and Models of Inorganic Chemistry*, Third Edition, John Wiley & Sons, Inc., **1994**, 668-673; (b) G. Wilkinson, F. G. A. Stone, E. W. Abel, *Comprehensive Organometallic Chemistry*, Pergamon Press, Oxford, **1982**, *5*, 542-547.
- 35 C. E. Johnson, R. Einsenberg, *J. Am Chem. Soc.*, **1985**, *107*, 3148-3160.
- 36 G. Wilkinson. F. G. A. Stone, E. W. Abel, *Comprehensive Organometallic Chemistry*: Pergamon Press. Oxford. **1982**. *5*, 497-498.
- 37 D. Seyferth. J. L. Lefferts. R. L. Lambert, *J. Organomet. Chem.*. **1977**, *142*, 39-53
- 38 Eaborn, P. B. Hitchcock, J. D. Smith, A. C. Sullivan, *J. Organomet. Chem.*, **1984**, *268-9*, 217-218.
- 39 N. H. Buttrus. C. Eaborn. P. B. Hitchcock, J. D. Smith, A. C. Sullivan, *J. Chem. Soc., Chem. Commun.*. **1985**, 1380-1381.
- 40 R. A. Zelonka. M. C. Baird, *J. Organometallic Chem.*, **1972**, *35*, C43.
- 41 M. A. Bennett. A. K. Smith. *J. Chem. Soc. Dalton Trans.*, **1974**, 233-241.
- 42 (a) *Chem. Ber.*. **1978**. *111* (11) 3573-84; (b) *J. Organomet. Chem.*, **1982**, *229* (2), 113-118.
- 43 M. Brookhart. W. Lamanna, M. B. Humphrey, *J. Am. Chem. Soc.*, **1981**, *103*, 989-999.
- 44 (a) H. Gilman. C. L. Smith. *J. Organomet. Chem.*, **1968**, *14*, 91-101; (b) H. Burger. W. Kilian. *J. Organomet. Chem.*, **1969**, *18*, 299-306; (c) K. W. Klinkhammer. *Chem. Eur. J.*, **1997**, *3*, 1418-1431; (d) M. Nanjo, A. Sekiguchi, H. Sakurai, *Bull. Chem. Soc. Jap.*, **1998**, *71*, 741-747.

- 
- 45 Z. Wu, J. Diminnie, Z. Hue, *J. Am. Chem. Soc.*, **1999**, *121*, 4300-4301.
- 46 (a) L. Li, J. B. Diminnie, X. Liu, J. L. Pollitte, Z. Xue, *Organometallics*, **1996**, *15*, 3520-3527; (b) U. Burckhardt, T. D. Tilley, *J. Am. Chem. Soc.*, **1999**, *121*, 6328-6329.
- 47 (a) B. Giese, B. Kopping, *Tetrahedron Letters*, **1989**, *30*, 681-684; (b) C. Chatgillialogu, *Acc. Chem. Res.*, **1992**, *25*, 188-194.
- 48 G. Wilkinson, F. G. A. Stone, E. W. Abel, *Comprehensive Organometallic Chemistry*, Pergamon Press, Oxford, **1982**, *3*, 730-742.
- 49 G. Wilkinson, *Coordination Chemistry*, Pergamon Press, Inc., Oxford, **1987**, *3*, 589-591.
- 50 (a) R. R. Shrock, *J. Organomet. Chem.*, **1976**, *122*, 209-225; (b) L. W. Messerle, P. Jennische, R. R. Schrock, G. Stucky, *J. Am. Chem. Soc.*, **1980**, *102*, 6744-6752; (c) G. A. Rupprecht, L. W. Messerle, J. D. Fellmann, R. R. Schrock, *J. Am. Chem. Soc.*, **1980**, *102*, 6236-6244.
- 51 R. R. Shrock, P. R. Sharp, *J. Am. Chem. Soc.*, **1978**, *100*, 2389-2399.
- 52 A. Sekiguchi, M. Nanjo, C. Kabuto, H. Sakurai, *Angew. Chem. Int. Ed. Engl.*, **1997**, *36*, 113-115.
- 53 M. A. Bennett, A. K. Smith, *J. Chem. Soc., Dalton Trans.*, **1974**, 233-241.
- 54 C. T. Kresge, M. E. Leonowicz, W. J. Roth, J. C. Vartuli, J. S. Beck, *Nature*, **1992**, *359*, 710-712.
- 55 C. T. Kresge, M. E. Leonowicz, W. J. Roth, J. C. Vartuli, J. S. Beck, K. D. Schmitt, C. Chu, D. H. Olson, E. W. Sheppard, S. B. Higgins, J. B. Schlenker, *J. Am. Chem. Soc.*, **1992**, *114*, 10834-10843.
- 56 IUPAC definition, *Pure and Appl. Chem.*, **1972**, *31*, 578.
- 57 J. M. Baker, J. C. Dore, P. J. Behrens, *J. Phys. Chem. B*, **1997**, *101*, 6226-6229.
- 58 (a) H. Hartmann, A. Poppel, L. Keran, *J. Phys. Chem.*, **1995**, *99*, 9, 17494-17496; (b) J. M. Kim, J. H. Kwak, S. Jun, R. Ryoo, *J. Phys. Chem.*, **1995**, *99*, 16742-16747; (c) K. R. Kloetstra, H. van Bekkum, *J. Chem. Soc. Chem. Commun.*, **1995**, 1005-1006; (d) M. Yonemitsu, Y. Tanaka, M. Iwamoto, *Chem. Mater.*, **1997**, *9*, 2679-2681.

- 
- 59 S. Goodchild, *Laboratory Focus*, September 1999, 3, No. 2, 11-12.
- 60 A. Jentys, N. H. Pham, H. Vinek, M. Englisch, J. A. Lercher, *Microporous Mater.*, 1996, 6, 13-17.
- 61 K. Moller, T. Bein, *Chem. Mater.*, 1998, 10, 2950-2963.
- 62 J. Y. Ying, C. P. Mehnert, M. S. Wong, *Angew. Chem.*, 1999, 111, 58-82; *Angew. Chem. Int. Ed. Engl.*, 1999, 37, 664.
- 63 Q. Huo, D. I. Margolese, U. Ciesla, D. G. Demuth, P. Feng, T. E. Gier, P. Sieger, A. Firouzi, B. F. Chmelka, F. Schuth, G. D. Stucky, *Chem. Mater.*, 1994, 6, 1176-1191.
- 64 Q. Huo, D. I. Margolese, U. Ciesla, P. Feng, T. E. Gier, P. Sieger, R. Leon, P. M. Petroff, F. Schuth, G. D. Stucky, *Nature*, 1994, 368, 317-321.
- 65 P. T. Tanev, T. J. Pinnavaia, *Science*, 1995, 267, 865-867.
- 66 U. Ciesla, D. Demuth, R. Leon, P. Petroff, G. D. Stucky, K. Unger, F. Schuth, *J. Chem. Soc., Chem. Commun.*, 1994, 1387-1388.
- 67 D. M. Antonelli, J. Y. Ying, *Angew. Chem. Int. Ed. Engl.*, 1995, 34, 2014-2017.
- 68 D. M. Antonelli, J. Y. Ying, *Angew. Chem. Int. Ed. Engl.*, 1996, 35, 426-430.
- 69 D. M. Antonelli, A. Nakahira, J. Y. Ying, *Inorg. Chem.*, 1996, 35, 3126-3136.
- 70 D. M. Antonelli, J. Y. Ying, *Chem. Mater.*, 1996, 8, 874-881.
- 71 M. S. Wong, D. M. Antonelli, J. Y. Ying, *Nanostructured Materials*, 1997, 9, 165-168.
- 72 D. M. Antonelli, *Adv. Mater.*, 1999, 11, 487-492.
- 73 Z-R. Tian, W. Tong, J.-Y. Wang, N.-G. Duan, V. V. Krishnan, S. L. Suib, *Science*, 1997, 276, 926-929.
- 74 A. Tuel, S. Gonttier, R. Teissier, *Chem. Commun.*, 1996, 651-652.
- 75 A. Corma, M. T. Navarro, J. Perez, Pariente, *J. Chem. Soc. Chem. Commun.*, 1994, 147-148.
- 76 M. J. MacLachlan, T. Asefa, G. Ozin, *Chem. Eur. J.*, 2000, 6, 2507-2511.
- 77 C-G. Wu, T. Bein, *Chem. Mater.*, 1994, 6, 1109-1112.
- 78 T. Maschmeyer, F. Rey, G. Sankar, J. M. Thomas, *Nature*, 1995, 378, 159-162.

- 
- 79 C. F. Cheng, H. He, W. Zhou, J. Klinowski, J. A. S. Goncalves, L. F. Gladden, *J. Phys. Chem.*, **1996**, *100*, 390-396.
- 80 W. Zhang, J. Wang, P. T. Tanev, T. J. Pinnavaia, *Chem. Commun.*, **1996**, 979-980.
- 81 A. M. Fogg, V. M. Green, D. O'Hare, *Chem. Mater.*, **1999**, *11*, 216-217.
- 82 M. J. MacLachlan, M. Ginzburg, N. Coombs, T. W. Coyle, N. P. Raju, J. E. Greedan, G. A. Ozin, I. Manners, *Science*, **2000**, *287*, 1460-1463.
- 83 D. Zhao, D. Goldfarb, *Chem. Mater.*, **1996**, *8*, 2571-2578.
- 84 M. MacLachlan, P. Aroca, N. Coombs, I. Manners, G. Ozin, *Adv. Mater.*, **1998**, *10*, 144-149.
- 85 M. Vetraino, M. Trudeau, D. Antonelli, *Adv. Mater.*, **2000**, *12*, 337-341.
- 86 X. He, D. Antonelli, M. Trudeau, *Adv. Mater.*, in Press.
- 87 Y. Bing, M. Trudeau, D. M. Antonelli, *Adv. Mater.*, Submitted.
- 88 S. N. Khanna, S. Linderoth, *Phys. Rev. Lett.*, **1991**, *67*, 742-745.
- 89 M. R. Khan, R. D. Fisher, N. Heiman, *IEEE Trans. Magnet.*, **1990**, *26*, 118-120.
- 90 S. Padovani, I. Chado, F. Scheurer, J. P. Bucher, *Phys. Rev. B*, **1999**, *59*, 11887-11891.
- 91 F. Imbierwitz, J. Pelzl, E. Arnscheidt, M. Acet, H. Zahres, H. Bach, G. A. Saunders, *J. Magnetism and Magnetic Materials*, **1999**, *196/197*, 863-864.
- 92 H. J. Blythe, V. M. Fedosyuk, O. I. Kasyutich, W. Schwarzacher, *J. Magnetism and Magnetic Materials*, **2000**, *208*, 251-254.
- 93 S. A. Majetich, J. H. Scott, E. M. Kirkpatrick, K. Chowdary, K. Gallagher, M. E. McHenry, *NanoStructured Mater.*, **1997**, *9*, 291-300.
- 94 H. J. Blythe, V. M. Fedosyuk, *J. Phys. Condens. Mater.*, **1995**, *7*, 3461-3469.
- 95 J. Wecker, R. von Helmolt, L. Schultz, K. Samwer, *IEEE Trans. Magnet.*, **1993**, *29*, 3087-3089.
- 96 D. G. Clerc, D. A. Cleary, *J. Phys. Chem. Solids*, **1995**, *56*, 69-78.
- 97 G. Wilkinson, F. G. A. Stone, E. W. Abel, *Comprehensive Organometallic Chemistry*, Pergamon Press, Oxford, **1982**, *5*, 244.
- 98 D. Clack, K. Warren, *J. Organomet. Chem.*, **1978**, *152*, C60-C62.

- 
- 99 J. Carver, G. Schweitzer, *J. Chem. Phys.*, **1972**, *57*, 973-982.
- 100 A. Bakke, W. Jolly, B. Prinsky, J. Smart, *Inorg. Chem.*, **1979**, *18*, 1343-1345.
- 101 J. Ammeter, J. Swalen, *J. Chem. Phys.*, **1972**, *57*, 678-698.
- 102 R. E. Robertson, H. M. McConnell, *J. Phys. Chem.*, **1960**, *64*, 70-75.
- 103 F. W. Grevels, *J. Organomet. Chem.*, **1976**, 111.
- 104 (a) G. E. McGuire, G. K. Schweitzer, T. A. Carlson, *Inorg. Chem.*, **1973**, *12*, 2450-2453; (b) T. Novakov, T. H. Gabelle, *Solid State Commun.*, **1972**, *10*, 225-229.
- 105 V. Stone, Jr., R. Davis, *Chem. Mater.*, **1998**, *10*, 1468-1474.
- 106 Borrell, E. Henderson, *Inorg. Chim. Acta.* **1975**, *12*, 215-218.
- 107 R. E. Rosenweig, *Nature*, **1966**, *210*, 613-614.
- 108 T. D. Shen, R. B. Schwartz, J. D. Thompson, *J. Appl. Phys.*, **1999**, *85*, 4110-4119.
- 109 L. Zhang, G. C. Papaefthymiou, R. F. Ziolo, J. Y. Ying, *Nanostructured Mater.*, **1997**, *9*, 185-188.
- 110 J. Crangle, B. R. Coles (Editor), *The Structures and Properties of Solids 6*, **1977**. Chapter 1, Edward Arnold Publishers Ltd.
- 111 J. Wecker, R. von Helmolt, L. Schultz, K. Samwer, *IEEE Trans. Magnetics*, **1993**, *29*, 3087-3089.
- 112 (a) E. Ruiz-Hitzky, J. M. Rojo, *Nature*, **1980**, *287*, 28-30; (b) D. W. Sindorf, G. E. Maciel, *J. Am. Chem. Soc.*, **1983**, *105*, 3767-3776.
- 113 K. A. Koyano, T. Tatsumi, Y. Tanaka, S. Nakata, *J. Phys. Chem. B*, **1997**, *101*, 9436-9440.
- 114 J. H. Ammeter, *J. Mag. Res.*, **1978**, *30*, 299-325.
- 115 J. Hulliger, L. Zoller, J. H. Ammeter, *J. Mag. Res.*, **1982**, *48*, 512-518.
- 116 J. F. Moulder, W. F. Stickel, P. E. Sobol, K. D. Bomben, Edited by J. Chastain. *XPS Analysis*, Perkin-Elmer Corporation, Physical Electronics Division.

---

## 5. Curriculum Vitae

Date of Birth      October 27<sup>th</sup> 1974

Citizenship        British

Education          B.Sc. (1997) University of Sussex, England

M.Sc. (2000) University of Windsor, Canada

- Experience
- 1999-2000 - Executive Director of Properties and Operations for the Society of Graduate and Professional Students (SGPS), University of Windsor.
  - 1998-1999 - SGPS Representative for the School of Physical Sciences, University of Windsor.
  - 1998-1999 - Representative for the Information Technologies Council Committee, University of Windsor.

- Dissertations
1. Samantha Menzies, Dr. D. M. Antonelli\*, Synthesis Of Ligands For Extremely Electron-Deficient Late Transition Metal Complexes Useful In Alkane Functionalisation Reactions. University of Sussex, Brighton, England.
  2. Samantha Menzies, Prof. L. Busetto, Dott. Silvia Bordoni\*, La Reattività Di Complessi, Mono E Binucleare, Con Cheteneidentrifenilfosforano,  $\text{Ph}_3\text{P}=\text{C}=\text{C}=\text{O}$ , University of Bologna, Italy.
  3. Samantha Menzies, Prof. L. Busetto, Dott. Silvia Bordoni\*, La Reattività Di Complessi Dinucleari E Mononucleari Che Contengono La Funzione Tiocarbanica (-CSR) Coordinata A Ponte. University of Bologna, Italy.



- 
- Publications
1. S. Murray, M. Trudeau, D. M. Antonelli\*, Synthesis and Magnetic Tuning in Superparamagnetic Cobaltocene-Mesoporous Niobium Oxide Composites, *Adv. Mater.*, **2000**, *12*, 1339-1342.
  2. S. Murray, M. Trudeau, and D. M. Antonelli\*, XPS and Magnetic Studies on the Effect of Pore Size, Wall Thickness, and Wall Composition on Superparamagnetic Cobaltocene Mesoporous Nb, Ta, and Ti Composites, *Inorg. Chem.*, **2000**, in Press.
- Presentations
1. 30th Inorganic Discussion Weekend, October 1997, University of Toronto, Ontario, Canada. Poster display. Samantha Menzies, Dr. D. M. Antonelli\*, *Synthesis of Ligands for Extremely Electron Deficient Late Transition Metal Complexes*.
  2. 32<sup>nd</sup> Inorganic Discussion Weekend, October 1999, University of Windsor, Ontario, Canada. Poster display. Samantha Murray, Dr. M. Trudeau, Dr. D. M. Antonelli\*, *Synthesis and Superparamagnetic Behaviour in Cobaltocene – Mesoporous Niobium Oxide Composites*
  3. International Symposium on Mesoporous Molecular Sieves, Québec, Qué, CANADA, August 27 - September 2, 2000. Poster display. Samantha Murray, Dr. M. Trudeau, Dr. D. M. Antonelli\*, *The Synthesis, Electronic Properties and Magnetic Behaviour of a New Series of Nonstoichiometric Cobaltocene-Reduced Mesoporous Niobium Oxide Composites*.